

**Development and characterisation of a near-infrared  
femtosecond optical parametric oscillator  
frequency comb**

**Teresa I. Ferreiro**

Submitted for the degree of Doctor of Philosophy

Heriot-Watt University

School of Engineering and Physical Sciences

June 2013

The copyright of this thesis is owned by the author. Any quotation from the thesis or use of any information contained in it must acknowledge this thesis as the source of the quotation or information.

## Abstract

This thesis describes a 280 MHz MgO:PPLN-based optical parametric oscillator (OPO) synchronously pumped by a 50 fs Ti:sapphire laser to produce ultrafast pulses in the near-infrared. The OPO tuned over a wavelength range from 1450 - 1550 nm and 1624 - 1750 nm for the signal and idler respectively. The carrier-envelope-offset (CEO) frequency of the signal pulses was stabilised to a 10 MHz reference frequency without f-2f self-referencing, with an RMS phase variation of 0.56 rad over an observation time of 1 second. The relative intensity noise was measured for the CEO-stabilised OPO over an observation time of 64 seconds as 0.04%.

The repetition frequency of the OPO was stabilised to 280 MHz using a frequency synthesiser at the eighth harmonic (2.24 GHz). This locking loop had an RMS phase variation of 0.98 mrad over a 1 second observation time. The CEO- and repetition frequencies were then locked simultaneously to a synthesiser referenced to a Rb-disciplined source, to generate a fully stabilised 1.5  $\mu\text{m}$  frequency comb with an absolute uncertainty in comb mode position of 110 Hz. The upper limit for the fractional instability for a comb mode at 200 THz was found to be  $2 \times 10^{-11}$ , limited by the stability of the Rb reference.

A five-fold increase in comb mode spacing to 1.4 GHz was demonstrated with the stabilised frequency comb. This was achieved using a passive filter cavity, stabilised to a transmission peak via dither locking. The FWHM bandwidth of the optical spectrum for the filtered frequency comb was reduced to 8 nm, however no increase in comb linewidth was observed.

An additional experiment was carried out where an external cavity diode laser was frequency-stabilised to a saturated absorption peak in Rb at 780.2 nm using dither locking, providing an optical frequency reference for future OPO frequency combs.

## **Acknowledgements**

The work contained within this thesis has only been possible thanks to the guidance, help and support of many people.

I am grateful for the continuous support and guidance I have received from my supervisor Derryck Reid. He was always there when a problem in the lab needed to be discussed and was a never-ending source of knowledge and ideas.

I would like to thank Jinghua Sun. He trained me in the lab, taught me the aspects of frequency combs that cannot be learnt from books and papers, and never ran out of suggestions when things stopped working.

Tobi Lamour deserves my gratitude for his help and advice over the course of my PhD and the long hours he put in helping me in the lab during his brief return from Stanford.

I would also like to thank the other member of the Ultrafast Optics group, especially Richard McCracken who has provided an extra pair of hands and eyes, and a couple of feet of height when equipment is out of reach.

My thanks to Ajoy Kar for his continuous support and the loan of a range of equipment over the years.

I am grateful to Peter Heron and Mark Stewart from the Physics Mechanical Workshop for cutting, drilling and machining a whole range of components. I am also grateful to the many other technical staff, including the Electronics Workshop for their help with this project.

I appreciate the guidance and useful discussions from Helen Margolis at the National Physics Laboratory, Ken Strain and Bryan Barr from the University of Glasgow, and in particular Aidan Arnold from the University of Strathclyde for his assistance with stabilising the ECDL.

My family, Tony, Janet and Carmen, have always been there for me, even when we're living at opposite ends of the country. I am forever indebted to them for their continuing love and support.

Finally I must thank my husband Stephen for providing me with the motivation I needed when I needed it most, whether I wanted it or not. Without his infinite patience and tolerance I wouldn't be where I am now. His love and support have made writing this thesis possible.

# ACADEMIC REGISTRY

## Research Thesis Submission



Name:	Teresa I. Ferreiro		
School/PGI:	EPS		
Version: <i>(i.e. First, Resubmission, Final)</i>	Final	Degree Sought (Award <b>and</b> Subject area)	PhD, Physics

### **Declaration**

In accordance with the appropriate regulations I hereby submit my thesis and I declare that:

- 1) the thesis embodies the results of my own work and has been composed by myself
- 2) where appropriate, I have made acknowledgement of the work of others and have made reference to work carried out in collaboration with other persons
- 3) the thesis is the correct version of the thesis for submission and is the same version as any electronic versions submitted\*.
- 4) my thesis for the award referred to, deposited in the Heriot-Watt University Library, should be made available for loan or photocopying and be available via the Institutional Repository, subject to such conditions as the Librarian may require
- 5) I understand that as a student of the University I am required to abide by the Regulations of the University and to conform to its discipline.

\* *Please note that it is the responsibility of the candidate to ensure that the correct version of the thesis is submitted.*

Signature of Candidate:		Date:	
-------------------------	--	-------	--

### **Submission**

Submitted By <i>(name in capitals)</i> :	
Signature of Individual Submitting:	
Date Submitted:	

### **For Completion in the Student Service Centre (SSC)**

Received in the SSC by <i>(name in capitals)</i> :			
Method of Submission (Handed in to SSC; posted through internal/external mail):			
E-thesis Submitted (mandatory for final theses)			
Signature:		Date:	

Please note this form should bound into the submitted thesis.

Updated February 2008, November 2008, February 2009, January 2011



# Contents

<b>Chapter 1. Introduction .....</b>	<b>1</b>
1.1. Aim .....	1
1.2. Stabilised optical frequency combs.....	1
1.3. Applications of stabilised frequency combs in spectroscopy and metrology .....	3
1.3.1. Laser frequency combs .....	3
1.3.2. Optical parametric oscillator frequency combs.....	4
1.4. Thesis outline .....	10
<b>Chapter 2. Design and characterisation of a Ti:sapphire-pumped optical parametric oscillator .....</b>	<b>12</b>
2.1. Ti:sapphire laser .....	12
2.1.1. Modelocking .....	12
2.1.2. Design considerations for an ultrafast modelocked laser.....	17
2.1.3. Modelocked Ti:sapphire lasers .....	26
2.1.4. Cavity design considerations .....	28
2.1.5. Final cavity design .....	33
2.1.6. Characterisation of the Ti:sapphire laser.....	35
2.2. Optical parametric oscillator.....	38
2.2.1. Introduction to second-order nonlinear optics .....	38
2.2.2. Nonlinear optics in optical parametric oscillators.....	40
2.2.3. Introduction to synchronously pumped femtosecond optical parametric oscillators .....	44
2.2.4. Cavity design and construction .....	45
2.2.5. Characterisation of the optical parametric oscillator.....	53
2.3. Conclusions.....	55
<b>Chapter 3. Stabilisation of a synchronously pumped femtosecond optical parametric oscillator frequency comb .....</b>	<b>57</b>
3.1. Locking a frequency comb.....	57
3.1.1. Modelocked lasers – a comb of modes .....	57
3.1.2. Repetition frequency .....	58
3.1.3. CEO-frequency .....	58
3.1.4. Phase noise.....	67
3.1.5. Relative intensity noise .....	69
3.2. CEO-frequency stabilization of a femtosecond optical parametric oscillator.....	69
3.2.1. Optical and mechanical configuration .....	70
3.2.2. Electrical locking loops.....	75

3.2.3.	Bandwidth measurement of the CEO-frequency locking loop .....	77
3.2.4.	Phase noise in the CEO-frequency locking loop.....	79
3.2.5.	Relative intensity noise .....	81
3.3.	Locking the repetition frequency of the Ti:sapphire laser .....	84
3.3.1.	Phase noise for preliminary locking of the repetition frequency .....	85
3.3.2.	Phase noise for improved locking of the repetition frequency.....	86
3.4.	Locking the OPO frequency comb.....	88
3.4.1.	Locking both the CEO-frequency and repetition frequency .....	88
3.4.2.	Power spectral density of the phase noise in the frequency comb .....	89
3.4.3.	Two-sample frequency deviation and in-loop comb instability measurements ..	90
3.4.4.	Slow loop for long-term repetition frequency stabilization .....	94
3.5.	Conclusions.....	94
<b>Chapter 4. Locking the frequency of an external cavity diode laser using saturated absorption in Rubidium .....</b>		<b>96</b>
4.1.	Introduction.....	96
4.1.1.	Rubidium.....	96
4.1.2.	External cavity diode lasers .....	99
4.1.3.	Dither locking of an optical cavity.....	99
4.2.	Experimental configuration.....	101
4.2.1.	Optical design .....	101
4.2.2.	Locking electronics .....	104
4.3.	ECDL stabilisation results .....	106
4.3.1.	The locked ECDL .....	106
4.3.2.	Relative intensity noise measurements .....	107
4.4.	Conclusions and further work.....	108
4.4.1.	Improvements .....	108
4.4.2.	Frequency comb measurement.....	109
<b>Chapter 5. Mode filtering of a stabilised frequency comb .....</b>		<b>110</b>
5.1.	Mode filtering and external cavities.....	110
5.2.	Cavity locking techniques.....	111
5.3.	Designing the filter cavity.....	112
5.4.	Locking the external cavity to the frequency comb .....	116
5.4.1.	Electrical locking loop .....	116
5.4.2.	Generating a suitable error signal .....	118
5.5.	Characterisation of the stabilised filter cavity.....	124
5.6.	Conclusions and further work.....	126

5.6.1.	Conclusions.....	126
5.6.2.	Further improvements and developments.....	127
<b>Chapter 6.</b>	<b>Conclusions and further developments.....</b>	<b>129</b>
6.1.	Summary of results for this thesis.....	129
6.2.	Further developments.....	130
<b>References</b>	<b>.....</b>	<b>133</b>

## List of publications by the candidate

### Peer reviewed journal articles

**T. I. Ferreiro**, J. Sun and D. T. Reid, “Locking the carrier-envelope-offset frequency of an optical parametric oscillator without f-2f self-referencing,” *Optics Letters* **35**(10), 1668-1670 (2010).

**T. I. Ferreiro**, J. Sun and D. T. Reid, “Frequency stability of a femtosecond optical parametric oscillator frequency comb,” *Optics Express* **19**(24), 24159-24164 (2011).

D. T. Reid, J. Sun, T. P. Lamour and **T. I. Ferreiro**, “Advances in ultrafast optical parametric oscillators,” *Laser Physics Letters* **8**(1), 8-15 (2011).

**T. I. Ferreiro**, T. P. Lamour, J. Sun and D. T. Reid, “1.4-GHz femtosecond comb generation by Fabry–Pérot filtering of an optical parametric oscillator frequency comb,” *Electronics Letters* **49**(13) 833 (2013).

### Conference papers

**T. I. Ferreiro**, J. Sun and D. T. Reid, “Carrier Envelope Offset Stabilization of an Optical Parametric Oscillator Without f-2f Self-Referencing,” *Conference on Lasers and Electro-Optics (CLEO) 2010*, paper: CMX3.

# Chapter 1. Introduction

## 1.1. Aim

Over the last decade, optical frequency combs have been used across a wide range of applications as stable, broadband, high-precision optical sources and references. The aim of the research described in this thesis was to develop and characterise a stabilised optical parametric oscillator frequency comb with a simplified design compared to similar sources. This source should offer flexibility for both the comb mode separation and optical frequency, with sufficient stability and precision to be used for spectroscopic measurements in the near-infrared, and with the long-term aim of moving to the mid-infrared region of the spectrum. In this chapter I describe some of the principles and applications of stabilised frequency combs and outline the research presented in this thesis.

## 1.2. Stabilised optical frequency combs

A modelocked ultrafast laser emits a train of ultrashort pulses separated by the laser cavity round-trip time. An isolated pulse can be described in terms of a carrier wave and an envelope, where the carrier is a CW sinusoidal signal which is multiplied by the envelope function to produce the electric field of the pulse, see Figure 1.1 [1].

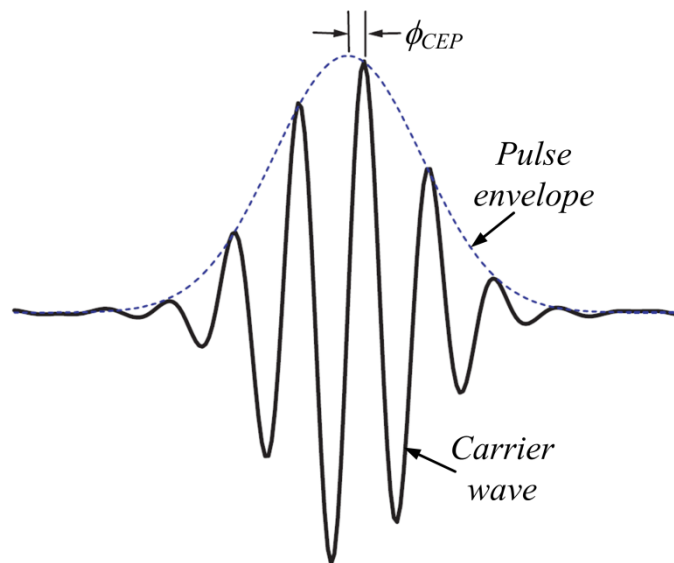


*Figure 1.1 A few-cycle ultrashort pulse where the carrier wave is offset from the pulse envelope by a continually changing phase, the CEP ( $\phi_{CEP}$ ). Image adapted from [1].*

The envelope of the pulse travels at the group velocity and the carrier travels at the phase velocity. In a dispersive material the group and phase velocity will differ so the carrier wave will ‘slip’ through the envelope and the peak of the envelope will not always line up with a peak of the carrier. The difference in phase between the envelope and carrier is the carrier-envelope-phase (CEP) of the pulse (see Figure 1.1) [1]. Pulses emitted from an optical cavity, such as a laser, sample the CEP of the intracavity pulse each time it hits the output coupler. So the CEP for each pulse relative to the previous pulse in the emitted pulse train will change by an amount called the carrier-envelope-phase-slip (CEPS), which will be constant in the absence of any noise. Perturbations to the laser system and effects such as temperature changes causing the cavity length to drift, cause the CEPS to change over time, so the CEP will not change by a fixed amount pulse-to-pulse [1].

A long train of pulses can be represented in the frequency domain as a frequency comb of narrow modes separated by the repetition frequency [2]. The CEPS produces an offset in this frequency comb so the comb lines do not lie at exact integer multiples of the repetition frequency. This frequency offset is described as the carrier-envelope-offset (CEO) frequency (see Figure 1.2) [3].

By using a stable reference and suitable feedback loops, the repetition frequency and the CEO-frequency for a pulse train can be locked to known values. This results in a stabilised frequency comb of narrow modes with constant comb line separation and position. Stabilised frequency combs can be used in a wide range of applications [4].

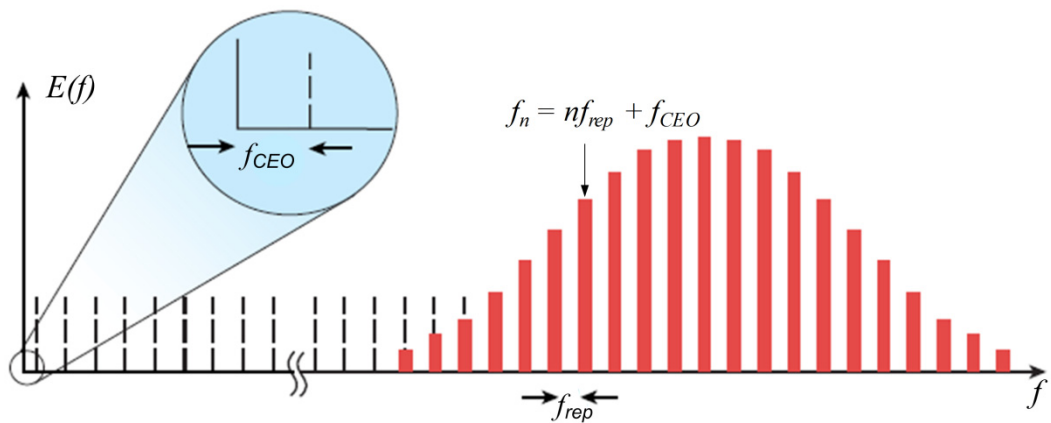


*Figure 1.2 A frequency comb of longitudinal modes for an ultrashort pulse train separated by the repetition frequency ( $f_{rep}$ ) and offset from the origin of the frequency-axis by the CEO-frequency ( $f_{CEO}$ ). Figure adapted from image in [5].*

### **1.3. Applications of stabilised frequency combs in spectroscopy and metrology**

Typical applications for stabilised frequency combs are spectroscopic and metrological measurements [5-8], including precision frequency measurement and accurate distance measurements [2, 9]. There are also applications in pulse shaping and attosecond pulse generation [10, 11]. The stabilised comb presented in this thesis was developed for applications in spectroscopy.

#### ***1.3.1. Laser frequency combs***

In 2000 Jones *et al.* demonstrated an absolute frequency measurement of a CW laser using a stabilised frequency comb based on a modelocked Ti:sapphire laser, which was CEO-frequency stabilised using f-2f self-referencing. This system represented a significantly simplified method compared to conventional frequency metrology techniques. The CW laser was locked to a transition in rubidium and the frequency was measured using the stabilised frequency comb as a “frequency ruler” extending across its emission bandwidth. The frequency was measured to an accuracy of 1 part in  $10^{11}$ , and fell within the uncertainty of the standard from the Comité International des Poids et Mesures (1997) [12]. In 2001 Udem *et al.* used a Ti:sapphire laser frequency comb to measure the absolute frequency of mercury and calcium optical clock transitions. The mercury transition was measured with an uncertainty of  $\sim 3$  Hz, making this the most accurate optical frequency measurement at that time [1, 13]. By 2004 frequency comb technology had developed for a range of lasers, including erbium fibre lasers in the near-infrared (IR) [14, 15].

Stabilised frequency combs have since been demonstrated for a range of measurements, including acting as a reference for a difference-frequency generator for spectroscopy on CO<sub>2</sub> transitions, and as the optical source for absorption spectroscopy with iodine [16]. Erbium fibre lasers allowed access to the region of the spectrum centred around 1.55  $\mu\text{m}$  for techniques such as cavity-ringdown spectroscopy with a range of gases [17] and broadband spectroscopy of hydrogen-cyanide with CW laser referenced frequency combs [18]. Other fibre lasers have also been used in the near-IR for applications including cavity-enhanced dual-comb spectroscopy, where sensitivity was increased through the use of an enhancement cavity [19].

### 1.3.2. Optical parametric oscillator frequency combs

The bandwidth of the stabilised CEO-frequency beat in lasers in the near-IR are typically poor compared to shorter wavelength lasers, with locked bandwidths in the region of 100's of kHz or MHz for Cr:forsterite and erbium-doped fibre lasers [20, 21]. These can be reduced with additional electronics [22], however using a laser at a visible wavelength to pump an optical parametric oscillator (OPO) can also give improved locking [23]. OPOs have the additional advantages that they can run over a very large range of wavelengths, and synchronously pumped femtosecond OPOs can be wavelength tuned by simply changing the OPO cavity length [24, 25]. Femtosecond OPOs can be configured as wavelength-tunable stabilised frequency combs, where changing a mirror set can lead to a very different signal wavelength. The laser used to pump the OPO can also be spectrally broadened to generate a supercontinuum, which can then be used to generate a beat frequency with different parts of the OPO spectra for convenient detection of CEO-frequencies for stabilisation [26, 27]. Table 1.1 summarises publications where CEO-frequency and repetition frequency behaviour have been investigated or stabilised in OPOs.

<u>Year</u>	<u>Authors/Title</u>	<u>Comments</u>
1999	Diddams <i>et al.</i> "Broadband optical frequency comb generation with a phase-modulated parametric oscillator"[28]	OPO pumped by stabilised CW laser. Phase modulator in OPO used to obtain stable broadband output. This was not a femtosecond OPO.
2000	Kobayashi <i>et al.</i> "Measurement of the optical phase relation among subharmonic pulses in a femtosecond optical parametric oscillator"[29]	Study of the phase relation between the pump, signal and idler pulses in a femtosecond OPO as cavity length was varied.
2001	Kobayashi <i>et al.</i> "Carrier-phase control among subharmonic pulses in a femtosecond optical parametric oscillator"[30]	CEO-frequency of the signal was locked relative to the CEO-frequency of the pump in a fs OPO. The CEO-frequencies of the pump, signal and idler pulse trains were a ratio of 3:2:1 respectively.
2003	Kobayashi <i>et al.</i> "Optical phase locking among femtosecond subharmonic pulses"[31]	CEO-frequency of the signal and idler were locked relative to the pump in a fs OPO. The relative CEP of signal and idler pulses were recovered for every 6th pulse, as with [30].
2003	Kobayashi <i>et al.</i> "Phase-coherent multicolor femtosecond pulse generation"[32]	Relative CEO-frequency stabilisation in a fs OPO was used to observe coherence in the time domain between the pump, signal and idler pulses.



2006	Sun <i>et al.</i> “Dual-color operation of a femtosecond optical parametric oscillator exhibiting stable relative carrier-envelope phase-slip frequencies”[33]	Demonstration of two co-resonant signal pulses in a fs OPO with separated centre wavelengths. The CEO-frequency difference between the signal outputs was controlled through variations in the cavity length.
2007	Sun <i>et al.</i> “Testing the parametric energy conservation law in a femtosecond optical parametric oscillator”[34]	CEO-frequencies of the pump, signal and idler were simultaneously measured in a free-running fs OPO. The relation between these phases was used to experimentally verify energy conservation in an OPO.
2007	Sun <i>et al.</i> “Coherent synthesis using carrier-envelope phase-controlled pulses from a dual-color femtosecond optical parametric oscillator”[35]	An AOM was used to shift the CEPS of two co-resonant signals in a fs OPO. When the CEO-frequency of both signals were matched, coherent synthesis of an ultrafast waveform was achieved.
2007	<b>Sun <i>et al.</i> “Composite frequency comb spanning 0.4-2.4 <math>\mu\text{m}</math> from a phase-controlled femtosecond Ti:sapphire laser and synchronously pumped optical parametric oscillator”[36]</b>	<b>Repetition frequency stabilised laser used to pump a fs OPO and PCF for supercontinuum generation. Two interferometers were used to heterodyne laser and OPO outputs with the supercontinuum for absolute CEO-frequency stabilisation to generate a fully stabilised OPO frequency comb.</b>
2008	Gebs <i>et al.</i> “1-GHz repetition rate femtosecond OPO with stabilized offset between signal and idler frequency combs”[37]	Demonstrated a synchronously pumped OPO with a 1 GHz repetition frequency. The difference between the CEO-frequencies of the signal and idler was stabilised to a frequency reference.
2008	Gale <i>et al.</i> “Towards versatile coherent pulse synthesis using femtosecond laser and optical parametric oscillators”[38]	A laser and synchronously pumped OPO were CEO-frequency stabilised and noise measurements were recorded for the locking. Coherence was shown for periods >20ms.
2008	<b>Reid <i>et al.</i> “Frequency Comb Generation and Carrier-Envelope Phase Control in Femtosecond Optical Parametric Oscillators”[27]</b>	<b>Review paper on CEO-frequency measurement and control in synchronously pumped fs OPOs.</b>
2008	Sun <i>et al.</i> “Control of the carrier-envelope phases of a synchronously pumped femtosecond optical parametric oscillator and its applications”[39]	Summary of results for CEO-frequency and repetition frequency control of a fs OPO and its pump laser for testing energy conservation, composite frequency comb generation and coherent pulse synthesis.
2008	Wong <i>et al.</i> “Self-phase-locked degenerate femtosecond optical parametric oscillator”[40]	Degenerate fs OPO with self-phase locking between the pump and signal/idler CEO-frequencies.
2009	Sun <i>et al.</i> “Coherent ultrafast pulse synthesis between an optical parametric oscillator and a laser”[10]	The CEO-frequencies of the pump, signal and idler in a fs OPO were stabilised and coherent pulse synthesis demonstrated between the pump and 2nd-harmonic of the signal pulses.

2009	Adler <i>et al.</i> “Phase-stabilized, 1.5 W frequency comb at 2.8-4.8 $\mu\text{m}$ ”[41]	Repetition frequency and CEO-frequency for a fs OPO operating in the mid-IR were stabilised to generate a fully stabilised comb.
2010	Adler <i>et al.</i> “Mid-infrared Fourier transform spectroscopy with a broadband frequency comb”[42]	A fully stabilised fs OPO frequency comb was used to take near-real-time broadband absorption spectra in the molecular fingerprint region of the mid-IR for a range of gases.
2010	Wong <i>et al.</i> “Self-phase-locked divide-by-2 optical parametric oscillator as a broadband frequency comb source”[43]	Frequency locking range for a degenerate fs OPO with self-phase locking between the pump and signal/idler CEO-frequencies was investigated.
2010	Ferreiro <i>et al.</i> “Locking the carrier-envelope-offset frequency of an optical parametric oscillator without f-2f self-referencing”[44]	CEO-frequency stabilisation of signal pulses from a fs OPO with a free-running pump. A simplified, lower noise locking technique was demonstrated compared with previous work.
2011	Ferreiro <i>et al.</i> “Frequency stability of a femtosecond optical parametric oscillator frequency comb”[23]	Repetition frequency stabilised laser used to pump a fs OPO with CEO-frequency stabilised signal. Noise measurements were recorded to calculate an upper limit on comb line stability of the OPO signal frequency comb.
2011	Reid <i>et al.</i> “Advances in ultrafast optical parametric oscillators”[45]	Review on ultrafast OPOs including CEO-frequency and wavelength stabilisation.
2011	Leindecker <i>et al.</i> “Broadband degenerate OPO for mid-infrared frequency comb generation”[46]	The cavity length of a broadband degenerate fs OPO in the mid-IR is stabilised to the pump laser.
2011	Vodopyanov <i>et al.</i> “Mid-IR frequency comb source spanning 4.4-5.4 $\mu\text{m}$ based on subharmonic GaAs optical parametric oscillator”[47]	Degenerate OPO centred at 4.9 $\mu\text{m}$ . Source suitable for stabilisation to generate locked frequency comb.
2012	Zhang <i>et al.</i> “Asynchronous midinfrared ultrafast optical parametric oscillator for dual-comb spectroscopy”[48]	The difference in frequency between two fs lasers was stabilised, and the lasers were used to synchronously pump an OPO to generate two asynchronous pulse trains. With CEO-frequency stabilisation, two mid-IR stabilised frequency combs with near-identical spectral properties could be achieved.
2012	McCracken <i>et al.</i> “Broadband phase coherence between an ultrafast laser and an OPO using lock-to-zero CEO stabilization”[11]	The pump, signal and idler in a fs OPO have been CEO-frequency stabilised to zero and phase coherence has been demonstrated. Outputs spanning nearly 3 $\mu\text{m}$ could be used to synthesise sub-optical cycle pulses.
2012	Vainio <i>et al.</i> “Degenerate 1 GHz repetition rate femtosecond optical parametric oscillator”[49]	Self-phase locked 1GHz degenerate fs OPO in the near-IR. Stabilisation of the pump laser would lead to a fully stabilised frequency comb.

2013	Lee <i>et al.</i> “Carrier envelope offset frequency of a doubly resonant, nondegenerate, mid-infrared GaAs optical parametric oscillator”[50]	A synchronously pumped, doubly resonant OPO was pumped by a fully stabilised laser. The relationship between the CEO-frequencies of the pump and signal pulse trains was investigated.
2013	Haakestad <i>et al.</i> “Intracavity trace molecular detection with a broadband mid-IR frequency comb source”[51]	Two near-degenerate fs OPOs were used for spectroscopy with a range of gases. The OPO cavity lengths were stabilised, however the pump lasers remained free-running.

*Table 1.1 Summary of publications presenting the development of partially and fully stabilised OPO frequency combs. The table includes investigations into CEO-frequency behaviour and the relationships between pump lasers and OPO outputs. Bold text is used for OPOs with both CEO-frequency and repetition frequency locked to a stable reference to generate a fully stabilised comb.*

In 1999 Diddams *et al.* presented a near-degenerate CW OPO modulated with an electro-optic phase modulator (EOM) to take advantage of parametric gain characteristics to obtain a stable broadband reference in the near-IR [28]. The CEO-frequency and repetition frequency were not stabilised to give a fully stabilised comb, however a stabilised CW laser was used to pump the OPO. The EOM was used to broaden the OPO spectrum which was then heterodyned with a stable single-frequency laser to verify the presence of sharp comb lines. Stabilisation of the OPO to a standard reference was discussed for future absolute frequency measurements. This work coincided with developments in stabilised frequency comb experiments and the demonstration of low dispersion microstructure fibres for the near-IR, which led to improved stabilisation of optical combs with significant simplification in the locking methods used.

In 2001 Kobayashi and Torizuka locked the CEO-frequency of the signal and idler pulses in a near-degenerate OPO based on KTiOPO<sub>4</sub> (KTP) relative to the CEO-frequency of the Ti:sapphire pump laser [30]. The pump laser was left free-running with neither the CEO-frequency nor the repetition frequency stabilised. The CEO-frequencies from the OPO were controlled using a feedback-loop to stabilise the cavity length of the OPO. In 2003, this work was built on by using an EOM to control the CEO-frequency of the pump laser and a piezo-electric transducer (PZT) to control the length of the pump laser relative to the OPO [31]. This was used to stabilise the pump, signal and idler outputs of the OPO relative to each other for long-term stabilisation.

Gebs *et al.* extended this work to a 1 GHz repetition frequency OPO based on periodically poled lithium niobate (PPLN) and pumped by a Ti:sapphire laser in 2008 [37]. They stabilised the difference between the CEO-frequencies of the signal and idler combs relative to a frequency reference. This difference-frequency was detected using the beat between the degenerate overlap of the signal and idler pulses. The frequency-doubled signal was also heterodyned with the depleted pump for comparison. In 2007 Sun *et al.* developed a CEO-frequency and repetition frequency stabilised OPO [36]. This was the first demonstration of absolute CEO-frequency stabilisation in a femtosecond OPO. A 200 MHz repetition frequency stabilised Ti:sapphire laser with a pulse duration of  $\sim 50$  fs was used to synchronously pump an MgO-doped PPLN-based OPO, with part of the laser output being broadened using a photonic crystal fibre (PCF). Two interferometers were used to heterodyne visible outputs from the laser and OPO with the supercontinuum generated in the PCF to obtain beat frequencies for stabilising the CEO-frequencies of all the pulse trains present. This resulted in a composite frequency comb with components spanning over a 2  $\mu\text{m}$  wavelength range [36]. In 2009 they demonstrated coherent pulse synthesis between an ultrafast laser and the second harmonic of signal pulses in an OPO based on these stabilisation techniques. Interference between the second harmonic signal pulses and residual pump supercontinuum gave clear fringes, indicating phase coherence between the stabilised pulses [10]. A second-order two-photon absorption autocorrelator was used to verify constructive interference between the parent pulses to synthesize coherent daughter pulses. When the different frequency components were stabilised, the intensity of the signal in the autocorrelation trace increased significantly and an 8:1 contrast ratio was achieved.

Recent research in frequency combs has focused at longer wavelengths in the mid-IR molecular ‘fingerprint’ region (2 – 20  $\mu\text{m}$ ) of the spectrum [52]. These optical frequencies correspond to strong characteristic vibrational transitions in many molecules and so have applications in studies on the structure and behaviour of molecular structures, and non-invasive diagnostics of solids, liquids and gases. Parts of this region also coincide with transparency in the Earth’s atmosphere and so can be used for trace gas detection in atmospheric, security and industrial monitoring applications. OPOs can provide a convenient method for obtaining stabilised frequency combs in the mid-IR region of the spectrum [52].

In 2009 Adler *et al.* demonstrated a high power fully stabilised OPO frequency comb with idler pulses tunable from 2.8 – 4.8  $\mu\text{m}$  [41]. A Yb:fibre laser was repetition frequency stabilised and used to synchronously pump an MgO-doped PPLN-based OPO. The pump and signal CEO-frequencies were locked to stabilise the CEO-frequencies of all the OPO outputs. This comb was used to take near-real-time broadband absorption spectra in the molecular fingerprint region of the mid-IR for a range of gases [42].

Gallium arsenide (GaAs) has also been used successfully in OPOs for mid-IR frequency comb generation. A 182 MHz, 100 fs  $\text{Cr}^{2+}:\text{ZnSe}$  laser centred at 2.45  $\mu\text{m}$  was used to synchronously pump a degenerate OPO [47]. This was a ring bow-tie cavity based on quasi-phase matched orientation-patterned (OP) GaAs. The OPO had a spectral bandwidth of 1  $\mu\text{m}$ , which was double the pump bandwidth in frequency units. The stabilisation of the CEO-frequencies was based on the same techniques that had been used previously for an erbium-fibre laser pumped MgO-doped PPLN ring OPO with an output extending from 2.5 – 3.8  $\mu\text{m}$  [46], and a Ti:sapphire pumped MgO-doped PPLN OPO operating at  $\sim 1550$  nm with a FWHM bandwidth of 50 nm [43].

In 2013, Haakestad *et al.* performed mid-IR intracavity spectroscopy of methanol, isotropic carbon monoxide, carbon monoxide, formaldehyde, acetylene and ethylene using two broadband near-degenerate OPOs [51]. One of these was based on PPLN and pumped using an erbium fibre laser at 1560 nm with a repetition frequency of 80 MHz and an 85 fs pulse duration [46]. The OPO output was centred at 3.1  $\mu\text{m}$ . The other system was based on OP-GaAs and was pumped by a thulium fibre laser at 2.05  $\mu\text{m}$  with a 75 MHz repetition frequency and 93 fs pulse duration [53]. This OPO output was centred at 4.1  $\mu\text{m}$ . Both pump lasers were left free-running. The large instantaneous bandwidths of both OPOs allowed for the detection of multiple gases simultaneously with high sensitivity levels. The gases were investigated by either injecting them directly into the OPO enclosure, or by using an intracavity gas cell, and their spectra were measured using a commercial Fourier transform IR spectrometer for total measurement periods ranging from 30 s to 4 min. The OPOs were locked to an appropriate oscillation peak using dither locking for these measurements [51].

An alternative method for mid-IR spectroscopy measurements is using two frequency combs with a controlled offset between their repetition frequencies. Zhang *et al.* at Heriot-Watt University have reported a system with two modelocked Yb:KYW lasers where the difference between the repetition frequency of the two lasers has been

directly stabilised. For this technique, one of the laser frequency combs acts as a signal that is probed by the second frequency comb, which acts as a local oscillator. The beat frequency between the two combs constitutes a radio-frequency comb with a repetition frequency equal to the difference in repetition frequency of the two optical combs. The repetition frequencies of the two lasers were detected, mixed and low-pass filtered to give a sine wave at a frequency equal to the difference between the laser repetition frequencies. This was then stabilised to a reference frequency using a phase frequency detector which fed back to a PZT in one of the lasers which controlled the cavity length [54]. Using an OPO design previously reported [55], these lasers were then used to simultaneously synchronously pump the single OPO cavity to generate asynchronous mid-IR pulse trains for the signal/idler pulses. Repetition frequency differences between the lasers ranging from 20 Hz to 10 kHz were investigated [48]. For future work the CEO-frequency of the outputs from this OPO will be stabilised to enable dual frequency comb spectroscopy in the mid-IR.

Optical parametric oscillators have proven to be suitable sources for spectroscopic measurements or for use as stabilised frequency combs. To date, however, there has been only limited work carried out to investigate the use of OPO outputs for spectroscopic measurements when they are fully stabilised combs.

#### **1.4. Thesis outline**

When I joined the Ultrafast Optics group at Heriot-Watt University, there was ongoing research into OPOs as stabilised frequency combs. Previous work by Sun *et al.* described in Section 1.3 had presented Ti:sapphire pumped stabilised OPO frequency combs in the visible and near-IR regions of the spectrum. This work was used as a basis for my project, utilising existing electronics for the stabilisation feedback loops and implementing similar cavity designs.

This thesis presents results for the design and characterisation of a 280 MHz ring Ti:sapphire laser pumping an OPO which is controlled to obtain a stabilised frequency comb. The laser was also used to pump a photonic crystal fibre for spectral broadening and supercontinuum generation. The non-phasematched outputs from the OPO included sum frequency mixing of the pump and signal, which was used with the pump supercontinuum to measure the CEO-frequency of the signal pulses. The CEO-frequency stabilisation technique was simplified to reduce the complexity of the system compared to similar sources and a range of noise and stability characterisation

measurements were used to demonstrate the high performance of this stabilised frequency comb. An external cavity diode laser was stabilised using dither locking to generate a stable high-precision optical reference suitable for use in stabilisation or noise measurements with the OPO frequency comb. The stabilised OPO frequency comb was mode filtered to increase the comb line separation using a filter cavity stabilised using the same technique.

Chapter 2 introduces the concept of modelocking lasers and ultrashort pulses and gives details for the requirements of a laser synchronously pumping an ultrafast OPO. Nonlinear optics in OPOs and the different frequencies that can be generated are outlined with details of CEO-frequency control in synchronously pumped OPOs. The performance of the laser and OPO are characterised to confirm their suitability for use in a stabilised frequency comb system.

Chapter 3 details the nonlinear interferometer used for CEO-frequency detection and the electronic feedback loops used for stabilising the CEO-frequency and repetition frequency for signal pulses from the OPO. Noise analysis is presented for the two stabilisation loops and an upper limit for the overall frequency comb instability is calculated.

Chapter 4 presents an external cavity diode laser stabilised to a saturated absorption peak in rubidium via dither locking. Results are given for relative intensity noise measurements to support the suitability of this system as a high-precision optical frequency reference for a stabilised frequency comb.

Chapter 5 reports preliminary results for filtering the stabilised OPO frequency comb using an external cavity. The cavity length is stabilised to a harmonic of the OPO using dither locking so the transmitted frequency comb has an increased mode separation of 1.4 GHz. Radio-frequency and optical spectra are presented for the filtered comb and several changes are suggested to improve both the short and long-term stability of the final frequency comb.

Chapter 6 outlines the main conclusions from the work presented in this thesis and details a selection of changes and developments that could lead to an improved source for frequency comb spectroscopy and metrology.

## **Chapter 2. Design and characterisation of a Ti:sapphire-pumped optical parametric oscillator**

In this chapter I will give details of the frequency comb optical parametric oscillator (OPO) source. The frequency comb needed to have a relatively high average power and repetition frequency and to generate femtosecond pulses. An OPO was chosen for the frequency comb and it was pumped by a repetition frequency-stabilised ‘home-built’ Ti:sapphire laser. In Section 2.1, the Ti:sapphire laser design considerations and final configuration are described. Section 2.2 presents the OPO that is the source of the frequency comb. The electronics used to lock the Ti:sapphire laser and OPO to make a stabilised comb will be detailed in Chapter 3.

### **2.1. Ti:sapphire laser**

Low-noise frequency combs require stable pump sources. Frequency combs with high repetition frequencies are useful in many applications, such as spectroscopy, as the increased mode spacing can enable resolving of the individual comb modes [56]. The Ti:sapphire laser therefore needs to be at a high repetition frequency and to have a sufficiently high peak power and short pulse duration to pump an OPO with a sufficient output power and a photonic crystal fibre (PCF) for supercontinuum generation. The laser needs to operate in the femtosecond regime and the design should have minimal complexity to result in a low-noise, simple and stable cavity. The repetition frequency of the laser must be stabilized to make the OPO into a stabilised frequency comb, however the carrier-envelope-offset frequency can be left free-running in the laser.

#### **2.1.1. Modelocking**

Modelocking [57] is a range of techniques used to generate ultrashort pulses, which are required to pump a femtosecond OPO. An active element [58], such as an optical modulator, or a nonlinear passive element [59], such as a saturable absorber, causes an ultrashort pulse to be formed and to circulate in a laser cavity. These elements are used to ensure the cavity loss is higher for continuous-wave (CW) as opposed to pulsed signals, and that there is a loss advantage for short pulses over long pulses [60]. Care must be taken in the design of the laser and saturable absorber to ensure the intra-cavity



pulse energy remains stable, this is CW modelocking. Failure to do so results in large oscillations in some pulse parameters (e.g. energy, spectral bandwidth and time duration), this is Q-switched modelocking, see Figures 2.1(a) and 2.1(b) [61].

A pulse is emitted each time the circulating pulse hits the output coupler, so a regular pulse train, the peaks of which are separated by the cavity round-trip time, is created. During the time in between these events, the output of the laser through the output coupler is approximately zero. This can result in very high peak powers, which can be utilised in nonlinear media.

Mode locking in the frequency domain means the laser is operating on a number of axial cavity modes, which oscillate with near-identical phase. By maintaining this phase relationship, short pulses can be produced with pulse duration inversely proportional to the locked bandwidth (by the time-bandwidth product [62]), which is the product of the number of locked modes and the mode frequency spacing. The axial mode amplitudes constructively interfere with spacing equal to the repetition frequency of the laser.

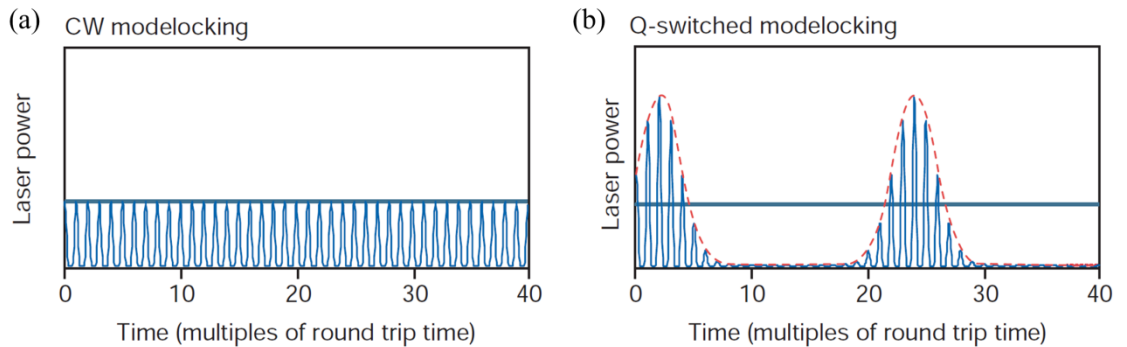


*Figure 2.1(a) Regular pulses of equal intensity resulting from CW modelocking. (b) The varying intensity within a group of pulses under a Q-switched envelope. Both images taken from [61].*

Typically, many frequencies can oscillate within a laser, as long as they are within the emission bandwidth and correspond to longitudinal modes of the laser cavity [63]. The modelocked condition requires that these modes maintain a fixed phase separation.

If we consider the total electric field output as a function of time from a laser, where the  $n^{th}$  mode has amplitude  $(E_0)_n$ , angular frequency  $\omega_n$  and phase  $\delta_n$ :

$$E(t) = \sum_{n=0}^{N-1} (E_0)_n \exp[i(\omega_n t + \delta_n)] \quad \text{Equation 2.1}$$

where amplitude, angular frequency and phase can vary over time [64]. This will result in a total irradiance that is the sum of the irradiance of all the incoherent modes.

If instead the modes were forced into coherence, i.e. have a fixed phase relationship, so  $\delta_n$  becomes a fixed  $\delta$ , then the total irradiance becomes the square of the sum of the individual modes' electric fields. Equation 2.1 can be further simplified by assuming that  $N$  modes have the same amplitude,  $E_0$ , giving a total electric field:

$$E(t) = E_0 \exp(i\delta) \sum_{n=0}^{N-1} \exp(i\omega_n t) \quad \text{Equation 2.2}$$

If  $\omega$  is the angular frequency of the highest frequency emitted mode and the separation in angular frequency between two adjacent modes is  $\delta\omega$ , then  $\omega_n = \omega - n\delta\omega$ . With  $l$  as the optical path length between the end mirrors of a standing wave cavity, then [64]:

$$\delta\omega = \frac{\pi c}{l} \quad \text{Equation 2.3}$$

Equation 2.2 can now be written in terms of  $\delta\omega$  and Equation 2.3:

$$\begin{aligned} E(t) &= E_0 \exp(i\delta) \sum_{n=0}^{N-1} \exp[i(\omega - n\delta\omega)t] \\ &= E_0 \exp[i(\omega t + \delta)] \sum_{n=0}^{N-1} \exp(-i\pi nct/l) \end{aligned} \quad \text{Equation 2.4}$$

This can be expressed as a geometric series, substituting  $a = \pi ct/l$  to give [64]:

$$\begin{aligned} E(t) &= E_0 \exp[i(\omega t + \delta)] \{1 + \exp(-ia) + \exp(-2ia) + \dots \\ &\dots + \exp[-(N-1)ia]\} \end{aligned} \quad \text{Equation 2.5}$$

Equation 2.5 can then be rewritten as:

$$E(t) = E_0 \exp[i(\omega t + \delta)] \frac{\sin(Na/2)}{\sin(a/2)} \quad \text{Equation 2.6}$$

This will give as irradiance,  $I$ , such that [64]:

$$I(t) = E(t) \cdot E(t)^* = E_0^2 \frac{\sin^2(Na/2)}{\sin^2(a/2)} \quad \text{Equation 2.7}$$

The irradiance is periodic and will have a maximum equal to  $E_0^2 N^2$  when  $a = 0$  or  $2b\pi$  for a non-zero integer  $b$ , corresponding to a time period  $T = 2l/c$ , which is the time taken for light to travel one round trip within the cavity. It will also have a minimum of zero when  $a = (2b+1)\pi$ , or at time  $t = (2b+1)l/c$ . So a modelocked laser will have a periodic train of short pulses with a peak power that is the product of the number of modes,  $N$ , and the average power, occurring at intervals,  $T$ , or  $2\pi/\delta\omega$  [64].

For ultrashort pulses, many modes need to be oscillating and locked together. This depends on the gain medium having a large emission bandwidth.

### Active and passive modelocking

Modelocking of a laser can be achieved using active or passive methods. Active modelocking can use an externally driven device to modulate the intra-cavity loss (amplitude modulation) or the intra-cavity phase (frequency modulation) of a laser, such as with an acousto- or electro-optic modulator [65]. For example, a cavity can have an electronically-driven modulator that gives a sinusoidal loss modulation with a period corresponding to the cavity round trip time. The steady-state saturated gain supports net gain around the minimum of the loss modulation (see Figure 2.2). Only pulses that are much shorter than the round trip time can be supported. With active modelocking it is difficult to generate sub-picosecond pulses, as your pulse duration is generally limited by the speed of your control electronics.

Passive modelocking can be achieved using any device in a laser cavity with a power-dependent gain or loss. The process of modelocking can be understood in terms of dynamic loss saturation, or in some cases, with dynamic gain saturation. The main element used for this is a saturable absorber. Saturable absorbers give a loss that decreases with increasing incident pulse intensity and can take the form of a physical device, such as a dye or semiconductor saturable absorber mirror (SESAM), or a virtual device, such as with Kerr lens modelocking [60]. Saturable absorbers can be used to generate ultrashort pulses through different regimes depending on whether their action is fast or slow.

A dye can be selected with an absorption band corresponding to the laser transition frequency. It will be opaque at low irradiances as the unexcited molecules absorb the photons. With increasing intensity the excited states are populated until the dye becomes transparent. The dye is now bleached [64]. To see how modelocking develops, we start with a laser operating in CW with this saturable absorber in the cavity. The saturable absorber will advantage small noise spikes in the intensity over the CW background. The spikes will then grow faster until they contain a significant proportion of the energy circulating in the cavity and saturate the gain, causing a decay in the background propagating CW. The most energetic noise spike will experience the least saturable absorption and saturate the gain so all the other spikes see net loss with each round trip, leading to a single circulating pulse. A fast saturable absorber will favour the higher intensity peak over the wings of the pulse, so its duration will be shortened in time for each round trip until pulse temporal broadening effects, such as dispersion, lead to a stable state (see Figure 2.2) [60]. With slow saturable absorbers, the period of low loss is greater than the pulse duration. Ultrashort pulses can still be generated if there is dynamic gain saturation, so the gain is significantly reduced for the tail of the pulse [66]. They can also be generated from a gain medium with steady state gain saturation if the saturable absorber absorbs the leading edge of the pulse at the same rate at which the tail of the pulse grows [66].

Fast saturable absorbers (short recovery time) can be the best for ultrashort pulses down to  $\sim 100$  fs, but below this the choice of fast saturable absorbers is very limited, which is why slow saturable absorbers (e.g. SESAMS) are dominant [60]. One exception to this is Kerr lens modelocking, where a Kerr lens medium acts as a very fast saturable absorber [67].

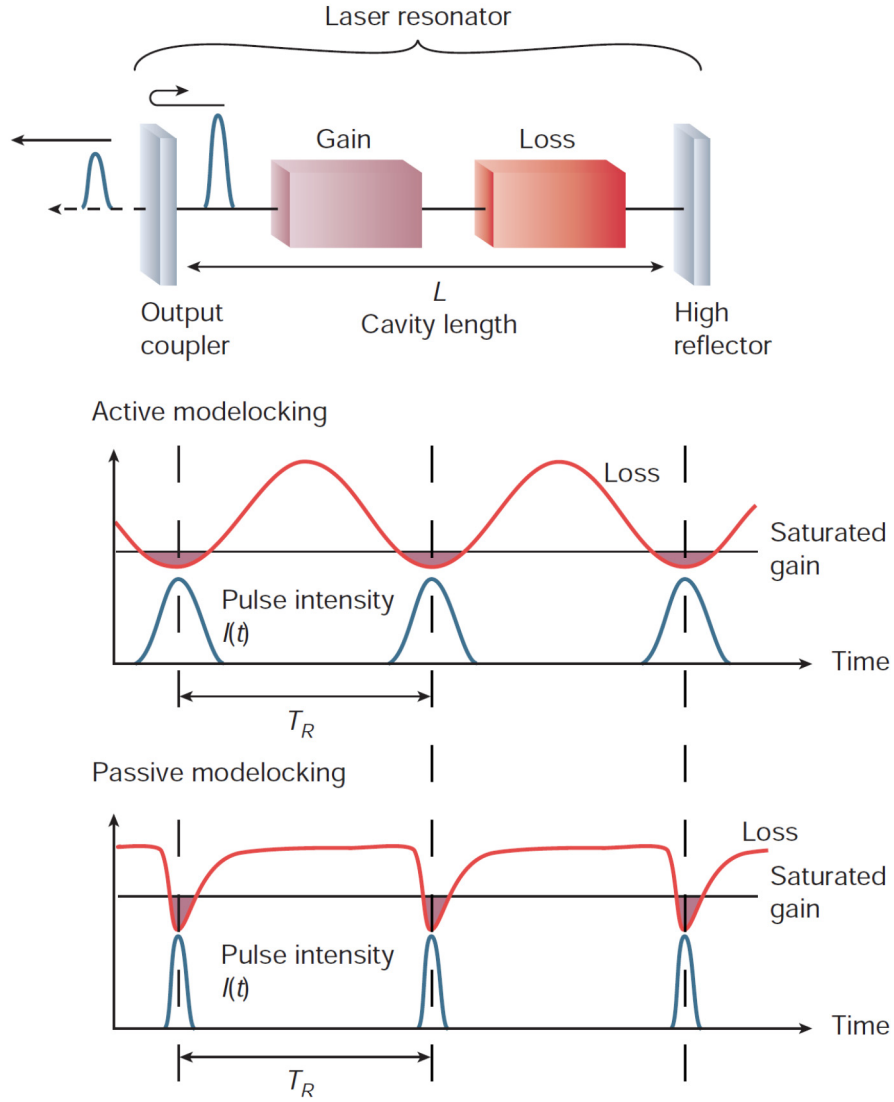


Figure 2.2 Active and passive modelocking in a laser cavity. The modulation of gain or loss in a cavity shapes the intensity of the light emitted (top). This can be done using active modelocking, where the losses are decreased using an externally controlled device (centre). In passive modelocking the intensity of light in a cavity determines the loss it undergoes, so high intensity fluctuations see less loss than low intensity background (bottom), leading to pulses limited in length by other pulse broadening effects in the cavity. Diagrams taken from [61].

### 2.1.2. Design considerations for an ultrafast modelocked laser

Ultrashort pulses are shaped in space, time and frequency by the media through which they propagate. An ultrafast laser that is used as a frequency comb requires stable modelocking with pulse envelopes that do not vary over time. The design of the laser will need to take into account these criteria when components are chosen.

### Stable modelocking

Many transverse modes can oscillate within a laser cavity. Any higher order transverse modes (above the fundamental) in the cavity will have different resonant frequencies. The result is that if they contain too much of the laser power, the periodic constructive interference of cavity modes won't be possible. Thus, for stable modelocking, it is usually necessary to operate on the fundamental transverse cavity mode, TEM<sub>00</sub>.

Higher repetition rates in modelocked lasers can be achieved using harmonic modelocking, where a modelocked laser is operating with the fundamental transverse mode, but has many pulses circulating simultaneously within the cavity [60]. For example, with second harmonic modelocking, there are two pulses circulating within the laser cavity [68]. Unless additional sophisticated methods such as filters and electronic feedback are used to control the pulses, they can vary in energy and phase, and the period between them can also fluctuate. This is not ideal in a simple frequency comb pump. Using a ring cavity design rather than a standing wave cavity can reduce the incidence of multi-pulsing for high pump powers [69].

### Gain media

The gain medium in a laser needs a pump transition corresponding to the output of an available pump source and a laser transition at a useful wavelength. A small quantum defect, no parasitic losses and high gain are also important. Good thermal conductivity, weak temperature dependence for the refractive index and resistance to heat damage are desirable for high-power operation. For ultrafast lasers, a broad emission bandwidth is necessary, due to the limitation of pulse duration with the time-bandwidth product. The laser cross section needs to be large enough that Q-switching can be easily overcome in passive modelocking, especially in higher repetition rate cavities, and the pump beam quality should be high [60].

Gain media for ultrashort pulse generation typically have very broad amplification bandwidths, but poor thermal properties and smaller than ideal laser cross sections. An exception to this is titanium-doped sapphire (Ti:sapphire), which has many ideal characteristics, although the quantum defect is large and the absorption spectrum necessitates the use of more expensive frequency-doubled solid-state pump sources rather than direct diode pumping [60, 70].

## Dispersion

Another consideration for ultrashort pulse generation is dispersion within the laser cavity. For ultrafast lasers we need to consider chromatic dispersion caused by the material properties of the cavity components.

If there is no chirp on an ultrashort laser pulse then the duration bandwidth product is transform limited (see Figure 2.3). The time-bandwidth product is defined as the product of the full-width at half-maximum (FWHM) of the frequency spectrum and the time duration,  $\Delta\omega\Delta\tau$ . It is equal to 2.77 for pulses with a Gaussian shape in time and 1.98 for  $\text{sech}^2$  pulses. However, when this pulse passes through a medium where dispersion is present, it will cause a phase shift on the pulse (see Equation 2.16), and there will arise a frequency chirp in time. The pulse duration will therefore increase. For ultrashort lasers, shorter pulses possess a larger frequency bandwidth and are subject to greater temporal broadening; dispersion within an ultrafast laser cavity must be carefully controlled to ensure short pulse durations.

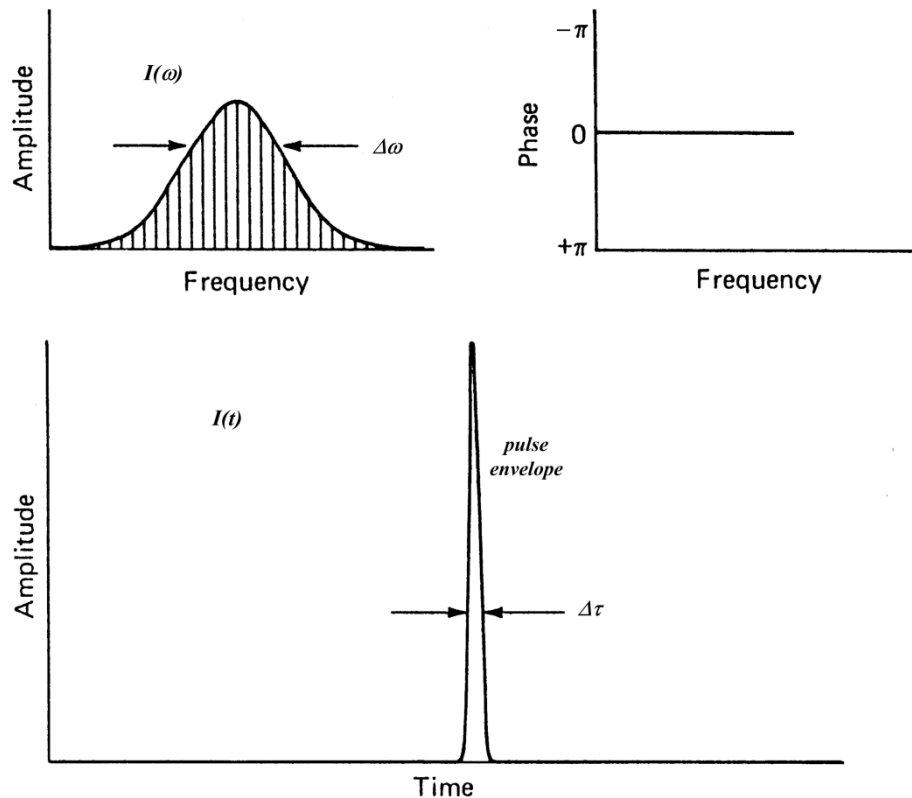


*Figure 2.3 Ideal transform limited pulse. In most systems the pulse will experience some dispersion so there will be some chirp on the pulse and a frequency-dependent phase. Diagram adapted from [67].*

For an arbitrary ultrashort pulse, in the frequency domain it can be considered to have an envelope centred at an angular frequency,  $\omega_0$ , with an electric field,  $E$  with complex amplitude  $A$  such that:

$$E(t) = A(t)e^{-i\omega_0 t} \quad \text{Equation 2.8}$$

This can pass through a dispersive material with a refractive index,  $n$ . The refractive index is determined by the square of the ratio of frequency-dependent electric permittivity,  $\epsilon$ , and magnetic permeability,  $\mu$ , of the material with the permittivity,  $\epsilon_0$ , and permeability,  $\mu_0$ , of a vacuum, such that:

$$n = \sqrt{\frac{\mu\epsilon}{\mu_0\epsilon_0}} \quad \text{Equation 2.9}$$

The refractive index can also be defined as the ratio between the speed of light in a vacuum,  $c$ , and the phase velocity,  $v_{ph}$ , of the carrier wave of the light in the material. The phase velocity is the velocity of the wavefronts for a single frequency component of the wave.

$$v_{ph} = c/n \quad \text{Equation 2.10}$$

For most optical materials,  $\mu = \mu_0$ , as they are non-magnetic, however the electric permittivity is a function of the angular frequency  $\omega$  of the light [71]. This means the refractive index (and phase velocity) are dependent on the frequency of a particular component of the wave. The wavenumber,  $k$ , can also be expressed in terms of the frequency-dependent refractive index:

$$k = n(\omega) \frac{\omega}{c} \quad \text{Equation 2.11}$$

An ultrashort pulse in a material can be described as having an envelope (see Figure 2.3) that travels at a group velocity,  $v_g$ , such that:

$$v_g = \frac{d\omega}{dk} = \frac{c}{n(\omega) + \omega \frac{dn}{d\omega}} \quad \text{Equation 2.12}$$

We can now define a group refractive index,  $n_g$ , analogous to the refractive index being defined in terms of phase velocity, where:

$$n_g = \frac{c}{v_g} = n(\omega) + \omega \frac{dn}{d\omega} \quad \text{Equation 2.13}$$

The envelope has a group delay,  $\tau_g$ , which is the time taken for the pulse to cover a distance,  $l$ , in the medium:



$$\tau_g = \frac{d\phi}{d\omega} = \frac{l}{v_g} \quad \text{Equation 2.14}$$

where  $\phi$  is the spectral phase, or phase of the electric field in the frequency domain [71].

From Equation 2.14 we can see that a pulse travelling through a gain medium, or any other optics, will acquire a phase shift. For narrow spectral bandwidths, the phase shift,  $\phi$ , can be viewed as linearly-dependent on frequency and causes a time-delay whilst maintaining the temporal shape of the pulse. For a medium of length,  $L$ , with a real part of its refractive index,  $n_0$ , the optical phase is:

$$\phi(\omega) = \frac{n_0 \omega L}{c} \quad \text{Equation 2.15}$$

For ultrashort pulses we must consider the higher order terms. If we take the central angular frequency of a pulse to be  $\omega_0$ , then the phase shift,  $\phi(\omega)$ , can be extended in a Taylor series about this [60]:

$$\phi(\omega) = \phi_0 + \frac{\partial \phi}{\partial \omega} (\omega - \omega_0) + \frac{1}{2} \left[ \frac{\partial^2 \phi}{\partial \omega^2} (\omega - \omega_0)^2 \right] + \frac{1}{6} \left[ \frac{\partial^3 \phi}{\partial \omega^3} (\omega - \omega_0)^3 \right] + \dots \quad \text{Equation 2.16}$$

The first term is a common phase shift, the second term contains the group delay and the third term is the group delay dispersion (GDD) – often referred to as 2<sup>nd</sup> order dispersion. Optical elements have a GDD defined for the entire substrate. Second order dispersion can also be defined per unit length of a material as the group velocity dispersion, or GVD. This is normally given in units of fs<sup>2</sup>/mm. There are also higher order terms, third order dispersion etc. With shorter pulses, higher order phase shifts modify the pulse shape, and for ultrashort pulses, which will have the largest bandwidths, the most higher order phase shifts will apply, causing increased distortion of the pulses [60].

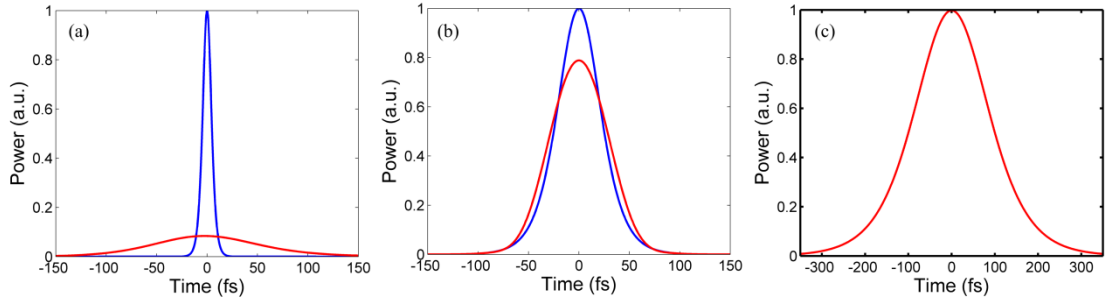


*Figure 2.4 Temporal pulse broadening for initially bandwidth limited ultrashort pulses with  $\text{sech}^2$  temporal pulse profile, centred at 790 nm and passing through 10 mm of a sapphire crystal. Blue is original pulse, red is chirped pulse at end of crystal. (a) Pulse with 10 fs FWHM gains large chirp and significantly reduced peak power. (b) 50 fs pulse sees some temporal broadening and  $\sim 25\%$  reduction in peak power. (c) 200 fs pulse sees almost no change after 10 mm of crystal.*

Figure 2.4 shows three graphs calculated in Matlab illustrating the duration of three pulses before and after they have propagated through 10 mm of sapphire crystal. The Sellmeier equation and coefficients were taken from a paper by Zhao *et al.* [72], and their work was based on the data in the *Handbook of Optics* [73]. The Sellmeier equation was used to calculate the refractive index for a range of optical frequencies in the medium. Duration transform-limited pulses were then generated for 10, 50 and 200 fs FWHM and  $\text{sech}^2$  temporal shape, centred at 790 nm, and propagated through 10 mm of sapphire crystal. The graphs in Figure 2.4 show how dispersion control becomes more important with decreasing pulse duration.

### Introduction to nonlinear optics: Kerr nonlinearity and Kerr lens modelocking

When electric fields are incident upon a dielectric material, the displacement of valence electrons from their original orbits forms electric dipoles, which is observed as polarisation. For a sufficiently intense electric field, the polarisation is not proportional to the incident sinusoidal wave and the dipoles radiate a wave differing from the original. This electric field can contain new frequencies. Polarisation for a dielectric material (where we ignore magnetic effects) can be expanded as a series [74]:

$$\vec{P} = \epsilon_0 \chi_{\text{linear}}^{(1)} \vec{E} + \epsilon_0 \chi^{(2)} \vec{E}^2 + \epsilon_0 \chi^{(3)} \vec{E}^3 + \dots \quad \text{Equation 2.17}$$

where  $\vec{E}$  is the electric field,  $\chi^{(1)}$  is the linear susceptibility and  $\chi^{(2)}$ ,  $\chi^{(3)}$  are the second and third order nonlinear susceptibilities respectively [75]. The fields in Equation 2.17

are vectors, so the nonlinear susceptibilities are tensors, however here I have assumed  $P$  and  $E$  to be scalar quantities to simplify how this nonlinearity can be described.

Passive modelocking can be achieved using the third-order nonlinearities present in all optical materials. Ultrafast lasers usually have high intra-cavity intensities, enabling access to higher order nonlinear effects.

The polarisation of an isotropic optical material ( $\chi^{(2)} = 0$ ), where we ignore higher order nonlinearities, can be written as:

$$P = \epsilon_0(\chi^{(1)}E + \chi^{(3)}E^3) = P^{(1)} + P^{(3)} \quad \text{Equation 2.18}$$

Considering only the  $P^{(3)}$  term, and assuming a monochromatic electric field:

$$E(t) = \epsilon \cos(\omega t) \quad \text{Equation 2.19}$$

where  $\epsilon$  is the amplitude of the electric field,  $\omega$  is the angular frequency of oscillation and  $t$  is time. Using the identity:  $\cos^3(x) = \frac{1}{4}\cos(3x) + \frac{3}{4}\cos(x)$ , the  $P^{(3)}$  term can be written as:

$$P^{(3)} = \epsilon_0\chi^{(3)}E^3 = \epsilon_0\chi^{(3)}\epsilon^3 \left( \frac{1}{4}\cos(3\omega t) + \frac{3}{4}\cos(\omega t) \right) \quad \text{Equation 2.20}$$

There is a term oscillating at the third harmonic and a term operating at the fundamental, this is the Kerr term. The polarisation can now be written as:

$$P = \epsilon_0\chi^{(1)}E + \frac{3}{4}\epsilon_0\chi^{(3)}\epsilon^2 E + \frac{1}{4}\epsilon_0\chi^{(3)}\epsilon^3 \cos(3\omega t) + \dots \quad \text{Equation 2.21}$$

In the absence of phase matching, the time-averaged transfer of energy through the third harmonic term is very small, so will be neglected:

$$P = \epsilon_0\chi^{(1)}E + \frac{3}{4}\epsilon_0\chi^{(3)}\epsilon^2 E = \epsilon_0E(\chi^{(1)} + \frac{3}{4}\chi^{(3)}\epsilon^2) \quad \text{Equation 2.22}$$

The linear refractive index can be expressed as  $n_0 = (1 + \chi^{(1)})^{1/2}$ , and by analogy we can derive intensity dependent refractive index:

$$n = (1 + \frac{P}{\epsilon_0 E})^{1/2} = (1 + \chi^{(1)} + \frac{3}{4}\chi^{(3)}\epsilon^2)^{1/2} = (1 + \chi_L + \chi_{NL})^{1/2} \quad \text{Equation 2.23}$$

Let  $(1 + \chi_L) = b$

$$n = (b + \chi_{NL})^{1/2} \quad \text{Equation 2.24}$$

If  $\chi_{NL} \ll b$  then a binomial expansion can be used:

$$(1 + x)^a = \sum_{k=0}^{\infty} \binom{a}{k} x^k = 1 + ax + \frac{a(a-1)}{2!}x^2 + \dots \quad \text{which can be used to obtain:}$$

$$n = (b + \chi_{NL})^{\frac{1}{2}} = b^{\frac{1}{2}}(1 + \frac{\chi_{NL}}{b})^{\frac{1}{2}} \quad \text{Equation 2.25}$$

Using the binomial expansion:

$$n \approx b^{\frac{1}{2}} \left(1 + \frac{1}{2} \frac{\chi_{NL}}{b}\right) = b^{\frac{1}{2}} + \frac{1}{2} \left(\frac{\chi_{NL}}{b^{\frac{1}{2}}}\right) \quad \text{Equation 2.26}$$

However  $b^{\frac{1}{2}} = (1 + \chi_L)^{\frac{1}{2}} = n_0$ , so

$$n = n_0 + \frac{1}{2} \left(\frac{\chi_{NL}}{n_0}\right) \quad \text{Equation 2.27}$$

From Equation 2.23,  $\chi_{NL} = \frac{3}{4} \chi^{(3)} \epsilon^2$ , so:

$$n = n_0 + \frac{1}{2} \left(\frac{3}{4} \frac{\chi^{(3)} \epsilon^2}{n_0}\right) = n_0 + \frac{3}{8} \frac{\chi^{(3)} \epsilon^2}{n_0} \quad \text{Equation 2.28}$$

where the second term is a refractive index increment dependent on the square of the electric field, the intensity. The refractive index can therefore be written as:

$$n = n_0 + n_2 I \quad \text{Equation 2.29}$$

where  $n_2$  is material dependent and also has a wavelength dependence [60]. This shows that the refractive index is dependent on the intensity when there is a third order nonlinearity. This is the optical Kerr effect. The nonlinear changes in refractive index cause two effects in a pulse. In space, a gradient across the transverse index as a result of the higher intensities present at the centre of a wavefront focuses the pulse to a smaller beam waist. Temporally, the Kerr effect causes self-phase modulation (SPM) [60].

The first effect – where there is intensity dependent focussing of the beam – is Kerr lensing. In the case of a plane wave with a Gaussian profile passing through a material with a Kerr nonlinearity, the intensity is highest in the centre of the wavefront and reduces towards the edges, causing the refractive index of the material to change across its width accordingly. This difference in refractive index changes the optical path length across the wavefront, as a positive lens would (for a positive Kerr nonlinearity), focussing the light. By placing an aperture after the Kerr medium, the highest intensity will pass through most efficiently. In Kerr lens modelocking (KLM), the gain medium also acts as a Kerr lens and can act as a fast saturable absorber to make sub-10 fs pulses. For most gain media, the Kerr effect will have a time constant of the order of a femtosecond [60], and this effect means pulses experience higher gain or lower loss than CW circulating light [76]. This can be used in two ways: soft aperture

modelocking and hard aperture modelocking. In hard aperture KLM a physical aperture is used to increase the loss of the less-focussed CW light (see Figure 2.5). This spatially-dependent loss enables modelocking like a fast saturable absorber. In soft aperture KLM the pump beam is more tightly focussed in the gain medium than the laser transverse spacial modes. The Kerr lensing effect increases the gain for modelocked pulses by improving the overlap between the pump and these laser modes compared to the less tightly focussed CW light. This normally necessitates operating the laser at one edge of the stability range to ensure a sufficient change in mode size to give a significant change in overlap [61].

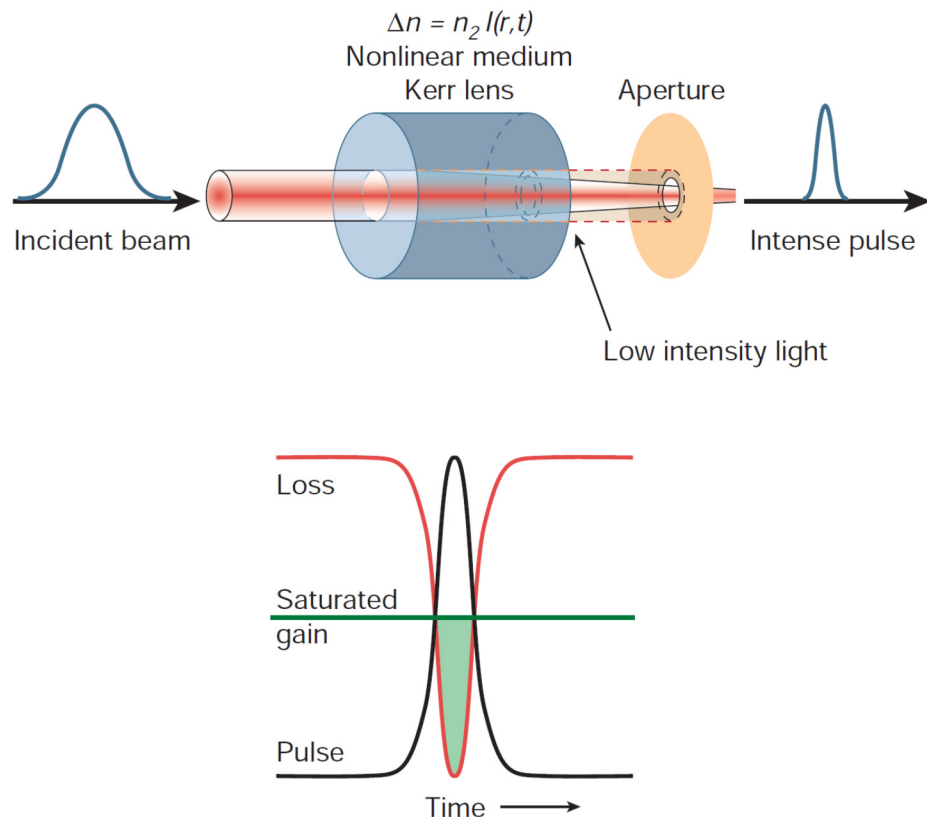


*Figure 2.5 Kerr lens modelocking with the use of a hard aperture. The lower intensity background experiences less focussing in the medium so it is blocked by the aperture acting as a high loss component. Diagram taken from [61].*

A disadvantage of Kerr lens modelocking is that it is not usually self-starting and requires a noise spike, caused by something like a tap of a mirror, to initiate the modelocking. Self-starting involves careful alignment of the laser and is rarely compatible with the shortest pulse durations [60].

The other consequence of the Kerr effect is SPM, where the optical pulse will undergo a change in phase,  $\phi(t)$ , as a result of a nonlinear refractive index in a medium it propagates through [77]. The higher the intensity of a pulse component, the greater the frequency shift,  $\Psi(t)$ , it will undergo compared to weaker intensity components:

$$\phi(t) = \frac{n_2 I(t) \omega L}{c} \quad \text{Equation 2.30}$$

$$\Psi(t) = -\frac{d\phi(t)}{dt} = \frac{-\omega n_2 L}{c} \frac{dI(t)}{dt} \quad \text{Equation 2.31}$$

For a positive  $n_2$ , the leading edge of the pulse will be shifted to lower frequencies, while the trailing edge is shifted to higher frequencies. If SPM and negative GDD are balanced for a pulse, a temporal optical soliton can develop [77].

### 2.1.3. Modelocked Ti:sapphire lasers

Titanium-doped sapphire (Ti:Al<sub>2</sub>O<sub>3</sub>) is a solid state laser gain medium commonly used in ultrashort pulse generation. Ti<sup>3+</sup> ions are substituted for Al<sup>3+</sup> in the Al<sub>2</sub>O<sub>3</sub> sapphire crystal with typical doping concentrations of 0.1% wt. Ti:sapphire crystals have an energy transition that gives a broad absorption spectrum from approximately 400 nm to 650 nm and a very wide emission spectrum from around 660 nm up to 1100 nm [70].

Photons from the pump laser excite Ti<sup>3+</sup> ions from the <sup>2</sup>T<sub>2</sub> ground level to the <sup>2</sup>E excited state, where they relax to a lower sub-level of the laser upper level, before making a laser transition to a vibrationally excited sub-level of the ground level. They then relax further to the original ground state (see Figure 2.6). The electronic distribution between the two levels is very different and this, in addition to the strong interaction between the Ti<sup>3+</sup> ions and the sapphire crystal give the broad transition bandwidth [78].

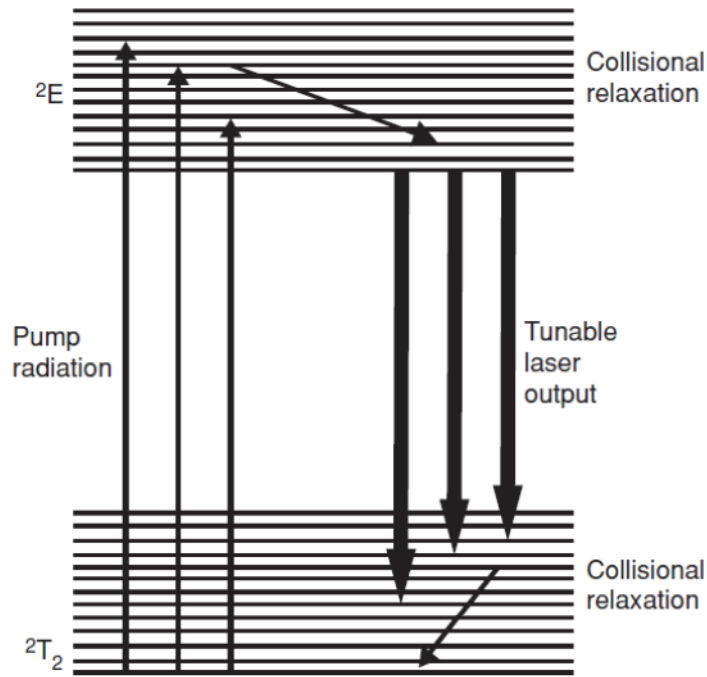


*Figure 2.6 The  $Ti^{3+}$  ions are excited to an upper sub-level of the upper laser level. They relax to a lower sub-level before making the laser transition to the upper ground state. Further relaxation takes them back to the original state. Figure taken from [79].*

Lasing from a Ti:sapphire laser was first demonstrated in 1982 [80], and they soon replaced dye lasers for many applications for modelocked near-IR sources. They are usually pumped using CW frequency-doubled Nd:YAG or Nd:YVO<sub>4</sub> lasers, although argon ion lasers are still occasionally used. The doped crystals are relatively easy to grow and can be as long as 30cm, although typically crystals of lengths less than 1 cm are used for both CW and modelocked operation [78].

Ti:sapphire crystals have many characteristics that are advantageous for ultrashort pulse modelocking including the broad tuning range mentioned above and a relatively large emission cross-section, comparable with Nd:YAG and greater than most ultrafast laser gain media. The  $Ti^{3+}$  ions also have an energy level structure that is unique amongst transition metal lasers as they have no d-state energy levels above the  $^2E$  laser level. This stops absorption of the laser light by excited state absorption, which reduced the tuning range and efficiency of other transition metal-doped gain media. These advantages are diminished however, by the short fluorescence lifetime of 3.2  $\mu s$ , which is significantly shorter than most ultrafast laser gain media [79].

One feature of Ti:sapphire-based lasers is that they can be modelocked using soft or hard aperture KLM [69, 76, 81]. By designing the cold cavity to have a negative

(anomalous) dispersion, the SPM that results from optical Kerr effect in the crystal and the GDD from the other optics can be balanced for ultrashort pulses. This causes soliton-like pulses to form.

For a true temporal soliton to form in a cavity, the second-order dispersion, GVD, and Kerr nonlinearity must be matched throughout the cavity. The soliton pulses will then propagate through any nonlinear medium with unchanging temporal or spectral shape and only an overall nonlinear phase shift. Solitons have the advantage of being very stable pulses and can recover from small disturbances to maintain their soliton characteristics. Where Kerr lens modelocking is used in Ti:sapphire lasers, stable modelocking is established at a pulse duration where SPM and GDD in the cavity are balanced. After many round-trips when this stability is reached, the pulses formed are soliton-like in their behaviour, so the modelocking is very stable and the pulses do not change over time [60]. However, these can only be described as soliton-like, as the SPM and GDD are only balanced across the whole cavity and are actually controlled using different discrete components. They would have to be balanced across the whole length of the cavity for true solitons to form.

#### ***2.1.4. Cavity design considerations***

The Ti:sapphire laser described in this thesis was used to pump a photonic crystal fibre (PCF) for spectral broadening to generate a supercontinuum, and to synchronously pump a femtosecond OPO. The cavity design also had to permit repetition frequency stabilisation for when the OPO frequency comb was locked.

Ti:sapphire lasers can be modelocked in linear standing wave or ring cavities. Ring cavities can provide some advantages over linear cavities for the type of laser that is needed to pump the OPO comb. When pumping a Ti:sapphire laser with several Watts of pump power, sometimes multi-pulsing can occur, which is easier to avoid with a ring laser configuration [69]. Another consideration for the Ti:sapphire laser is that it will need a relatively high power output to pump the OPO and a PCF. Although average output powers from ring lasers tend to be slightly lower than with linear cavities, the reduced sensitivity of ring lasers to back-reflections from optics usually dispenses with the need for an optical isolator [69]. By using a ring cavity the optical design can be slightly simplified without an overall reduction in the output power.



Early designs we used for the Ti:sapphire were for repetition frequencies up to 500 MHz. With the optomechanics available in the laser laboratory, this was more practical to build in a four mirror cavity in a bow-tie ring configuration than as a standing wave cavity. Even for the lower repetition frequency finally used at 280 MHz, this was easier to work with in a ring cavity configuration.

Ti:sapphire lasers have been modelocked in ring cavity configurations since the early 1990's [69]. Early designs showed they can be self-starting [69], generate ultrashort pulses [82], and have multiple GHz repetition frequencies [81]. Ring Ti:sapphire lasers are also suitable for use as stabilized optical frequency combs [83-85].

Initially a range of cavity designs, including both linear and ring configurations, were tried for a range of repetition frequencies from 200 - 500 MHz. These were pumped using a Coherent Verdi V10, which is a 10 W output power frequency-doubled diode-pumped solid-state single-longitudinal-mode CW laser at 532 nm, based on Nd:YVO<sub>4</sub>. When a new project in our research project started it then became necessary for us to change pump sources to a Spectra-Physics Millennia VIs J, which is a similar laser with a lower output power of 6 W and an output beam with multiple-longitudinal-modes. We then looked at moving to lower repetition frequency of between 250 and 300 MHz to ensure the output of the Ti:sapphire laser still had sufficient pulse energy for pumping the OPO.

The cavity was based on a 4.5 mm Ti:sapphire crystal mounted at Brewster angle to the pump beam from the Millennia laser. Using data from [72, 73], the refractive index, second order and third order dispersion for sapphire could be calculated using the material's Sellmeier equation. The results for this are shown in Figure 2.7, giving the GVD at 790 nm as 59.3 fs<sup>2</sup>/mm. A 4.5 mm Ti:sapphire crystal will therefore have a GDD of ~265 fs<sup>2</sup> when operating at close to 790 nm.

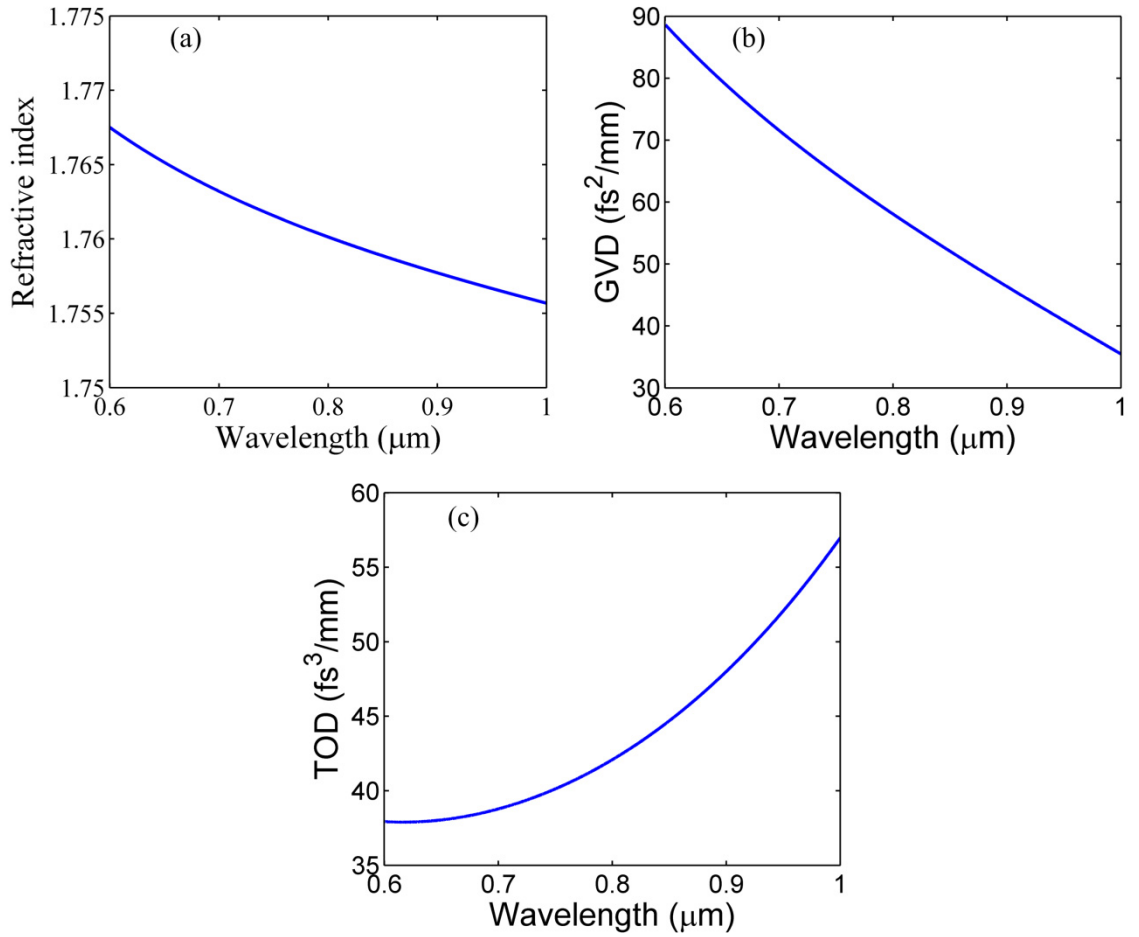


*Figure 2.7 Dispersion in a sapphire crystal using the Sellmeier equation [72, 73] used in Figure 2.4. (a) Graph showing refractive index vs. wavelength. (b) Graph showing second order dispersion, GVD, vs. wavelength. Data calculated from (a). (c) Graph showing third order dispersion (TOD) vs. wavelength. Data calculated from (b).*

The Ti:sapphire crystal was mounted at Brewster's angle in a 'home-built' brass mount. A small plate was screwed down on top of the crystal to hold it securely in place. The whole mount was water cooled using the same chiller unit used to cool the Millennia laser. The two main sections of the brass mount were held together using two screws which allowed for small changes in angle to ensure the crystal faces were at Brewster's angle to the laser beam. The entire brass mount was then screwed on to a micrometer translation stage so the distance between the crystal and the fixed curved mirror (M1) could be varied. The second curved mirror (M2) was also mounted on a micrometer translation stage to enable independent tuning of the distance between both the curved mirrors and the crystal (see Figure 2.8).

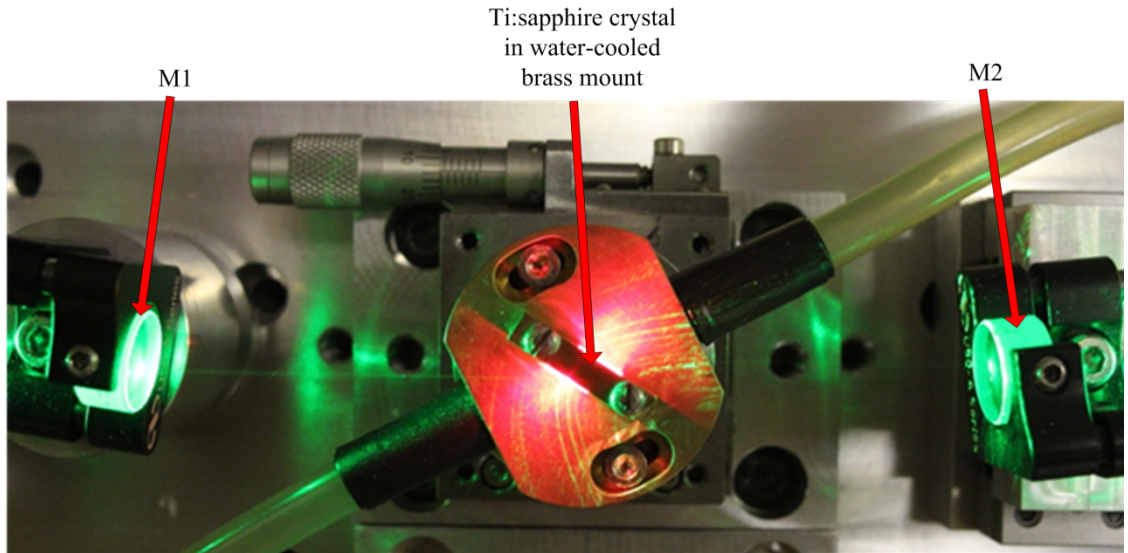


Figure 2.8 Photograph of the mounting for the Ti:sapphire crystal within the laser cavity. A brass crystal mount was used to hold the crystal and water chilled to minimise heat accumulation within the crystal. The crystal faces were at Brewster's angle to the beam and this could be adjusted using the screws visible in the brass mount. The mount was screwed onto a translation stage to allow movement in the z-direction.

To establish stable KLM the 'cold cavity' dispersion needs to be anomalous, or to have a negative GDD. A Gires-Tournois interferometer (GTI) mirror [86], with a GDD of  $-500 \text{ fs}^2$  at 800 nm was used to give the cavity a negative initial overall GDD [87-89]. Early cavity designs led to a ring cavity configuration with four mirrors in a crossed over 'x' shape. The output coupler (OC) and the two curved mirrors necessary to complete the cavity all had negligible dispersion at  $\sim 790 \text{ nm}$ , where the laser was expected to run. The basic cavity design is shown in Figure 2.9.

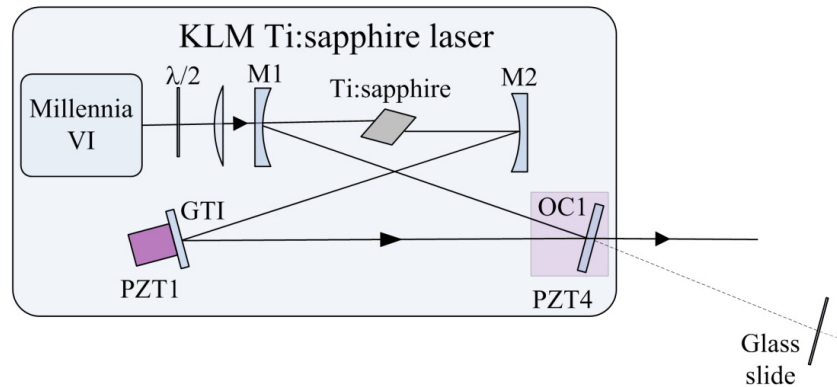


Figure 2.9 Schematic of the Ti:sapphire ring laser:  $\lambda/2$ , half-wave plate; M, dielectric mirror; GTI, Gires-Tournois interferometer; PZT, piezo-electric transducer or stack; OC, output coupler.

A glass microscope slide was used to reflect light back towards M1 when the laser was operating CW to ensure uni-directional operation. Placing this slide at a distance from the Ti:sapphire crystal that matched the path length from the OC to crystal did enable self-starting for modelocking with some of the early cavity designs, however these configurations did not lead to the most stable modelocking with high output powers and short pulse durations. The partial reflection from the glass slide was therefore blocked, with M2 being tapped, to establish modelocking.

Piezo-electric stack transducers (PZTs) were used control the length of the cavity. PZT1 was used to mount the GTI in a mirror mount and PZT4 was inserted in a micrometer translation stage upon which the OC mirror mount was fixed. These were used to lock the repetition frequency of the Ti:sapphire laser.

Once a repetition frequency had been selected ( $\sim 280$  MHz), a ring cavity was built based on the folding angles and optics used in previous designs. A selection of mirror curvatures and lenses, in addition to output couplers ranging from 2.5 – 20% were investigated to ensure optimum operating conditions. To find the optimum positions for the mirrors, as with earlier designs, ‘ABCD’ ray matrices for Gaussian beams were used in Matlab to give a good starting point with the optics and arm lengths used. A basic model was created using the separation of M1 and M2 from the Ti:sapphire crystal, and the distance between M1 and OC1 and from M2 to the GTI mirror, in order to find the edge of the stability region for the cavity [90-92]. All nonlinear effects were ignored and the Ti:sapphire was treated as a simple dielectric at a Brewster’s angle with a refractive index of 1.76 to find the eigenvalues for a range of folding angles and z-direction linear translations of the curved mirrors. These were then used to check whether the cavity was still a stable resonator for both the sagittal and tangential rays [93]. The starting point for investigating modelocking stability was selected from the graph with both curved mirrors 0.5 mm closer than their radius of curvature ( $D = -0.5$  mm) and half folding angles of  $8^\circ$  (see Figure 2.10).

The micrometer translation stages for the lens, Ti:sapphire crystal and M2 were then adjusted, with small changes in the turning angles at the curved mirrors, to find the optimum modelocking performance for the laser.

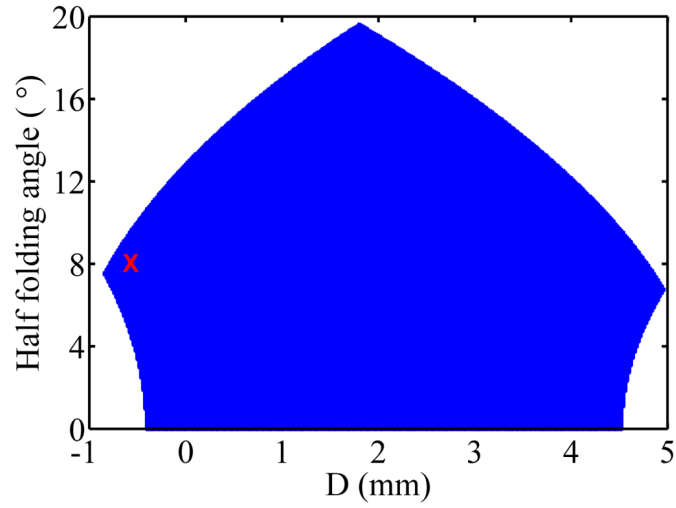


Figure 2.10 The stability region (blue) for the Ti:sapphire cavity. Stable Kerr lens modelocking is best at one edge of the stability region. Folding angles of  $8^\circ$  and mirror offset of  $-0.5$  mm ( $D$ ) from the length of their radius of curvature were chosen as a starting point for investigating modelocking (red 'X').

#### 2.1.5. Final cavity design

The final cavity configuration selected for modelocking at a repetition frequency just over 280 MHz. A half-wave plate turned the vertically-polarised Millennia beam to match the horizontal polarisation in the Ti:sapphire laser before the 89 mm lens. Two matching half-inch mirrors with  $R = -100$ mm focused the intracavity light in the Ti:sapphire crystal, with the GTI and output coupler completing the laser (see Figure 2.11).

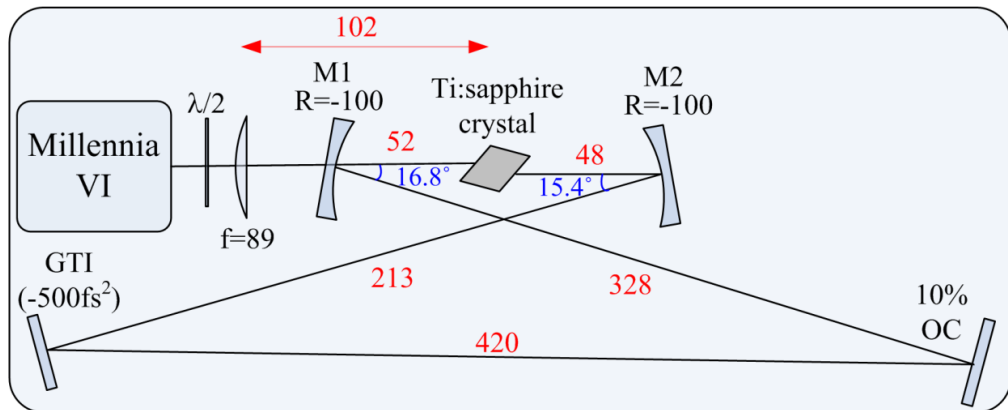
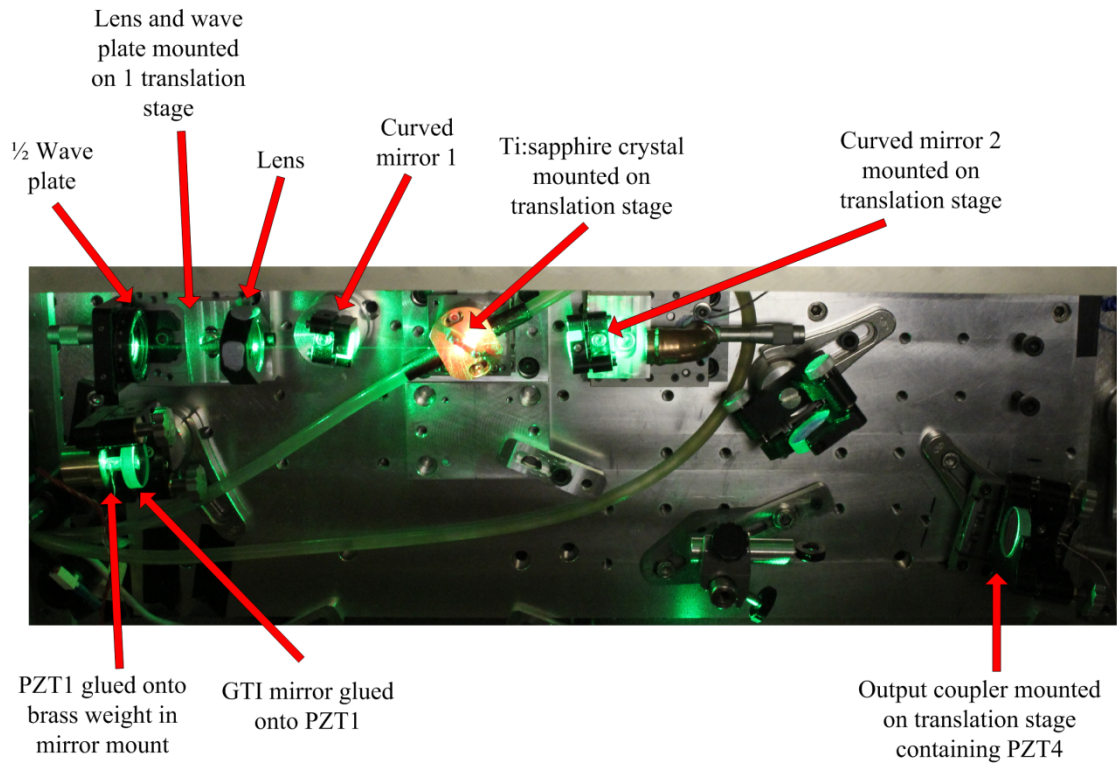


Figure 2.11 Schematic of the final Ti:sapphire ring laser. The folding angles and positions of elements on translation stages have been optimised to give stable modelocking with good average power output and short pulse durations ( $\sim 50$  fs). An output coupler with reflectivity  $R = 10\%$  was used. All lengths are in mm.

A labelled photograph in Figure 2.12 shows the complete laser. A partially reflecting mirror was used as a beamsplitter (BS1) after the output coupler and directed 75% of the output beam to where the OPO was located, with the remainder passing through the BS to be directed into the PCF for supercontinuum generation (see Figure 2.13).



*Figure 2.12 Photograph of the final Ti:sapphire cavity design. A cross-over bow-tie arrangement for 4 mirrors was used.*

Two irises were used in each of the two beams after the BS to maintain alignment into the OPO and PCF if small changes were made to the alignment in the Ti:sapphire laser. The irises in the beam to the OPO were closed until they were nearly clipping the beam when the Ti:sapphire laser was modelocked to minimise reflections from the OPO crystal so no optical isolator was needed. One of the optics used to reflect the Ti:sapphire beam into the OPO was a GTI (GDD of  $-500 \text{ fs}^2$  for normal incidence at 800 nm) to give the best performance from the OPO (see Figure 2.13). Details on this are given in Section 2.2.

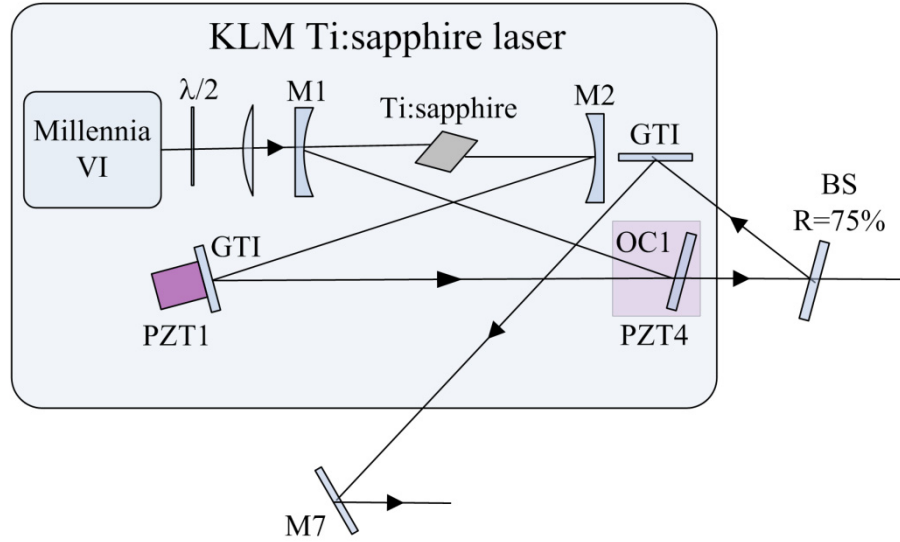
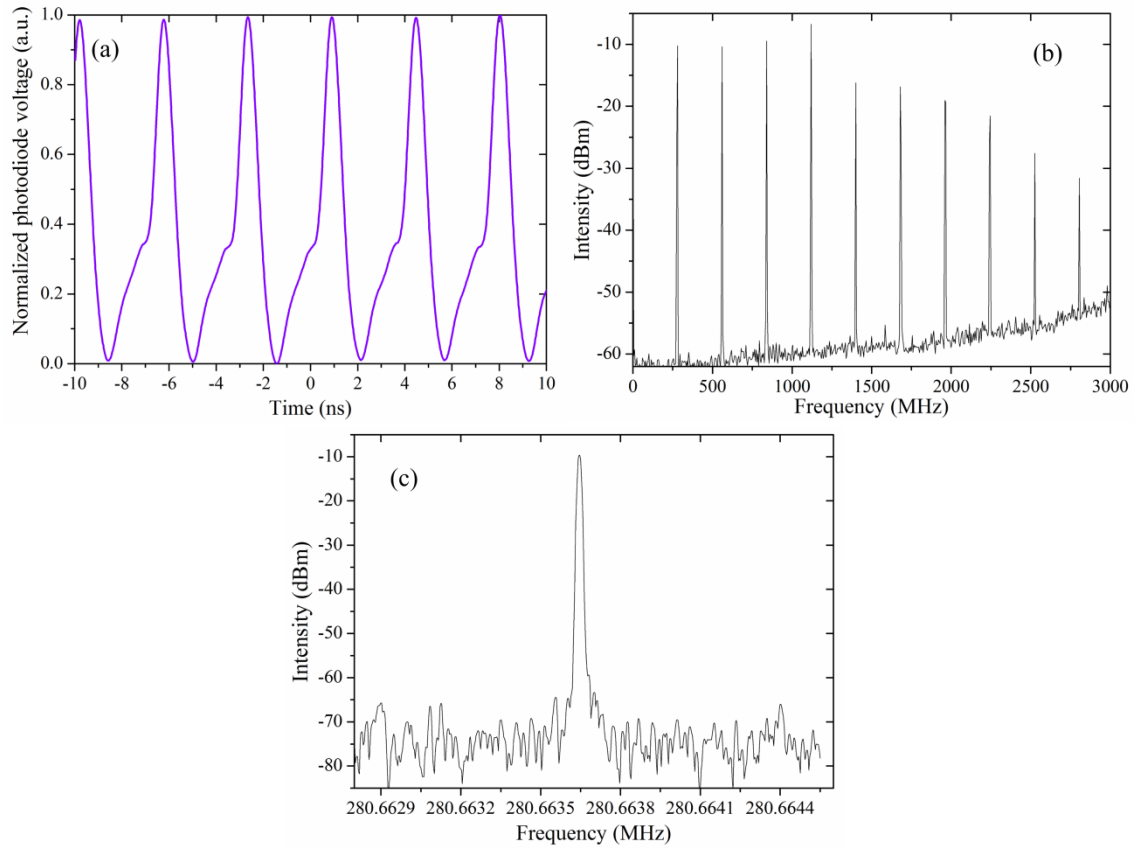


Figure 2.13 Schematic of the Ti:sapphire laser with additional external optics shown. A 75:25 partially reflecting mirror (BS) was used to allow some light to pass through for pumping a photonic crystal fibre, with the remainder of the light used to pump the optical parametric oscillator after M7.

#### 2.1.6. Characterisation of the Ti:sapphire laser

The output of the Ti:sapphire laser was centred at  $\sim 793$  nm. The average output power was over 1.4 W for modelocked operation. Time-domain and radio-frequency (RF) measurements were taken of the output pulse sequence to ensure stable single-pulse modelocking was achieved. The results recorded on an oscilloscope (Agilent Infiniium 54833A) and an RF spectrum analyser (Rigol DSA 1030A) are shown in Figure 2.14.

Figure 2.14(a) shows single-pulsing at a constant energy suggesting stable KLM. Figures 2.14(b) and (c) show modelocking in the frequency domain with clean harmonics up to the 10<sup>th</sup> harmonic of the fundamental frequency with narrow peaks and no sidebands.



*Figure 2.14 Repetition frequency of the Ti:sapphire laser at 280 MHz using a fast (2 GHz) Si photodiode. (a) Graph showing stable single pulse modelocking with very similar energy in each pulse. (b) Radio-frequency (RF) spectrum of the repetition frequency showing up to the 10<sup>th</sup> harmonic. (c) RF spectrum of the fundamental repetition frequency. Both Figures 2.14 (b) and (c) show no sidebands and clean narrow signal for the repetition frequency.*

The optical spectrum of the pulses was measured using an ANDO AQ6317B optical spectrum analyser (OSA) and gave a FWHM bandwidth of 18 nm centred at 793 nm, see Figure 2.15. CW sidebands above and below the modelocked spectrum contained little power (measured using dispersion through a prism) and so had no significant effect on the measurement for the output beam.



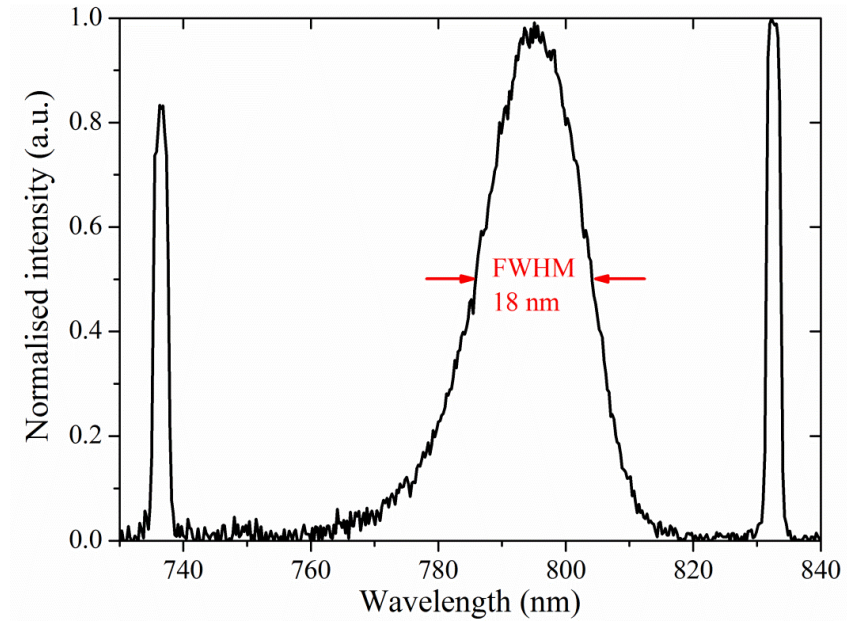


Figure 2.15 Optical spectrum of the Ti:sapphire laser measured with an OSA. The FWHM bandwidth is 18 nm (0.1 nm resolution).

The pulse duration of the laser was measured using a Timewarp E-750 autocorrelator (Figure 2.16) which led to a calculated pulse duration of  $\sim 48$  fs, which gives a time-bandwidth product of 2.59 (approximately  $1.3 \times$  bandwidth limited). This gives a peak power of  $\sim 100$  kW, which is sufficient power to pump the OPO and PCF.

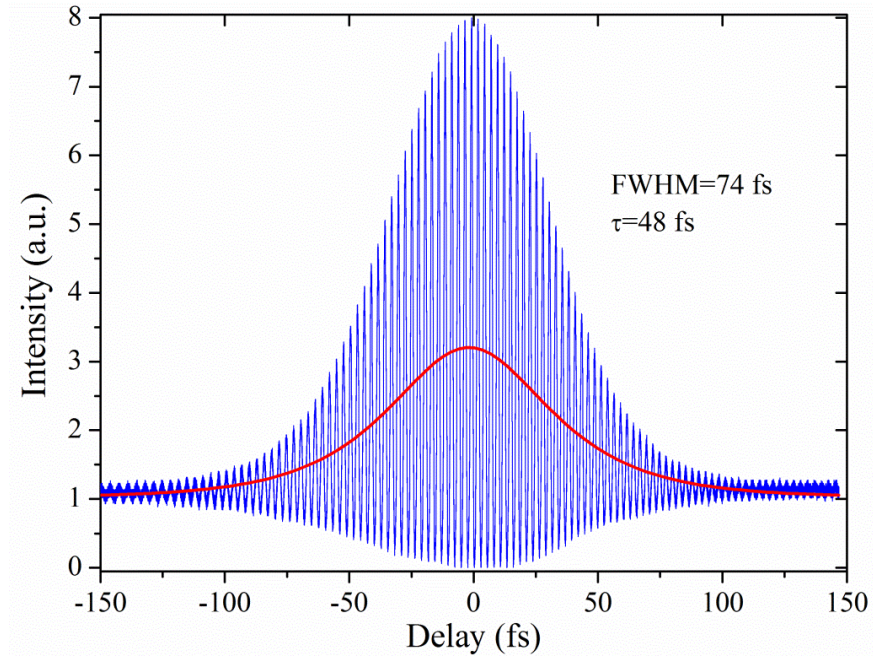


Figure 2.16 Autocorrelation of the Ti:sapphire laser measured using 2 photon absorption in a Timewarp (E-750) autocorrelator. The FWHM pulse duration was calculated as  $\sim 48$  fs.

The Ti:sapphire laser produces stable ultrashort pulses at a high repetition frequency. The centre frequency of the optical spectrum is suitable for use in an MgO:PPLN based OPO for the generation of pulses at 1500 nm. The cavity is designed to facilitate control of the repetition frequency for generating an OPO frequency comb.

## **2.2. Optical parametric oscillator**

This project aimed to develop a frequency comb source suitable for near-infrared (IR) spectroscopy measurements. The output of the modelocked Ti:sapphire laser was at too short a wavelength for most applications. OPOs utilise nonlinear processes, present in non-centrosymmetric optical media under intense irradiation, to generate new wavelengths. This project aimed to produce a frequency comb source for near-IR spectroscopy with gas cells such as acetylene (absorption at  $\sim 1520$  and  $1530$  nm), with a long term aim of moving to the mid-IR region of the spectrum.

OPOs work by nonlinear interactions inside crystals. Light propagating through a medium interacts with the electric dipoles formed by the nuclei and surrounding electrons. These dipoles then oscillate and so act as sources of photons in turn. For high intensities, the relationship between irradiance and amplitude of oscillation can not be approximated as linear and photons are emitted at frequencies differing from the incident light. These nonlinear optical effects can initiate frequency doubling, sum or difference frequency generation and parametric amplification [94]. An optical cavity can be built around a medium where optical parametric amplification can be achieved to form an OPO.

An OPO was built to generate light at close to 1500 nm from the 800 nm light emitted from the laser. This was done using a similar cavity design to the laser, with PZT's included to ultimately allow for locking the CEO-frequency of the signal pulses so a stabilised frequency comb could be realised.

### **2.2.1. Introduction to second-order nonlinear optics**

In Section 2.1.2 we showed that the polarisation is no longer linear for high intensity pulses (Equation 2.17). Previously we assumed the material to have inversion symmetry and therefore zero  $\chi^{(2)}$ , but some materials, such as nonlinear crystals in OPOs, do not have inversion symmetry, so this term must be considered. If we again

assume polarisation and the electric field to be scalar, then where third-order and higher terms are ignored the polarisation can be expressed as:

$$P = \varepsilon_0(\chi^{(1)}E + \chi^{(2)}E^2) \quad \text{Equation 2.32}$$

where  $\chi^{(1)}$  is the linear susceptibility and  $\chi^{(2)}$  is the second order nonlinear susceptibility [75].

For second order nonlinear effects momentum and total photon energy are conserved and the exchange of energy between the waves that will be involved is coupled by the second order nonlinear susceptibility.

With sum or difference frequency mixing, two incident waves,  $\omega_1$  and  $\omega_2$ , with similar intensities and frequencies, cause the emission of a third wave,  $\omega_3$ , such that:

$$P(\omega_3) = \varepsilon_0\chi^{(2)}E(\omega_1)E(\omega_2) \quad \text{Equation 2.33}$$

for  $\omega_3 = \omega_1 + \omega_2$  in the case of sum frequency mixing, SFM [75].

If the incident waves have a common frequency,  $\omega_1$ , then the frequency generated will become  $\omega_3 = 2\omega_1$ . In this case, for an incident wave with electric field  $E = \epsilon \sin(\omega_1 t)$ , the induced polarisation can be expressed as:

$$\begin{aligned} P(\omega_3) &= \varepsilon_0[\chi^{(1)} \epsilon \sin(\omega_1 t) + \chi^{(2)} \epsilon^2 \sin^2(\omega_1 t) + \dots] \\ &= \varepsilon_0\left[\chi^{(1)} \epsilon \sin(\omega_1 t) + \frac{1}{2}\chi^{(2)} \epsilon^2 (1 - \cos 2\omega_1 t) + \dots\right] \end{aligned} \quad \text{Equation 2.34}$$

So a wave with double the original frequency can be radiated, this is second harmonic generation, SHG [75]. Very large electric fields are required for significant amounts of SHG, which is why lasers are normally required to reach the required intensities.

We have seen that two waves can create a wave with a frequency equal to the sum of their frequencies, but two waves can also create a wave with their difference frequency. If there is one input ‘pump’ wave that causes noise to be emitted at a lower frequency, the signal, then to conserve energy an additional output will be generated, which is known as the idler. As the signal and idler grow, then parametric amplification can be achieved. Energy and momentum conservation required in this process means that:

$$\omega_p = \omega_s + \omega_i \quad \text{Equation 2.35}$$

$$k_p = k_s + k_i \quad \text{Equation 2.36}$$

So the sum of the frequencies of the signal and idler waves must equal the frequency of the pump wave, and the sum of the wavevectors of the sum and idler waves must be equal to the wavevector of the pump wave.

### 2.2.2. *Nonlinear optics in optical parametric oscillators*

Parasitic SFM and SHG processes are typically observed in an OPO, in addition to optical parametric oscillation, although higher-order nonlinear processes may also be present.

#### Sum frequency mixing

Here we consider SFM from two collimated, monochromatic CW lasers, with electric fields  $E_1$  and  $E_2$ , at normal incidence to a lossless nonlinear optical medium. These can be expressed as:

$$E_1(z, t) = A_1 \exp(k_1 z - \omega_1 t) + c. c. \quad \text{Equation 2.37}$$

$$E_2(z, t) = A_2 \exp(k_2 z - \omega_2 t) + c. c. \quad \text{Equation 2.38}$$

Where  $A_i$  is the amplitude,  $k_i$  the wavevector,  $\omega_i$  is the angular frequency of electric field  $E_i$  propagating in the z-axis and  $c.c.$  is the complex conjugate [95].

The sum frequency component will have an electric field,  $E_3$ , such that:

$$E_3(z, t) = A_3 \exp(k_3 z - \omega_3 t) + c. c. \quad \text{Equation 2.39}$$

Assuming a fixed geometry, the nonlinear polarisation for SFM can be expressed as:

$$P(\omega_3) = 4d_{eff}E(\omega_1)E(\omega_2) = 4d_{eff}A_1A_2 \exp(i[k_1 + k_2]z) \quad \text{Equation 2.40}$$

where we have defined  $d_{eff}$ , as a new scalar nonlinear susceptibility.

We can use the 1-D wave equation for a wave propagating in z:

$$\frac{d^2 E(z, t)}{dz^2} - \frac{1}{c^2} \frac{d^2 E(z, t)}{dt^2} = \frac{4\pi}{c^2} \frac{d^2 P(z, t)}{dt^2} \quad \text{Equation 2.41}$$

Substituting Equations 2.39 and 2.40 into Equation 2.41 will give:

$$\begin{aligned} & \left[ \frac{d^2 A_3}{dz^2} + 2ik_3 \frac{dA_3}{dz} - k_3^2 A_3 + \frac{n^2 \omega_3^2 A_3}{c^2} \right] \exp(i[k_3 z - \omega_3 t]) + c. c. \\ & = \frac{-16\pi d_{eff} \omega_3^2}{c^2} A_1 A_2 \exp(i[k_1 + k_2]z - \omega_3 t) + c. c. \end{aligned} \quad \text{Equation 2.42}$$

$$\frac{d^2 A_3}{dz^2} + 2ik_3 \frac{dA_3}{dz} = \frac{-16\pi d_{eff}\omega_3^2}{c^2} A_1 A_2 \exp(i[k_1 + k_2 - k_3]z) \quad \text{Equation 2.43}$$

The first term in Equation 2.43 is much smaller than the second term, so we can use the slowly-varying amplitude approximation, i.e. the change in  $A_3$  over the distance of an optical wavelength is less than unity [95]. This simplifies Equation 2.43 to give:

$$\frac{dA_3}{dz} = \frac{8\pi d_{eff}\omega_3^2}{k_3 c^2} A_1 A_2 e^{i\Delta k z} \quad \text{Equation 2.44}$$

Equations for input waves  $\omega_1$  and  $\omega_2$  can be derived using the same principles:

$$\frac{dA_1}{dz} = \frac{8\pi d_{eff}\omega_1^2}{k_1 c^2} A_3 A_2^* e^{i\Delta k z} \quad \text{Equation 2.45}$$

$$\frac{dA_2}{dz} = \frac{8\pi d_{eff}\omega_2^2}{k_2 c^2} A_3 A_1^* e^{i\Delta k z} \quad \text{Equation 2.46}$$

where

$$\Delta k = k_3 - k_2 - k_1 \quad \text{Equation 2.47}$$

For efficient SFM in a crystal, the wavevector mismatch,  $\Delta k$ , must be considered. Making the assumption SFM is relatively small and  $A_1$  and  $A_2$  are constant, then for  $\Delta k = 0$ , the amplitude  $A_3$  will increase linearly with  $z$  and its intensity will increase quadratically. This is perfect phase matching and the wave at  $\omega_3$  will have a fixed phase relationship with the nonlinear polarisation and so SFM will be at its most efficient with all the waves generated adding coherently [95]. The efficiency of SFM will decrease with increasing wavevector mismatch. For a distance  $L$  into a nonlinear crystal, the efficiency of conversion from  $\omega_1$  and  $\omega_2$  to  $\omega_3$  will decrease with  $L$ , until  $L$  exceeds  $\pi/\Delta k$ , where the direction of conversion will swap back to towards  $\omega_1$  and  $\omega_2$ . The period for growth or decay in SFM is  $\Delta k L = \pi$ . The coherence length,  $L_c$ , of a medium is therefore defined as:

$$L_c = \pi/\Delta k \quad \text{Equation 2.48}$$

### Second harmonic generation

For second harmonic generation in a nonlinear medium where  $\omega_3 = 2\omega_1$ , the coupled wave equations are of the same form as with SFM, so:

$$\frac{dA_1}{dz} = \frac{8\pi d_{eff}\omega_1^2}{k_1 c^2} A_3 A_1^* e^{i\Delta k z} \quad \text{Equation 2.49}$$

$$\frac{dA_3}{dz} = \frac{4\pi i d_{eff} \omega_3^2}{k_3 c^2} A_1^2 e^{i\Delta k z} \quad \text{Equation 2.50}$$

where

$$\Delta k = k_3 - 2k_1 \quad \text{Equation 2.51}$$

assuming an undepleted pump [95].

### Difference frequency mixing and optical parametric amplification

With difference frequency mixing (DFM) a nonlinear interaction between two waves,  $\omega_3$  and  $\omega_1$ , generates a new wave  $\omega_2$ . So  $\omega_2 = \omega_3 - \omega_1$ . If once again we treat the interaction as lossless and assume  $\omega_3$  remains undepleted, we can again derive coupled wave equations for the interaction:

$$\frac{dA_1}{dz} = \frac{8\pi i d_{eff} \omega_1^2}{k_1 c^2} A_3 A_2^* e^{i\Delta k z} \quad \text{Equation 2.52}$$

$$\frac{dA_2}{dz} = \frac{8\pi i d_{eff} \omega_2^2}{k_2 c^2} A_3 A_1^* e^{i\Delta k z} \quad \text{Equation 2.53}$$

$$\frac{dA_3}{dz} = \frac{8\pi i d_{eff} \omega_3^2}{k_3 c^2} A_1 A_2 e^{-i\Delta k z} \quad \text{Equation 2.54}$$

where

$$\Delta k = k_3 - k_1 - k_2 \quad \text{Equation 2.55}$$

The generated wave  $\omega_1$  will maintain its phase and undergo amplification, whereas wave  $\omega_2$  will have a phase dependence on both the pump and  $\omega_1$  in addition to experiencing growth. The generation of each of the fields for  $\omega_1$  and  $\omega_2$  stimulates the growth of the other field, so both will experience exponential growth [95].

The amplification of the field for  $\omega_1$  by difference frequency mixing means this process is also described as parametric amplification and is used in optical parametric amplifiers (OPAs). The wave at  $\omega_1$  is amplified by the nonlinear process and is known as the signal wave ( $\omega_s$ ), and the wave at  $\omega_2$  is generated as a result of this process and is referred to as the idler wave ( $\omega_i$ ). An OPA for  $\omega_s$  and/or  $\omega_i$  can be placed inside an optical resonator cavity to form an optical parametric oscillator, or OPO [95].

The end mirrors in an OPO can be highly reflective for the signal, idler, or both the signal and idler frequencies. In the latter case, this is a doubly-resonant OPO (see

Figure 2.17). OPOs that operate at or close to degeneracy (where  $\omega_s = \omega_i$ ) are normally doubly-resonant. Doubly-resonant OPOs have lower thresholds than singly-resonant, however they also have lower power stability and don't allow for smooth wavelength tuning and so are not usually desirable. As long as  $\omega_s < \omega_p$ , in theory any signal frequency that falls within the crystal gain spectrum can be generated in an OPO, however practically the wavelength of the signal wave is controlled by the phase matching condition and dispersion in the OPO cavity [95].

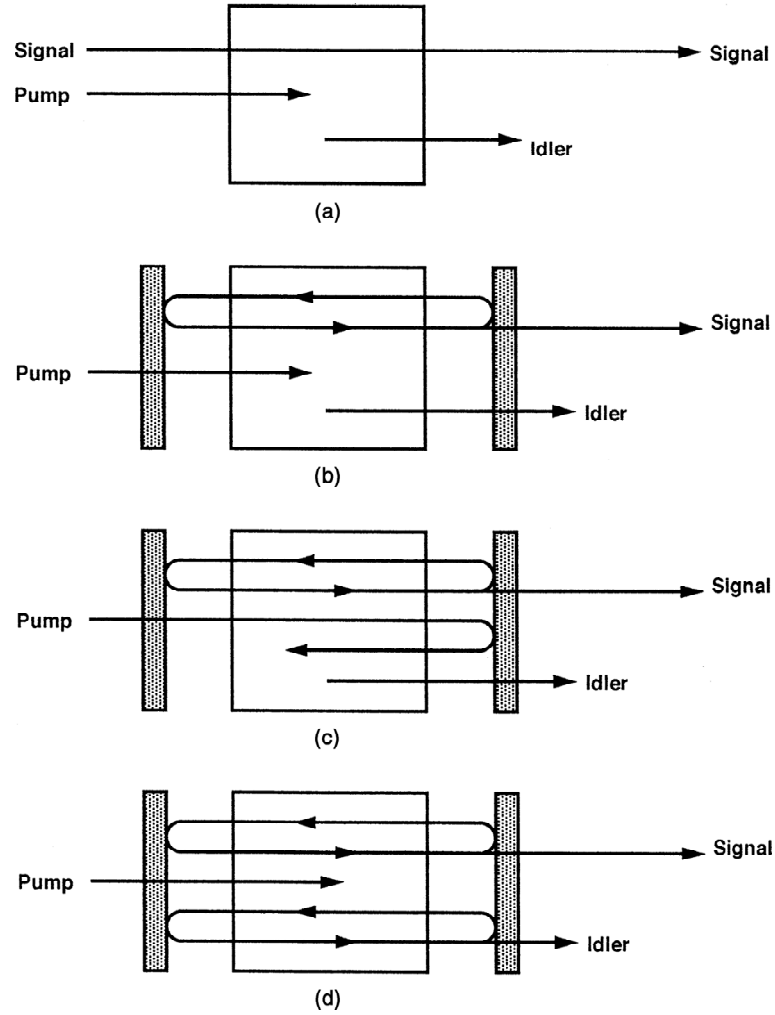


Figure 2.17 Configurations for OPAs and OPOs. (a) An optical parametric amplifier, OPA. (b) A singly-resonant optical parametric oscillator, OPO. (c) A singly-resonant OPO where a mirror is also HR for the pump beam. (d) A doubly-resonant OPO. Images taken from [75].

Nonlinear processes present in OPOs such as SFM and parametric amplification need the phase matching condition,  $\Delta k = 0$ , to be satisfied, that for efficient generation to take place. When depletion of the input beam is also considered this condition must still be

satisfied for efficient frequency generation. Materials used for nonlinear processes tend to cause normal dispersion in the visible/near-IR, so in the case  $\omega_3 = \omega_1 + \omega_2$ , the condition takes the form:  $n_3\omega_3 = n_1\omega_1 + n_2\omega_2$ , which cannot be achieved directly. The phase matching condition can still be satisfied if the birefringent characteristics of many nonlinear crystals are exploited. The angular orientation of the crystal to the incident light, or the temperature of the crystal can be used to control the birefringent effects [95].

Where a second-order nonlinear optical medium is used which has weak or no birefringent properties, or it is not practical to use this property to control phase matching, quasi-phase matching will be used. Rather than use a single crystal as the optical medium, it can be divided into effectively many single-domain sub-crystals, which are stacked on top of each other with the domain orientation of neighbouring sub-crystals rotated by  $180^\circ$  relative to each other. The periodicity of this structure,  $\Lambda$ , or the distance separating two regions with equal orientations, is defined as [95]:

$$\Lambda = L_c \quad \text{Equation 2.56}$$

where  $L_c$  was defined in Equation 2.48.

One example of quasi-phase matching in a crystal is periodically poled lithium niobate ( $\text{LiNbO}_3$ ), or PPLN. As with single-domain lithium niobate, this has a low photorefractive damage threshold and requires heating to reduce photorefractive damage from short wavelength radiation generated by SFM and SHG [96]. It also has a high nonlinear coefficient and so is commonly used in low peak power pulsed and CW OPOs [75].

### ***2.2.3. Introduction to synchronously pumped femtosecond optical parametric oscillators***

OPOs were first demonstrated back in the 1960's [97, 98]. Synchronously pumped OPOs have optical path lengths that match or are an exact ratio of the laser cavity. Synchronously pumping an ultrafast OPO with a femtosecond laser [45] can enable smooth wavelength tuning as there is no gain storage in the OPO crystal, so the signal pulse must pass through the nonlinear crystal at the same time as an incoming pump pulse to experience gain. OPO crystals typically have large gain bandwidths, so changes in the cavity length can be compensated for by changes in the generated frequencies in order to maintain synchronism [24, 25]. As the cavity length is tuned,



the signal wavelength shifts, changing the group velocity to maintain a constant round trip time through dispersion compensation in the nonlinear crystal [25]. The same effect will also affect the optical and temporal bandwidths of the pulses. For very small changes in the cavity length, the signal wavelength will stay approximately constant, while the carrier-envelope-phase slip of the pulses will be tuned [29]. Ring OPOs have only a single pass of the nonlinear crystal and are less sensitive to changes in cavity alignment and length. This can make them more stable for low noise applications such as frequency comb sources. Synchronous pumping at high repetition frequencies has been successfully demonstrated in femtosecond ring OPOs pumped by Ti:sapphire lasers [99-103]. The stability of ring OPOs has also been demonstrated in OPO frequency combs synchronously pumped by Ti:sapphire and chromium-doped zinc selenide ( $\text{Cr}^{2+}:\text{ZnSe}$ ) lasers [37, 47].

#### **2.2.4. Cavity design and construction**

The OPO was synchronously pumped by the KLM Ti:sapphire laser detailed in Section 2.1 and was chosen to be a ring cavity based on MgO-doped PPLN. Quasi-phase matching (QPM) was used to maximise down-conversion across the full length of the crystal. Doping the PPLN with magnesium oxide increases the pump power that can be applied without it experiencing photorefractive damage in the crystal [75]. The signal and idler wavelengths generated in an OPO based on PPLN are dependent on the temperature of the crystal for a fixed grating period,  $\Lambda$ , see Figure 2.18. The refractive index of the crystal is temperature dependent, so heating the crystal will change the wavevector mismatch (from Equations 2.11 and 2.38) and therefore the quasi-phase matching condition, shifting the optical frequencies of the signal and idler. Heating the crystal raises its photorefractive damage threshold and so the MgO:PPLN was heated to 90° C [75, 96]; however the accompanying QPM tuning necessitates the use of a shorter grating period to generate signal pulses at 1500 nm. Figure 2.18 presents the phasematching for an MgO:PPLN crystal based on data used by Gayer *et al.* in an OPO [104, 105]. In this example when the crystal was heated to 90° C a grating period of ~20  $\mu\text{m}$  would be needed to generate signal pulses at 1500 nm.

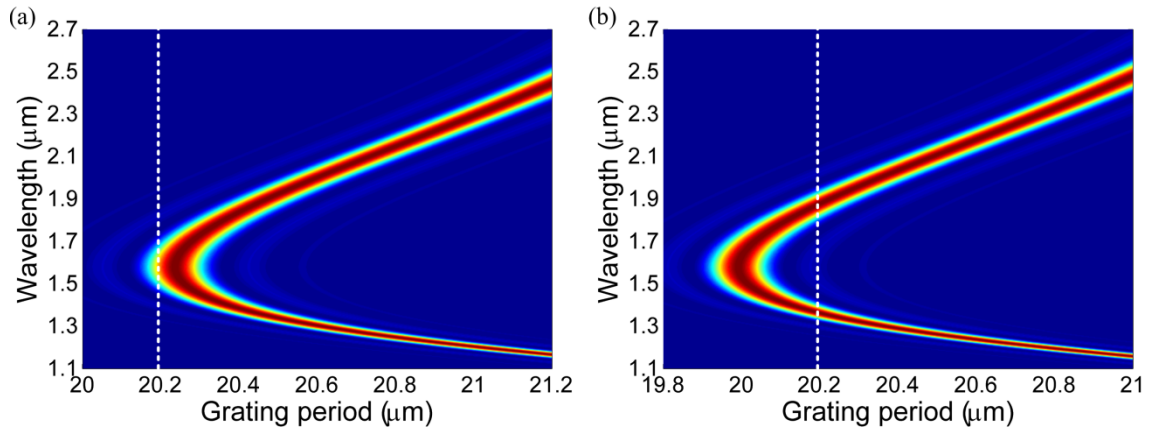


Figure 2.18 Phase-matching for a piece of PPLN based on data from [104, 105]. (a) Crystal at 20 °C. (b) Crystal heated to 90° C. Dotted line shows wavelengths phase matched for a 20.2  $\mu\text{m}$  grating period.

The OPO ring cavity design was based on the four-mirror cavity design for the Ti:sapphire laser. Synchronously pumping away from degeneracy (so  $\omega_s \neq \omega_i$ ) makes it possible to tune the wavelength (and carrier-envelope-phase slip) of the signal pulses by tuning the OPO cavity length.

The crystal used in the OPO was previously used for a different experiment and so was AR coated for  $\sim 1300$  nm rather than at 1500 nm where the OPO was to operate. This was expected to reduce the efficiency of the system. The MgO:PPLN crystal (HC Photonics) was 1 mm thick with grating periods ranging from 20.4 – 21.6  $\mu\text{m}$  (in steps of 0.2  $\mu\text{m}$ ) along its length (from top to bottom in Figure 2.19). The highest power at 1500 nm was obtained from the system when using the 20.4  $\mu\text{m}$  grating period. This differs significantly from the example presented in Figure 2.18, which may be in part due to differences between the crystal growth techniques.

The crystal was mounted in a custom designed aluminium holder with a brass adapter to mount it in a mirror mount. A resistor (blue cables) was used to heat the holder to 90° C, driven by the TEC (thermoelectric cooler) on an ILX Lightwave LDC-3722B Laser Diode Controller. A thermistor (yellow cable) was used as feedback to the TEC controller, see Figure 2.19. The thermistor monitored the temperature of the crystal mount, rather than the actual crystal, which may also account for some of the difference between the performance of this OPO and the data presented in Figure 2.18.

The mirror mount provided horizontal and vertical tilt, which were used to direct back-reflections from the crystal face so they were sufficiently clipped by the two irises

between the laser and the OPO to remove the need for an optical isolator. Reflections off the back face of the crystal propagated in the opposite direction to the main beam in the OPO and formed a second, much lower power, output beam at an angle to the main OPO output. An x-y-z translation stage holding the mirror mount enabled easy alignment of the laser beam through the centre of a grating, moving from one grating period to the next without changing the optical alignment, and optimisation of the focusing in the crystal (see Figure 2.20).

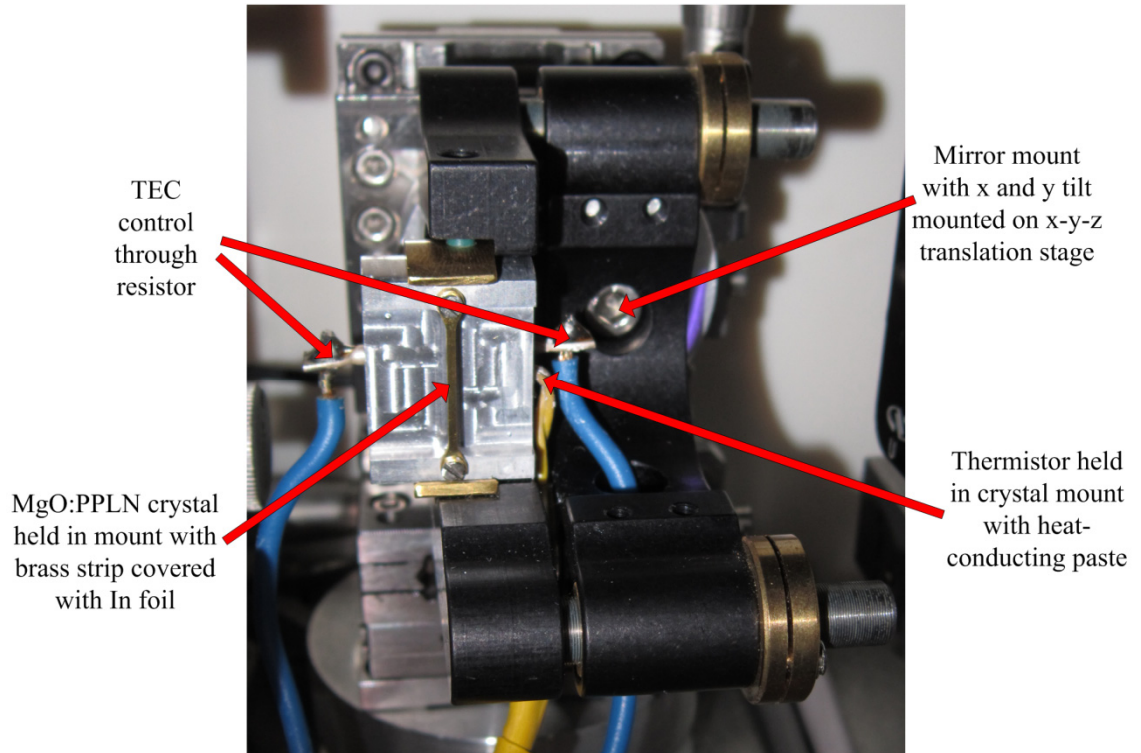


*Figure 2.19 Photograph showing the mounting of the PPLN crystal within the OPO cavity. An aluminium crystal mount was used to hold the PPLN crystal and heated to 90° C using a resistor thermally contacted to the brass holder (current supplied by blue-clad wires). A thermistor (yellow clad) was used to monitor the crystal oven. Heating the crystal minimised the risk of damage (photorefractive effects) when the system was running [75, 96].*

The GTI mirror used to add negative chirp to the pump pulses had a GDD of  $-500 \text{ fs}^2$  at 0°, or normal to the mirror surface. As it was used at close to 45°, the effective GDD will have differed from this. The output power from the OPO was compared for using none, one and two of these GTIs between the Ti:sapphire laser and OPO, switching between GTIs and HR mirrors accordingly. Using one GTI and one HR mirror was

found to give enough negative chirp on the pulses for efficient down conversion inside the crystal (see Figure 2.20). This was investigated along with testing a GTI in the cavity in place of mirror M5 and using prisms in the OPO cavity to determine performance for positive or negative GDD in the cavity. For some cavity configurations the pump power was only just above threshold, and so having only the three HR mirrors with an output coupler in the cavity helped to minimise any losses and gave an overall positive (normal) dispersion.

The plane mirror (M5) was mounted on a PZT (PZT2) in preparation for when the carrier-envelope-offset (CEO) frequency of OPO was locked. A second PZT (PZT3) was mounted inside a micrometer translation stage for larger changes in cavity length for manual CEO-frequency and wavelength tuning.

Originally, cavity lengths for repetition frequencies between 200 and 500 MHz were investigated. Ratios between the Ti:sapphire laser and the OPO were tested to generate higher repetition frequencies for the output of the OPO resulting from differences between the two cavity lengths [102, 106]. But, once the pump for the Ti:sapphire laser was changed from a 10 W Verdi laser to a 6 W Millennia laser, the output power from the Ti:sapphire laser was no longer high enough to use these options and so an OPO with a cavity length matched to the laser was used. Rather than aiming for a higher repetition frequency as a result of the difference between the two cavity lengths, we planned instead to use an additional external cavity later in the system to filter the frequency comb and raise the mode separation [56]. This work will be detailed in Chapter 5.

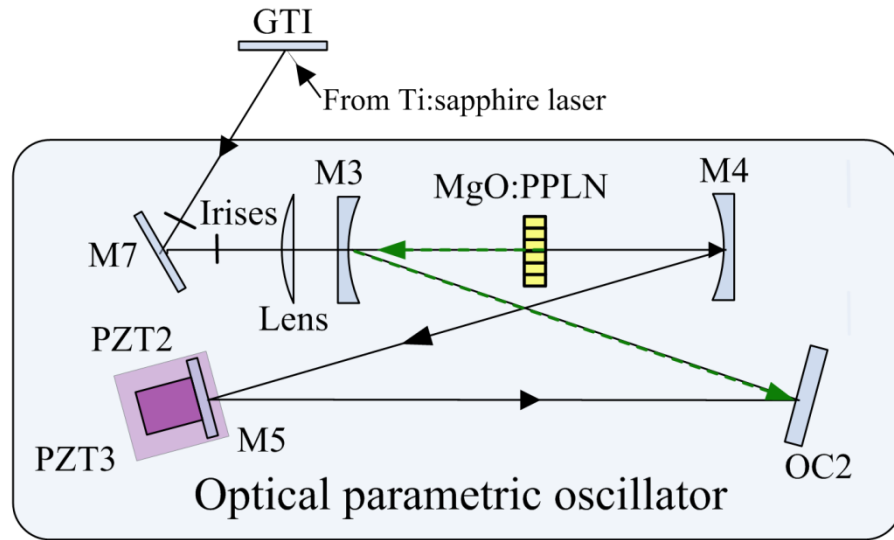


Figure 2.20 Schematic of the OPO cavity design: *M*, dielectric mirror; *PZT*, piezo-electric transducer or stack; *OC*, output coupler ( $R = 10\%$ ). The green dashed line shows where some light is reflected back from the crystal to output at an angle to the main output beam (solid black line).

For the best optical configuration, as with any earlier OPO designs, ‘ABCD’ ray matrices for Gaussian beams were used in Matlab to give a good starting point with the optics and arm lengths used. As with the Ti:sapphire laser in Section 2.1.4, the model was made using the distances between the curved mirrors and both the PPLN crystal and the closest plane mirror to find the edge of the stability region for the cavity [90–92]. In this case the model was simpler as no astigmatism from the crystal was considered as it was not mounted at the Brewster’s angle. All nonlinear effects were ignored and the PPLN was treated as a simple dielectric at close to normal to the pump beam with a refractive index of  $\sim 2.13$  to find the eigenvalues for a range of folding angles and  $z$ -direction linear translations of the curved mirrors. These were then used to check whether the cavity was still a stable resonator. The starting point for investigating modelocking stability was with the two curved mirrors separated by their radius of curvature ( $D = 0$ ) and half folding angles of  $3.5^\circ$  (see Figures 2.20 and 2.21). This angle was chosen to minimise astigmatism from the curved mirrors without the beam being clipped by any of the optics or mounts.

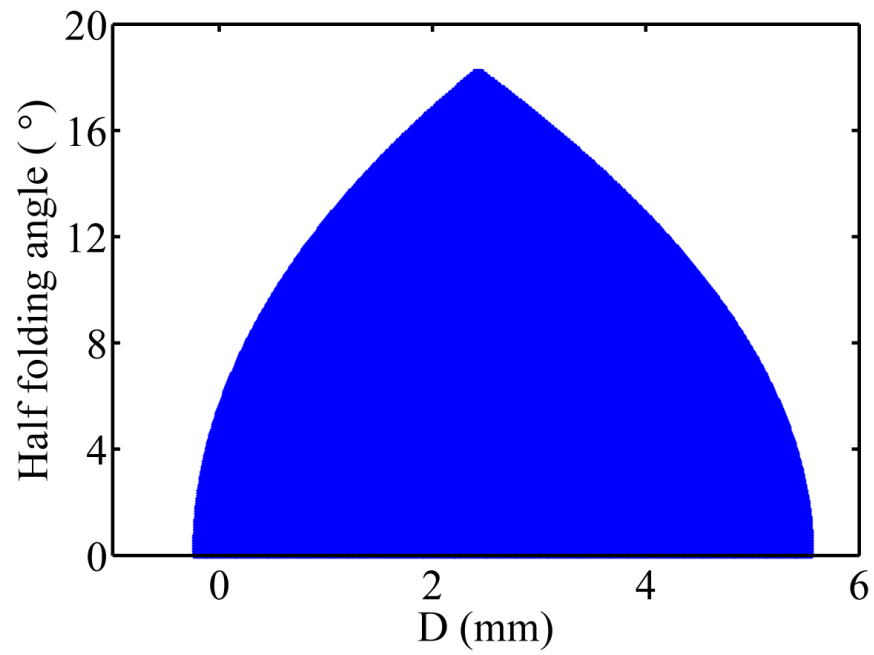


Figure 2.21 Graph drawn in Matlab to show the stability region (blue) for the OPO cavity. Folding angles of  $7^\circ$  and mirror offset of 0 mm (D) from the length of their radius of curvature were chosen as a starting point for investigating oscillation.

From the initial starting position detailed above, the micrometer translation stages for the lens, PPLN crystal and M4 were optimised for maximum output power at 1500 nm (see Figure 2.23). The angular alignment of the four mirrors was also optimised for the final configuration (see Figure 2.22).

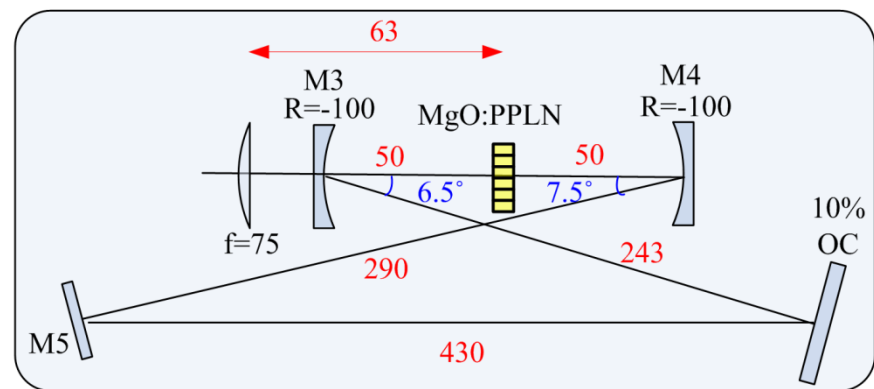
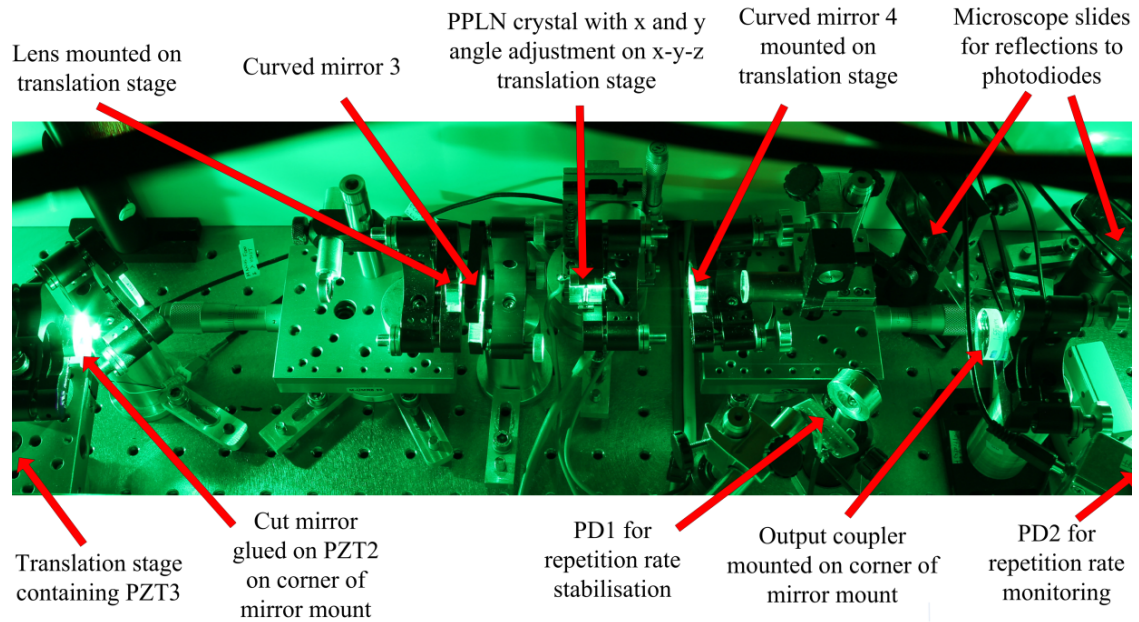


Figure 2.22 Schematic of the final OPO cavity. The folding angles and positions of elements on translation stages were optimised to ensure the OPO operates stably with good average power output and wavelength tunability. All lengths are in mm.

The final cavity configuration is shown in Figures 2.22 and 2.23. Output couplers with 2.5%, 6% and 10% transmission were investigated for the maximum output power, with 10% selected. The coating on the 6% output coupler was of relatively poor quality and this may have been the reason for obtaining better results with the 10%, which is not what we had expected, so the output coupling was relatively high for the system. Two fast photodiodes (PD) were used to monitor the repetition frequency from the depleted pump.



*Figure 2.23 Photograph of the final OPO cavity design. A cross-over bow-tie arrangement for 4 mirrors was used, based on the design for the Ti:sapphire laser.*

The photograph in Figure 2.23 shows a green light illuminating the OPO cavity. The main (non-phase matched) outputs observed from the OPO, in addition to the pump, signal and idler, were: SFM of the pump and signal pulses; SFM of the pump and idler pulses, and SHG for the pump pulses. The SFM of the pump and signal (at 519 nm) is causing the green illumination in the photograph. The wavelengths generated from interactions in the OPO are presented in Table 2.1.

Origin	pump	signal	idler	pump SHG	pump + signal SFM	pump + idler SFM
Wavelength (nm)	794	1500	1685	397	519	540

*Table 2.1 Wavelengths for the required OPO pump, signal and idler pulses, in addition to the other significant pulses generated.*



Figure 2.24 shows the complete layout of the synchronously pumped OPO. The main output of the OPO (shown as dark red) was used for further experiments once the laser and OPO cavities were stabilised to form a frequency comb. Some of the pump beam (the Ti:sapphire laser output) leaked through the second curved mirror (M4) and was detected on a fast Si photodiode (PD1) for monitoring the repetition frequency, which is always identical for the laser and OPO whilst both are running. There was also a small reflection off the back face of the PPLN crystal which contained some of the generated frequencies, including a strong component of the SFM of the pump and signal pulses. This was used for locking the CEO-frequency of the OPO signal pulses, as detailed in Chapter 3.

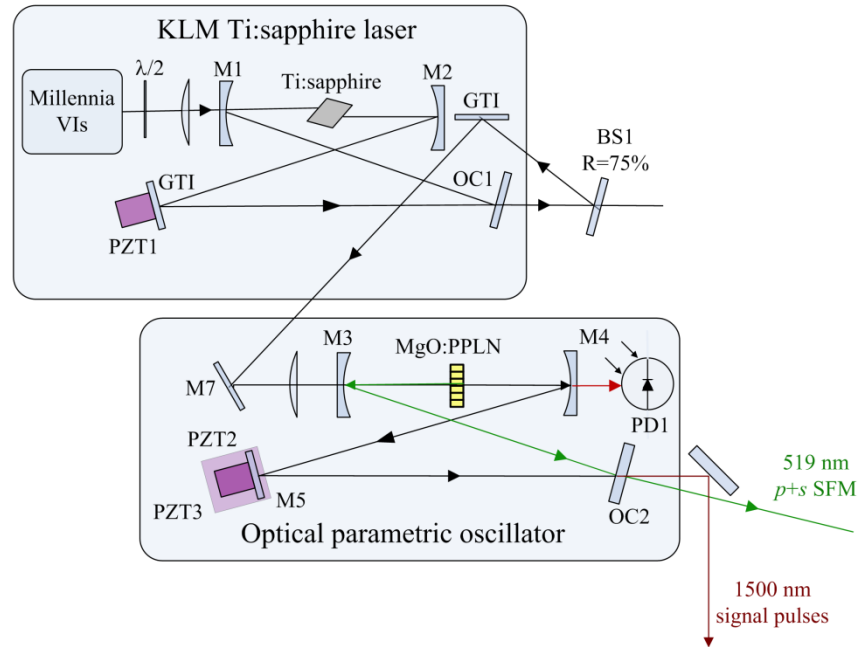


*Figure 2.24 Schematic of the OPO with additional external optics shown. An HR mirror was used to turn the main output with the signal pulses, later used in an external filter cavity. Light reflected back from the PPLN crystal contain pump + signal from SFM. This was used in one arm of an interferometer for locking the carrier-envelope-offset frequency of the signal pulses.*

Once a final cavity configuration for the OPO was established, a full characterisation of the signal pulses was carried out. The results for this are detailed below.



### 2.2.5. Characterisation of the optical parametric oscillator

The OPO was pumped with  $\sim 900$  mW average power from the Ti:sapphire laser. The average output power of the OPO varied with the tuning of the cavity length and wavelength. The maximum output was  $>100$  mW at close to 1500 nm. While the OPO remained running, this would vary with wavelength from approximately 15 mW up to 110 mW. The mirror coatings in the cavity were not the same for all the optics, but they are all in the range of 1450 – 1600 nm. The centre wavelength of the signal pulses from the OPO could be tuned from just below 1440 nm up to 1570 nm. A Newport Microdrive Controller (ESA-C) was used to vary the voltage to PZT3 (Thorlabs AE0203D04F, maximum displacement  $\sim 5$   $\mu\text{m}$ ) to change the wavelength of the signal (and idler) pulses. A voltage range of 150 V was used to obtain the tuning range shown in Figure 2.25. The central wavelength of the signal pulses did not tune smoothly or continuously with the decreasing cavity length. This was most likely due to water absorption in the atmosphere, although the reflection and dispersion curves for the optical coatings may also have affected the tuning.

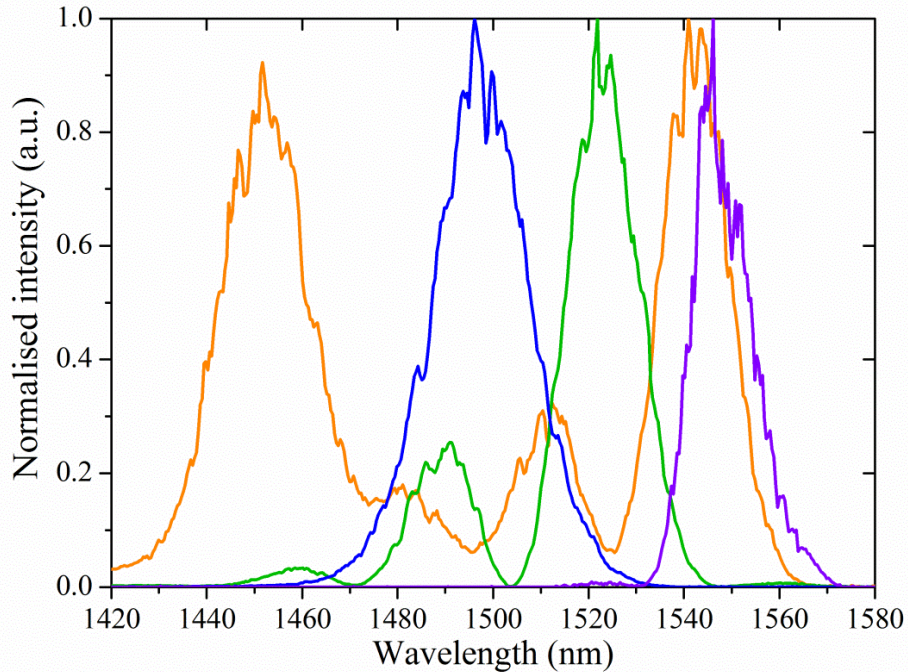
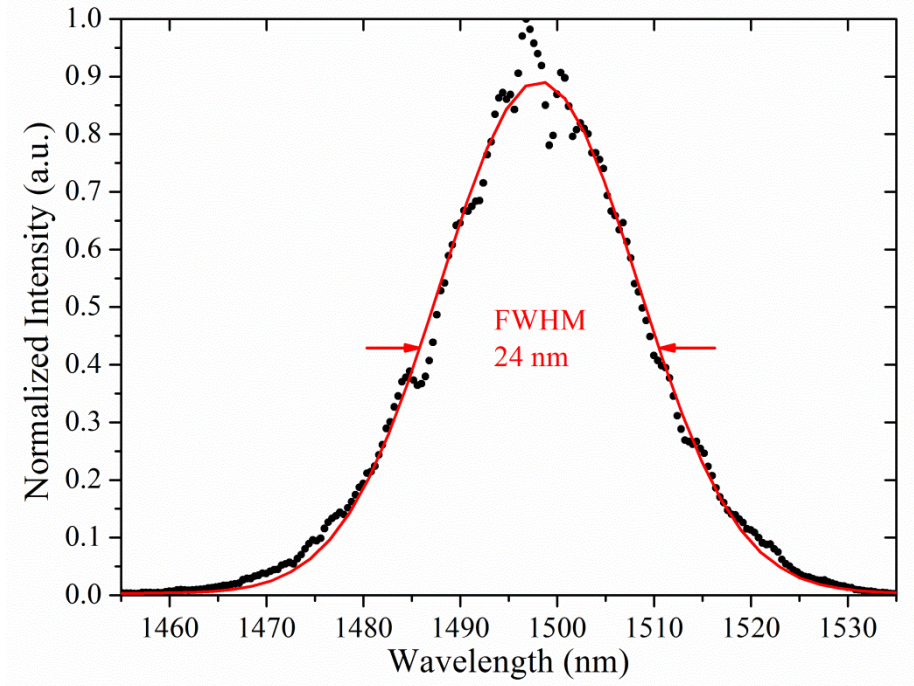


Figure 2.25 Optical spectra of the OPO signal pulses when the voltage to PZT3 was varied. The spectra above are shown for applied voltages of 9.8 V (purple), 110 V (orange), 120 V (green) and 130 V (blue). Spectra were measured using an OSA.

The CEO-frequency of the OPO would be locked close to the maximum average power at a wavelength of  $\sim 1500$  nm, so the spectrum at this position is shown in Figure 2.26. The FWHM bandwidth was 24 nm measured using a Gaussian fit for the data.



*Figure 2.26 Optical spectrum of the OPO signal pulses measured with an OSA. The FWHM bandwidth is 24 nm. The red line shows a Gaussian fit for the data.*

An autocorrelation of the signal pulses was measured at this wavelength using a ‘home-built’ autocorrelator using two-photon absorption on a silicon photodiode. The pulse duration was calculated as 135 fs for pulses with a Gaussian temporal fit, with no temporal chirp observed. The time-bandwidth product was calculated as 2.7, so the pulses were bandwidth limited within the experimental error of the measurements.

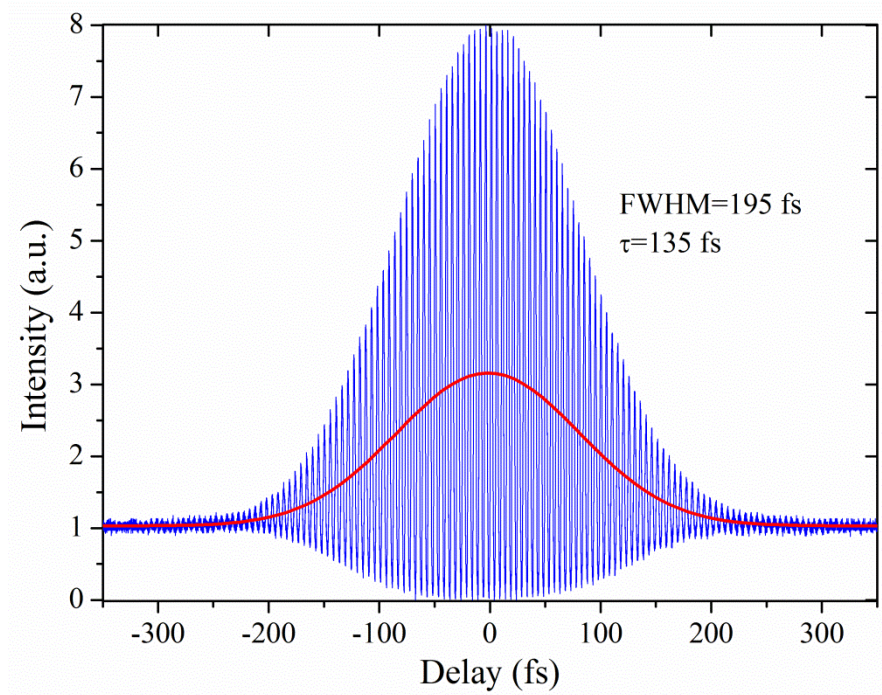


*Figure 2.27 Autocorrelation of the OPO signal pulses at 1500 nm (corresponding to Figure 2.26) measured using two-photon absorption in a ‘home-built’ autocorrelator. The FWHM pulse duration was calculated as  $\sim 135$  fs. No significant temporal chirp can be observed.*

The OPO can be run stably over a range of more than 100 nm with good average output powers. The highest output power was at close to 1500 nm, which is where any later measurements, such as spectroscopic measurements for a gas cell, were planned to be carried out.

### 2.3. Conclusions

A femtosecond KLM Ti:sapphire laser was built in a folded ring cavity with a repetition frequency of 280 MHz. The cavity design included two PZTs to be used for repetition frequency stabilisation for generating a stabilised frequency comb. Part of the output from this laser was used to pump a PCF for supercontinuum generation, which will be detailed in Chapter 3. The remainder of the Ti:sapphire laser output was used to pump a femtosecond OPO to generate signal pulses tunable around 1500 nm. This cavity contained two PZTs for tuning of the signal pulses’ wavelength and CEO-frequency in preparation for locking the CEO-frequency to generate a stabilised frequency comb. A

reflection from the PPLN crystal containing pump + signal SFM followed a different output path and was used for the CEO-frequency stabilisation.

In Chapter 3 the locking of the repetition frequency of the Ti:sapphire laser and the CEO-frequency of the OPO signal pulses will be detailed. This will include how the pump + signal SFM from the OPO and supercontinuum from the PCF were used in a nonlinear interferometer to generate a beat frequency that was used to lock the CEO-frequency of the signal pulses.

## **Chapter 3. Stabilisation of a synchronously pumped femtosecond optical parametric oscillator frequency comb**

Stabilised frequency combs provide useful optical sources for a range of applications in spectroscopy and metrology [9, 107]. By locking the repetition frequency and CEO-frequency for a train of pulses, the longitudinal frequency modes can be used as a ‘comb’ of stable lines – whose exact frequencies can be known with high precision – to use as a reference ‘ruler’ for any measurements [108, 109].

Chapter 2 described the optical configuration for the Ti:sapphire laser and OPO that were used to generate an ultrashort pulse train in the near-IR. Once the synchronously pumped OPO was completed, the optical system remained to be stabilised by feedback loops in order to establish a locked frequency comb. The repetition frequency of the Ti:sapphire laser was locked, which in turn locked the repetition frequency of the OPO by its synchronicity. The carrier-envelope-offset (CEO) frequency of the signal pulse train in the OPO was also locked to make the signal output of the OPO into a frequency comb. The CEO-frequency of the signal pulse train was detected using a nonlinear Mach-Zehnder interferometer, which included the OPO in one arm and a PCF in the other. The frequency detected by beating these sources gave the CEO-frequency of the signal pulses to enable locking.

Noise analysis was then carried out on the locked frequency comb. Measurements were taken for the relative intensity noise in the Ti:sapphire laser and the OPO outputs. Phase noise was measured, using the power spectral density and cumulative phase noise, for the CEO-frequency and repetition frequency of the OPO with, and without, stabilisation. Finally, two-sample frequency deviation and fractional instability were recorded for the locked frequency comb and locking loops to establish an upper limit on the noise level, which was found to be equipment-limited.

### **3.1. Locking a frequency comb**

#### ***3.1.1. Modelocked lasers – a comb of modes***

The output from an ideal modelocked laser can be described in the time-domain as a train of pulses with near-identical characteristics separated in time by a constant spacing and with each pulse having the same duration. If we consider a sufficiently large

number of pulses in the frequency-domain, an ideal laser can be described as a comb of very narrow longitudinal modes, with a constant separation, that can be traced back to a “zero-frequency” point on a graph. In reality however, there will always be fluctuations in the output of any laser as a result of temperature changes in the environment, mechanical and electronic noise, disturbances to the system through air currents and particles in the air, and other effects. These can be manifested as changes in the intensity of a laser output, which can be recorded using relative intensity noise, (RIN) measurements. They can also cause variations in the repetition frequency and changes to the difference between the group and phase velocities within the cavity.

The difference between the group and phase velocities cause a phase shift between consecutive pulses (described in Section 2.1.2). Both this phase shift and the repetition frequency of the modelocked source need to be locked to a precision frequency reference to realise a stabilised frequency comb [110].

### ***3.1.2. Repetition frequency***

The repetition frequency for a cavity presents as the mode separation in an optical frequency comb. If the pulses are stable, the mode separation between any two comb modes will be identical [111]. However, as temperature drifts and mechanical disturbances will cause variation in the cavity length, the repetition frequency (and mode separation for a comb) will not be constant, and will cause a broadening and drift of the comb lines for long time span or successive measurements. The repetition frequency can be easily measured using a fast photodiode and stabilised to a reference frequency [2, 7]. If the repetition frequency for a femtosecond laser synchronously pumping an OPO is stabilised, the repetition frequency of the OPO will also be stabilised.

### ***3.1.3. CEO-frequency***

For an ultrashort pulse train propagating through optical elements, the group and phase velocity of the pulses will be different. The pulse envelope, the square of which is the intensity profile, travels at the group velocity, and the carrier propagates with the phase velocity. The difference between the peak of the carrier wave of a pulse and the maximum of its envelope is the carrier-envelope-phase (CEP) of the pulse and this is



dependent on the difference between the group and phase velocity. The envelope and carrier wave for a few-cycle ultrashort pulse were illustrated in Figure 1.1.

In an optical cavity, such as a laser, small fluctuations in temperature, cavity length, alignment and pump intensity cause variations in the CEP through effects such as changes in the length of the gain medium and dispersion in the cavity. The change in CEP between successive pulses is the carrier-envelope-phase slip (CEPS). If the difference between group and phase velocity changes with the time, the CEP will change by a different amount pulse-to-pulse, so the CEPS will not be constant [1]. In most lasers systems the noise causing CEP variations is not controlled and the CEPS is constantly changing. A stabilised frequency comb requires that the CEPS ( $\Delta\phi_{CEP}$ ) is locked to a reference, so the change in CEP between consecutive pulses is always constant (see Figure 3.1).

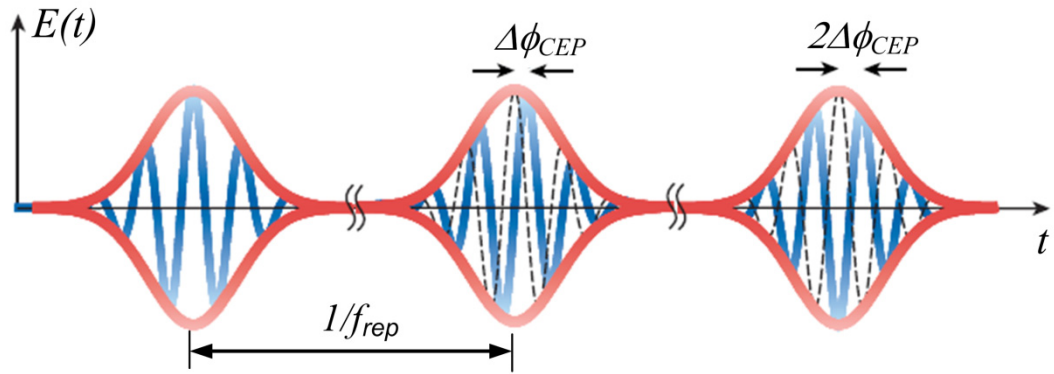


*Figure 3.1 CEP evolving for ultrashort pulses. In the absence of any noise in a system with dispersive elements, the CEP will change by a fixed value, the CEPS ( $\Delta\phi_{CEP}$ ). Figure adapted from image in [5].*

The electric field for a single, ultrashort pulse can be expressed in terms of the function of the envelope,  $E_0(t)$ , the angular frequency of the carrier wave,  $\omega_c$ , and the CEP of the pulse,  $\phi_{CEP}$ , to give Equation 3.1 [1]:

$$E_p(t) = E_0(t) \exp [i(\omega_c t + \phi_{CEP})] \quad \text{Equation 3.1}$$

For a train of pulses we can write the electric field as:

$$E(t) = \sum_n E_p(t - n\tau) \quad \text{Equation 3.2}$$

where  $\tau$  is the time between pulses and greater than the pulse duration  $E_p(t)$ .

The CEPS has been ignored temporarily to simplify the expression [1]. This is periodic with  $\tau$  and can be expressed as a Fourier series using the Poisson sum formula:

$$\sum_{m=-\infty}^{\infty} f(x - m\tau) = \sum_{k=-\infty}^{\infty} \frac{1}{\tau} F\left(\frac{k}{\tau}\right) \exp[(2\pi i k x)/\tau] \quad \text{Equation 3.3}$$

where  $F(y)$  is the Fourier transform of  $f(x)$ . The optical spectrum is therefore a comb of frequency lines that are integer multiples of the repetition frequency ( $f_{rep} = 1/\tau$ ) [1]. But if we consider the CEPS, the pulses will no longer be identical and their spectrum cannot be described using this Fourier series. The electric field can be rewritten for a pulse,  $n$ , using Equation 3.1 and the equation  $\phi_{CEP} = n\Delta\phi_{CEP} + \phi_0$  to give:

$$\begin{aligned} E(t) &= \sum_n E_0(t - n\tau) \exp[i(\omega_c t - n\omega_c \tau + n\Delta\phi_{CEP} + \phi_0)] \\ &= \sum_n E_0(t - n\tau) \exp[i(\omega_c t + n(\Delta\phi_{CEP} - \omega_c \tau) + \phi_0)] \end{aligned} \quad \text{Equation 3.4}$$

The Fourier transform of this is [1]:

$$\begin{aligned} E(\omega) &= \int \sum_n E_0(t - n\tau) \exp[i(\omega_c t + n(\Delta\phi_{CEP} - \omega_c \tau) + \phi_0)] \exp(-i\omega t) dt \\ &= \sum_n \exp[i(n(\Delta\phi_{CEP} - \omega_c \tau) + \phi_0)] \int E_0(t - n\tau) \exp[-i(\omega - \omega_c)t] dt \end{aligned} \quad \text{Equation 3.5}$$

Using the identity:  $\int f(x - a) \exp(-iax) dx = \exp(-iaa) \int f(x) \exp(-iax) dx$

and the substitution:  $\tilde{E}(\omega) = \int E_0(t) \exp(-i\omega t) dt$

with the reverse of Equation 3.3 this becomes [1]:

$$\begin{aligned} E(\omega) &= \sum_n \exp[i(n(\Delta\phi_{CEP} - \omega_c \tau) + \phi_0)] \exp[-in(\omega - \omega_c)\tau] \tilde{E}(\omega - \omega_c) \\ &= \exp(i\phi_0) \tilde{E}(\omega - \omega_c) \sum_n \exp[i(n\Delta\phi_{CEP} - n\omega\tau)] \\ &= \exp(i\phi_0) \tilde{E}(\omega - \omega_c) \sum_n f_{CEO}(\Delta\phi_{CEP} - \omega\tau - 2\pi m) \end{aligned} \quad \text{Equation 3.6}$$

This is a frequency comb with modes at:

$$\omega_m = \frac{2m\pi}{\tau} - \frac{\Delta\phi_{CEP}}{\tau} \quad \text{Equation 3.7}$$

or alternatively [1]:

$$f_m = mf_{rep} + f_{CEO} \quad \text{Equation 3.8}$$

where

$$f_{CEO} = -\frac{\Delta\phi_{CEP}f_{rep}}{2\pi} \quad \text{Equation 3.9}$$



This shows the optical spectrum to be a frequency comb of longitudinal modes separated by the repetition frequency and shifted from exact integer multiples of this by the CEO-frequency, which is determined by the CEPS [1].

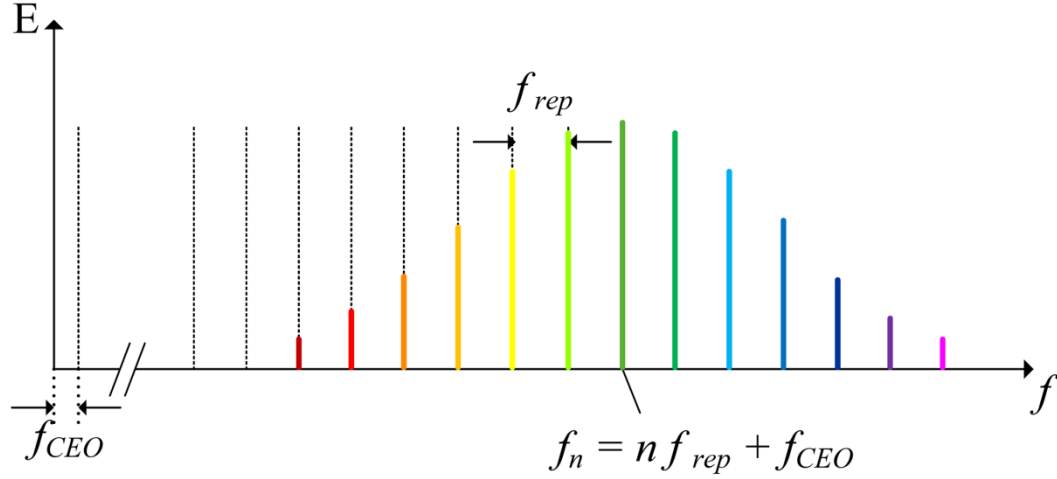


Figure 3.2 A frequency comb of longitudinal modes for an ultrashort pulse train. The comb lines are separated by  $f_{rep}$  and offset from the origin of the frequency-axis by the  $f_{CEO}$ .

For a locked frequency comb the frequency mode spacing,  $f_{rep}$ , is fixed, and the modes are offset from exact multiples of this by the fixed frequency,  $f_{CEO}$ , with line position and width limited by the stability and noise in the reference frequency source used for locking. A frequency comb for a train of ultrashort pulses is presented in Figure 3.2.

The CEO-frequency control in any system will be limited by the locking electronics used, the pump source for the system and, ultimately, the quantum limit for phase noise, which is lower for shorter pulses. This means that lasers producing shorter pulses have a lower absolute limit for the noise levels in a frequency comb [112]. High repetition frequencies also provide an advantage by reducing the minimum possible width of the comb lines, within a fixed sample period.

Fluctuations in the CEO-frequency of pulse trains have been known to have significance in some nonlinear processes for some time, however in the late 1990's there was still no convenient method for measuring and controlling this. Additional oscillators and CW lasers were generally needed to measure the CEO-frequency and these led to large and complex system designs [3]. Measurements could be made using frequency combs with repetition frequencies monitored by chains of optical systems with HeNe or diode lasers at known frequencies [113, 114], however direct

measurements of the CEO-frequency to enable full stabilisation of frequency combs had still not been realised.

During the 1990's, a range of optical fibre structures were being investigated, including microstructure fibres. Microstructure fibres have a complex cross-section of many high and low index regions, as with photonic crystals, and so are also referred to as photonic crystal fibres, or PCF. In 1996, a low-loss fibre consisting of silica and air holes was successfully demonstrated to be single mode across a wavelength range of over 1000 nm [115, 116]. In 1997 this range was shown to extend towards the mid-IR part of the spectrum, although the single-mode guiding was limited by the bend radius of the fibre [117]. An example of the PCF used for this broadband single mode guiding is shown in Figure 3.3. At the end of 1999, Ranka *et al.* demonstrated a silica PCF that could be used for continuum generation with anomalous dispersion for visible wavelengths [118], something that could be advantageous for frequency comb work.

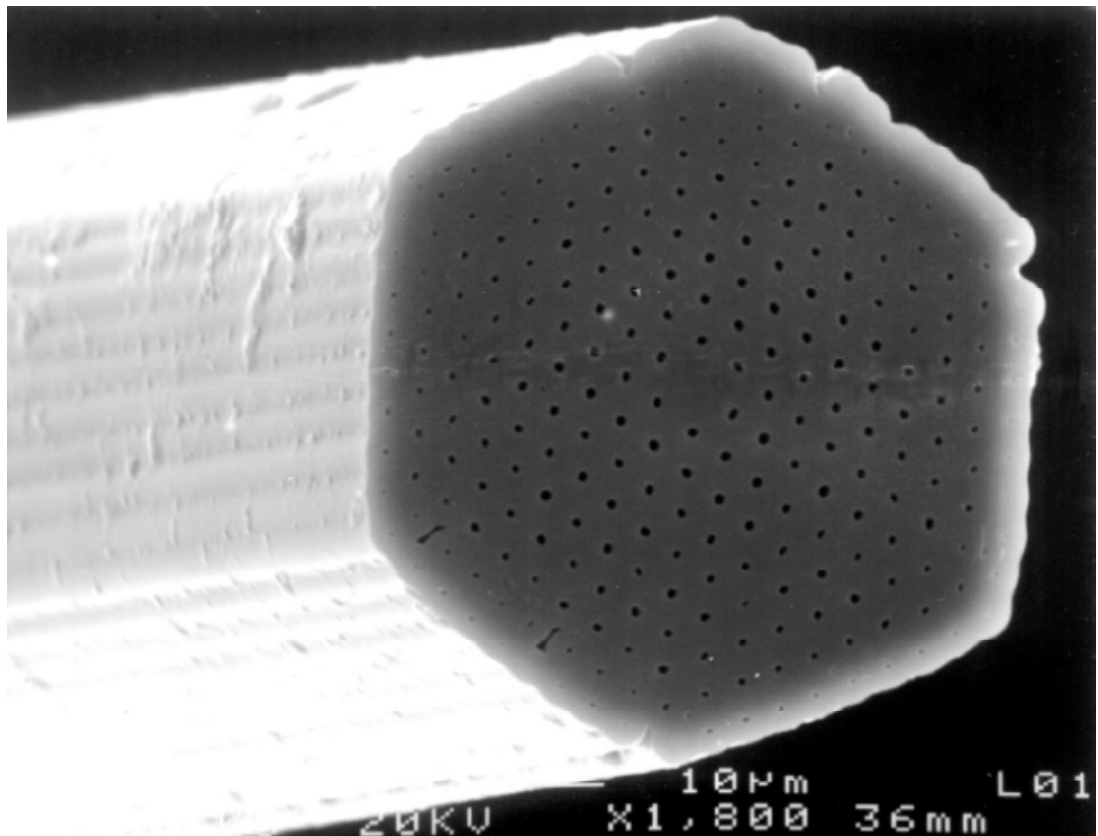


Figure 3.3 Scanning electron micrograph of a PCF. A hexagonal array of air holes encloses a solid core. The solid core is  $\sim 4.5 \mu\text{m}$  across with a pitch (centre of hole to centre of hole) of  $\sim 2.3 \mu\text{m}$ . The total width of the fibre is  $\sim 48 \mu\text{m}$ . Image from [116].

The guiding properties and behaviour of photonic crystal fibres are determined by the type of structure used: the air hole size and spacing; the size of the core and the number of layers of holes surrounding this. Small core fibres with large air holes give a large core-cladding index contrast and therefore large effective nonlinearity; with appropriate dispersion, strong nonlinear interactions can be achieved for relatively low pulse energies. The large air-filling fraction means waveguide dispersion dominates, and reducing the core diameter will reduce the wavelength at which zero GVD will be present [119]. A core of 2  $\mu\text{m}$  can give a zero GVD point in a wavelength range corresponding to Ti:sapphire oscillators, at  $\sim 800$  nm. The third-order dispersion is also affected by the air-filling fraction, and can lead to an almost flat GVD across a wide wavelength range. The optical nonlinearities in the PCF can lead to pulse broadening and supercontinuum generation, and also soliton behaviour for ultrashort pulses [119]. The behaviour of ultrashort pulses in PCF as a result of these nonlinearities has led to them being exploited across a range of application and areas in physics [120, 121], including optical frequency combs [122].

In 2000, Jones *et al.* stabilised the CEO-frequency of femtosecond pulses from a modelocked Ti:sapphire laser using a self-referencing technique commonly referred to as f-2f self-referencing [12]. Pulses from the laser are broadened in wavelength by supercontinuum generation in the PCF. Part of the output from the fibre is then frequency doubled in a BBO crystal in one arm of a Mach-Zehnder interferometer, with the rest of the light propagating in the other arm with no nonlinear crystal. The longer wavelengths in the frequency doubling arm will now overlap with the shorter wavelengths in the arm that wasn't frequency doubled (see Figure 3.4). The pulses in the doubled arm have a CEO-frequency which is double that of the other arm, so the beat frequency detected after the beams are recombined will be equal to the CEO-frequency of the laser pulses [12]. This technique is now used to measure the CEO-frequency in almost all stabilised laser frequency combs [1, 123].

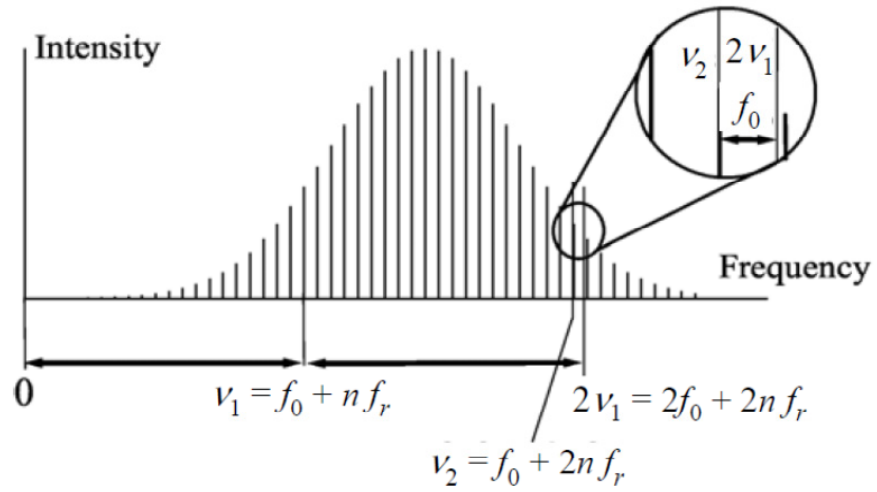


Figure 3.4 Frequency  $\nu_2$  is interfered with  $2\nu_1$ , to give the CEO-frequency, presented here as  $f_0$ , with repetition frequency as  $f_r$ . Figure taken from [111].

Once the CEO-frequency has been measured, it can be compared to a reference frequency in a number of ways and the difference between them can be used as feedback to a component in the laser cavity that can vary the CEO-frequency [12]. Prevedelli *et al.* presented a phase frequency detector (PFD) circuit in 1995 that could be used for locking the phase of diode lasers for use in optical frequency chains [124]. A PFD circuit can be used to measure the difference between the CEO-frequency detected and a reference frequency. This difference in frequency (or phase) is then expressed as a voltage level to feed back to the element or equipment that controls the CEO-frequency, varying the dispersion and therefore the difference between the group and phase velocities. This is typically a PZT for an end mirror in a synchronously pumped femtosecond OPO [31, 36].

Tilting the angle of an end-mirror in a laser cavity containing prisms is also a convenient way of changing the CEO-frequency; otherwise using AOMs and EOMs to vary the pump intensity to change the Kerr lensing in a crystal will also change the GDD of the cavity, and therefore the CEO-frequency of the pulses [111].

In this thesis the CEO-frequency of the signal pulses of a synchronously pumped femtosecond OPO was stabilised. From the coupled wave equations for nonlinear processes in an OPO, the fixed phase relationship between the CEP of the pump, signal and idler can be derived such that [24, 34]:

$$\phi_{CEP}^p = \phi_{CEP}^s + \phi_{CEP}^i - \frac{\pi}{2} \quad \text{Equation 3.10}$$

The time derivative can then be taken to relate the rate of change in CEP between these components [24, 34]. In the frequency domain, this can be expressed as:

$$f_{CEO}^p = f_{CEO}^s + f_{CEO}^i \quad \text{Equation 3.11}$$

When an OPO is used as a stabilised frequency comb, the laser pumping it is usually CEO-frequency stabilised, and then by CEO-frequency stabilising any other output from the OPO containing a signal or idler component, all the remaining components generated by nonlinear processes will also be CEO-frequency stabilised [26, 29, 39].

In this thesis the CEO-frequency of the pump laser was left free-running and only the signal pulses from the OPO were CEO-frequency stabilised. This was done by beating the pump + signal from SFM in the OPO with the pump supercontinuum. This beat frequency was equal to the CEO-frequency of the signal pulses and so could be used in a feedback loop to stabilise this through changes in the OPO cavity length. The interference of the pump + signal SFM with the pump supercontinuum is explained in Figure 3.5.

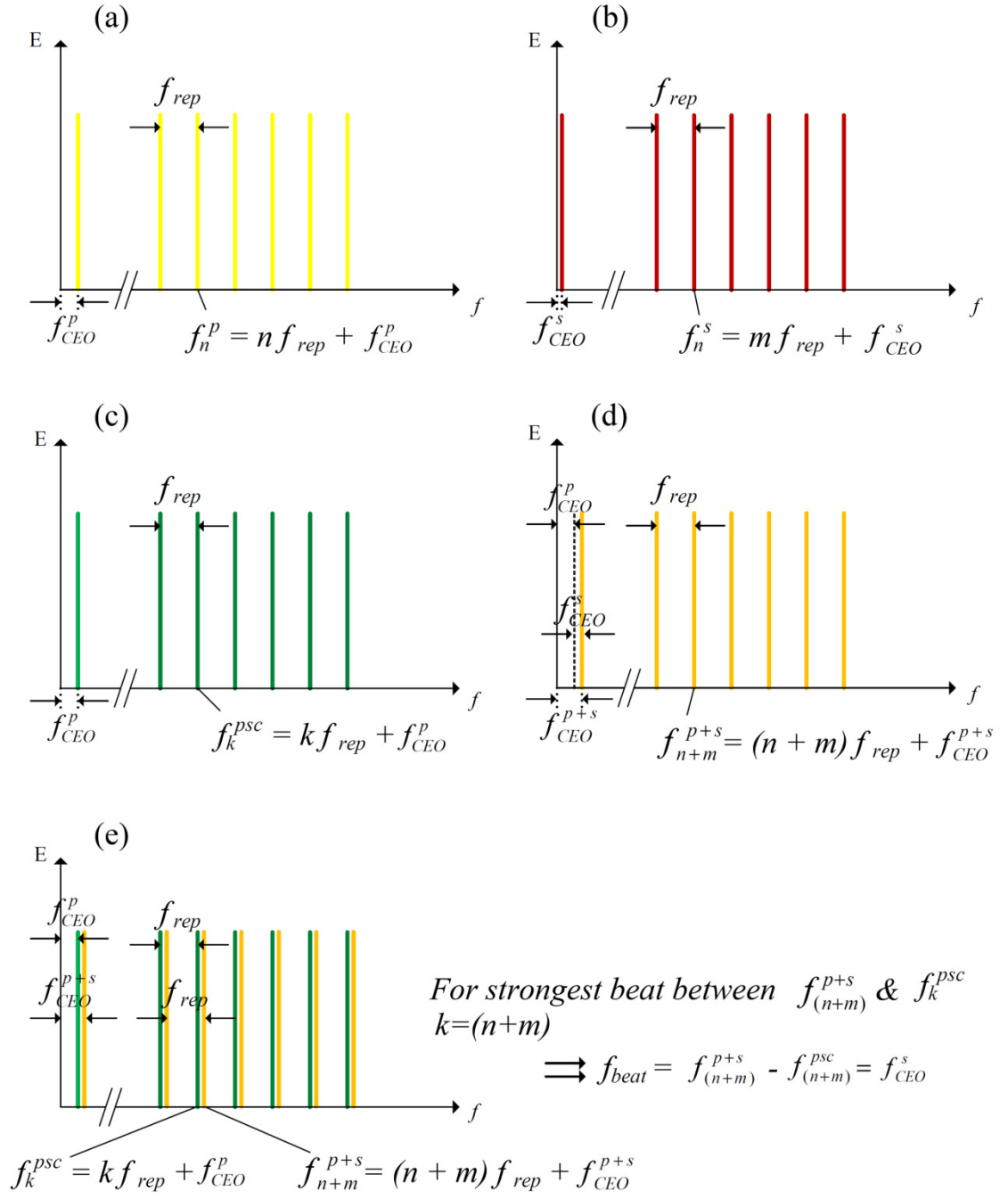


Figure 3.5 Frequency domain representation of the pulse trains present in the optical system. (a) Pump. (b) Signal. (c) Pump supercontinuum. (d) Pump + signal from SFM in the OPO crystal. (e) Pump + signal SFM pulse train beat with pump supercontinuum. The beat frequency measured is equal to the CEO-frequency of the signal pulses.

### 3.1.4. Phase noise

For an ideal monochromatic laser, the electric field can be described as:

$$E(t) = [E_0 e^{i(\omega_0 t + \phi)}] \quad \text{Equation 3.12}$$

where  $\phi$  is constant. However, in reality no laser produces perfectly monochromatic light due to random phase and amplitude fluctuations. This leads to a laser output with a finite linewidth. This is the phase noise and leads to a new equation for the electric field:

$$E(t) = [E_0 e^{i(\omega_0 t + \phi(t))}] \quad \text{Equation 3.13}$$

where  $\phi(t)$  is slowly varying [125].

For a modelocked laser or OPO that is controlled to generate a stabilised frequency comb, the position of any comb line can be described using the repetition frequency and CEO-frequency. Fluctuations in these quantities are another example of phase noise and cause broadening of the comb lines. In this research, the phase noise for the CEO-frequency and repetition frequency were measured. This was done by using the output from a PFD circuit for the CEO-frequency and the output from a mixer for the repetition frequency. These outputs were calibrated to turn the measured voltages into a phase, and then a power spectral density (PSD) was taken of the results. A cumulative phase noise measurement was taken by summing the noise across the frequency range recorded, which is equal to the root-mean-square (RMS) noise for the frequency [123], and this can then be used for noise comparisons with other locking loops and systems.

The phase noise can be quantified using the PSD function, which describes the noise power per unit frequency interval. The PSD of the phase noise does not describe the actual physical power present, but rather the squared value of the signal, (in this case phase in radians) and so is given in units of  $\text{rad}^2/\text{Hz}$ . The general equation for PSD is estimated as follows below [126, 127]. Using the Fourier transform equations for a quantity  $h(t)$  that is a function of time:

$$H(\omega) = \int_{-\infty}^{\infty} h(t) e^{i\omega t} dt \quad \text{Equation 3.14}$$

$$h(t) = \frac{1}{2\pi} \int_{-\infty}^{\infty} H(\omega) e^{-i\omega t} d\omega \quad \text{Equation 3.15}$$

or for frequency, substitute  $\omega \equiv 2\pi f$  to obtain [126]:

$$H(f) = \int_{-\infty}^{\infty} h(t) e^{2\pi i f t} dt \quad \text{Equation 3.16}$$

$$h(t) = \int_{-\infty}^{\infty} H(f) e^{-2\pi i f t} df \quad \text{Equation 3.17}$$

The expression for total power is then (from Parseval's theorem):

$$\text{Total power} = \int_{-\infty}^{\infty} |h(t)|^2 dt = \int_{-\infty}^{\infty} |H(f)|^2 df \quad \text{Equation 3.18}$$

and so to calculate the power in a frequency interval, or power spectral density:

$$P_h(f) = |H(f)|^2 + |H(-f)|^2 \quad \text{Equation 3.19}$$

for  $0 \leq f \leq \infty$  [126].

The analysis for the results in this thesis used discrete Fourier transforms, as a finite number of points were sampled. Thus our discrete Fourier transform of  $N$  points for quantity  $h_j$  will be of the form [127]:

$$H_k \equiv \sum_{j=0}^{N-1} h_j e^{2\pi i j k / N} \quad \text{Equation 3.20}$$

A factor of the sampling interval is introduced to equate this to the original Fourier transform  $H(f)$ . The phase noise PSD can then be normalised using the mean-squared-amplitude. The integral of the PSD over the range of 0 to the upper limit of the Nyquist frequency is equal to half the mean-squared-amplitude and this can be used to normalise the PSD for each frequency [127]. This was then plotted on a graph of the phase noise PSD against frequency.

The normalised PSD can now be integrated over the frequency range (which is dependent on the sampling rate used) to give the cumulative phase noise using:

$$\Delta\phi_{cum} = \left[ 2 \int_1^{f_{Nyquist}} P_{\phi}(f) df \right]^{1/2} \quad \text{Equation 3.21}$$

where,  $P_{\phi}(f)$  is the normalised PSD,  $f_{Nyquist}$  is the Nyquist frequency and  $f$  is a frequency relative to the chosen lock frequency for the locking loop [1].

This method of phase noise characterisation was used for both the CEO-frequency and repetition frequency locking loops. The same analysis with PSD was also used for the relative intensity measurements detailed in the next section.

Another mathematical technique for characterising noise in a locking loop involves taking a time-series two-sample frequency deviation for the CEO-frequency and repetition frequency. By using a frequency counter to take the mean of a frequency signal over different gate times, an average-to-average deviation can be taken to characterise the variation over time of this signal. This measures the Allan deviation



(Equation 3.22), which is similar to a standard deviation (Equation 3.23), but compares adjacent data points rather than data points and the overall mean. The standard deviation for this data was also recorded for comparison.

$$\text{Allan deviation} = \sqrt{\frac{1}{2(N-1)} \sum_{i=1}^{N-1} (y_{i+1} - y_i)^2} \quad \text{Equation 3.22}$$

$$\text{Standard deviation} = \sqrt{\frac{1}{N-1} \sum_{i=1}^N (y_i - \bar{y})^2} \quad \text{Equation 3.23}$$

### 3.1.5. *Relative intensity noise*

The relative intensity noise (RIN) is the relative fluctuation of a signal in a 1 Hz bandwidth and can be defined as the mean-squared noise power divided by the square of the average power [128]. It can also be represented using a PSD plot, as with phase noise, but with signal strength at a frequency relative to the average considered rather than above, where measurements were for an absolute phase. The RIN measurements in this thesis were taken by subtracting the average signal from each data point, to give the fluctuations without the DC component. So the cumulative standard deviation is equivalent to the RMS noise for the results. The discrete Fourier transform for the fluctuation data was then used and multiplied by its conjugate to give a spectral density in the same method described previously [127]. This was normalised, as with the phase noise PSD described above, and changed to a dB scale, which is more common for RIN measurements [128]. It was calculated relative to the mean signal, so the units used to plot the results are dBc<sup>2</sup>/Hz, where “c” is the carrier (mean). The cumulative standard deviation was also dealt with slightly differently from the phase noise, being calculated as a percentage relative to the mean.

## 3.2. **CEO-frequency stabilization of a femtosecond optical parametric oscillator**

Once the Ti:sapphire laser and OPO were built, the output needed to be CEO-frequency and repetition frequency stabilised. The CEO-frequency of the OPO signal pulses was locked first. OPO frequency combs usually have the CEO-frequency of the pump laser stabilised using f-2f self-referencing [3, 12], and then a second interferometer is used to interfere either the signal SHG pulses [36], or the pump + idler/signal SFM pulses [10], with the remaining pump supercontinuum to obtain a beat for locking the CEO-frequency of the remaining components. However interfering the pump + signal

SFM pulses with the pump supercontinuum gives a beat frequency exactly equal to the CEO-frequency of the signal pulses, with the significant advantage that noise in the CEO-frequency of the pump pulses will be suppressed by common-mode rejection [10]. For the work in this thesis, only the signal pulses needed to form a stabilised frequency comb. This meant that the CEO-frequency of the pump and idler could be left free-running without any increased noise in the signal pulses. This simplified system had only one interferometer for beating the pump supercontinuum with the pump + signal SFM pulses from the OPO. The absence of an  $f$ - $2f$  interferometer has the addition advantage of reducing the noise in the overall comb by decreasing the electronic loops feeding back into it [44].

### ***3.2.1. Optical and mechanical configuration***

The CEO-frequency of the signal pulses was detected using a nonlinear interferometer. A Mach-Zehnder interferometer was used with the Ti:sapphire light being divided at a 75% reflecting beamsplitter (BS), where 25% was used to pump a PCF and 75% was used to pump an OPO. In the OPO arm, some pump + signal SFM pulses were reflected back off the PPLN crystal and exited the output coupler at an angle to the main output beam. This light was then recombined with the pump supercontinuum from the PCF to obtain the CEO-frequency. The optical configurations for the laser and OPO are shown in Figure 3.6.

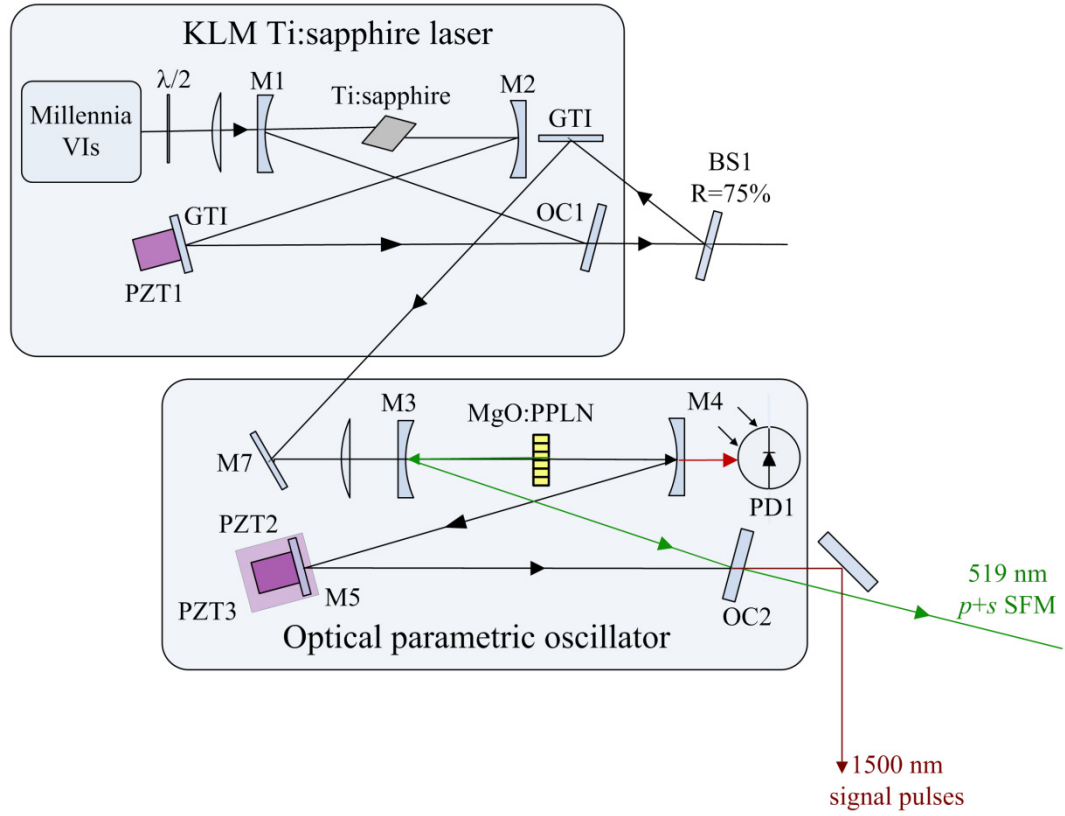


Figure 3.6 Schematic for the Ti:sapphire laser and OPO from Chapter 2. The interferometer started at BS1 so the OPO forms one arm and the transmitted light focussed in the PCF forms the other. The interference of the two beams together again is shown in Figure 3.7 below.

The light transmitted through BS1 was reflected off a GTI ( $\sim 500 \text{ fs}^2$  at normal incidence for 800 nm) and an HR mirror before propagating through a half-wave plate and being focussed into the PCF (Crystal Fibre A/S, 30 cm length, NL-2.0-740). The average power and spectrum from the PCF were monitored for the use of one, two and no GTI mirrors between BS1 and half-wave plate to optimise the anomalous dispersion on the pulses to give the highest power at short wavelengths in the supercontinuum. The half-wave plate was rotated to maximise the output from the PCF at 519 nm (and later on small adjustments of this were used to maximise the strength of the beat frequency for the signal CEO-frequency). A range of aspheric lenses were tested to optimise the coupling into the PCF, and for measurements comparing the average power before the half-wave plate and PCF and after the fibre the highest efficiency achieved was  $\sim 60\%$  transmission.

The light output from the PCF passed through quarter- and half-wave plates for 519 nm, which were also rotated to optimise the strength of the beat frequency at the avalanche

photodiode (APD) by maximising the light transmitted through the polarising beamsplitter (PBS). The unlabelled mirrors in Figure 3.7 were silver or aluminium. Two of these were mounted on a micrometer translation stage to vary the interferometer arm length to find the beat frequency between the supercontinuum and pump + signal SFM pulses.

The pump + signal SFM pulses reflected from the PPLN crystal were reflected through a half wave plate to maximise the reflection at the PBS. The reflected light then passed along the same path as the supercontinuum, with a diffraction grating (Comar 2400 lines/mm BK7 glass) dispersing the light so an iris could be used to ensure only a narrow bandwidth was focussed onto the APD (Becker & Hickl GmbH APM-400-N). The polariser was rotated to maximise the signal-to-noise ratio of the beat frequency for the CEO-frequency detected at the APD. The optical path lengths of the two arms of the interferometer were exactly matched to ensure the corresponding pulses were interfered at the APD, and the alignment of the recombined beams was checked over a long distance ( $>1$  metre) to maximise the strength of the beat frequency.

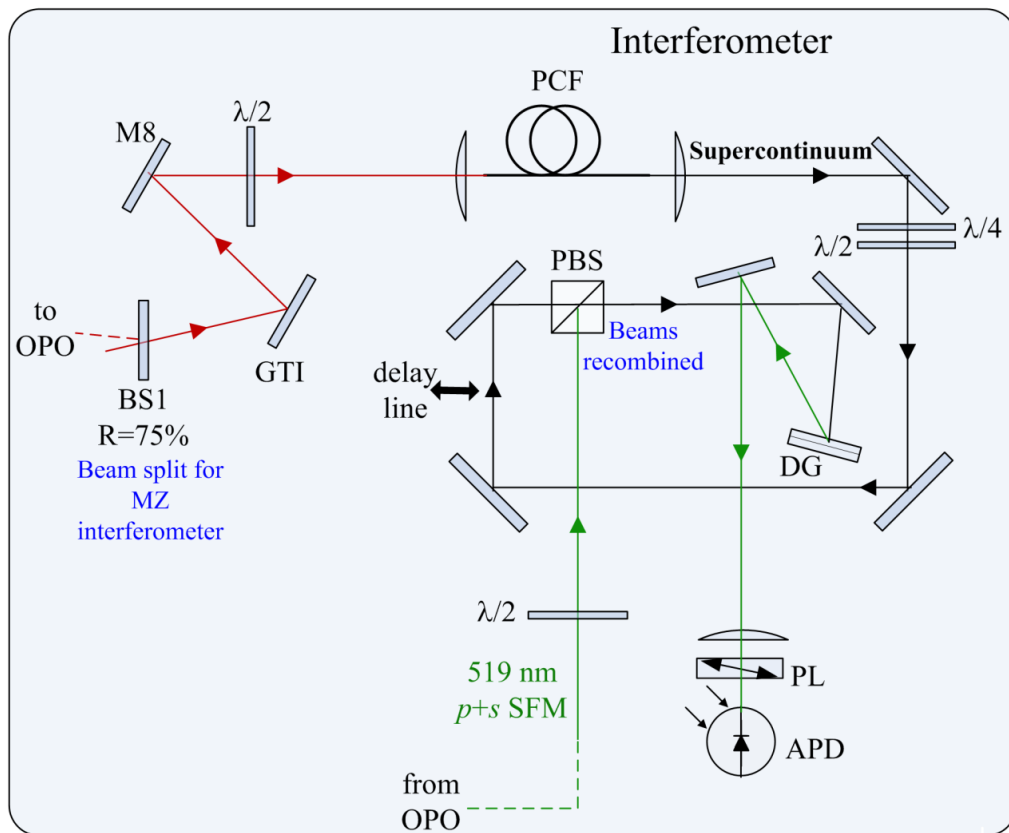
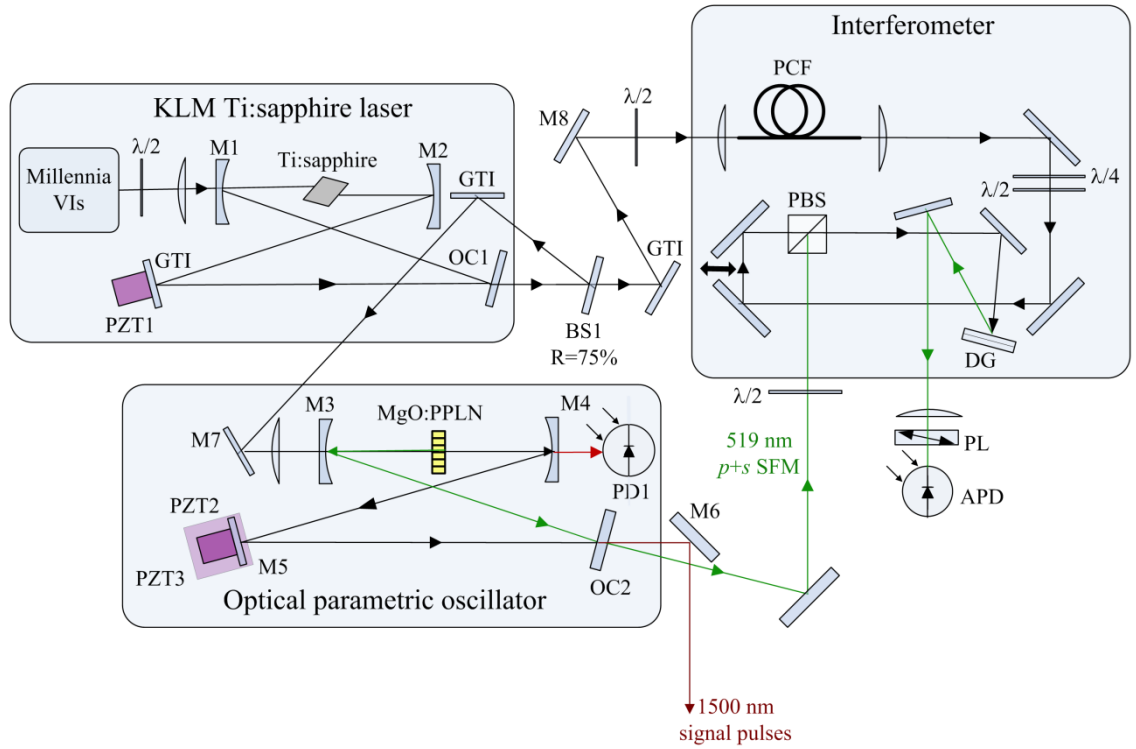


Figure 3.7 Optical configuration for the nonlinear Mach-Zehnder interferometer, not showing the OPO. PCF, photonic crystal fibre; PBS, polarising beam splitter; DG, diffraction grating; PL, polariser; APD, avalanche photodiode.

The complete optical configuration for the interferometer is presented in Figure 3.8. The alignment and polarisation for the PCF arm before and after the fibre, and for the OPO arm before the PBS were optimised, in addition to the polariser rotation and the delay line optical path length to maximise the overall signal strength and signal-to-noise ratio of the signal CEO-frequency beat detected at the APD.



*Figure 3.8 Full optical configuration for the laser, OPO and interferometer. The arm lengths for the interferometer were exactly matched and the alignment and polarisation were adjusted to optimise the strength of the signal at the APD.*

The optical spectra of the pump supercontinuum from the PCF and the pump + signal SFM from the OPO must overlap to obtain a strong beat frequency for the signal CEO-frequency. Spectra were recorded for these before and after the diffraction grating to ensure there was sufficient overlap (see Figure 3.9). Early work was done using an interference filter (Comar 532IN 25) with 3 nm bandwidth for transmission at 532 nm, turned at an angle to transmit light at close to 519 nm [23, 44]. This allowed a wider bandwidth than using a diffraction grating. Although the change to a grating did not have any effect on the noise in the CEO-frequency locking loop, it did increase the signal-to-noise ratio for the beat frequency so it was easier to obtain the initial lock. The relative strength of the beat frequencies is shown in Section 3.2.3.

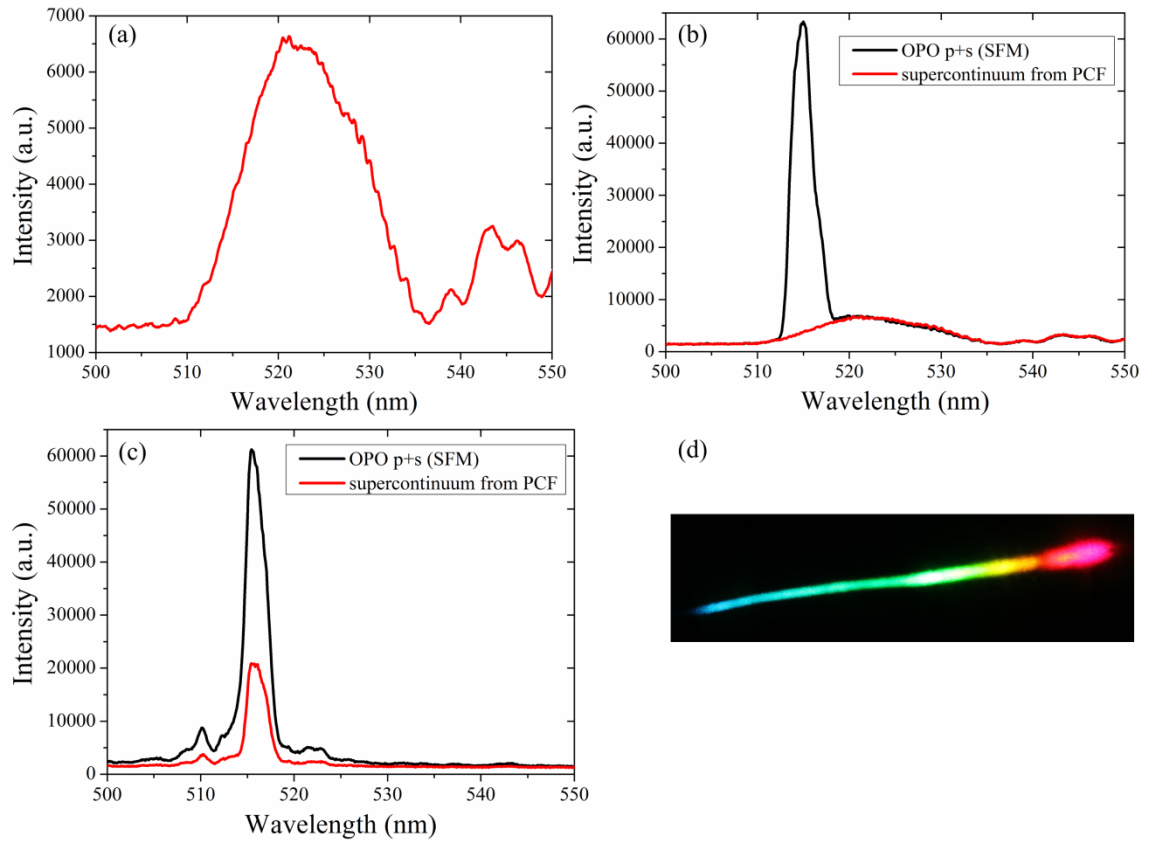


*Figure 3.9 Spectra for the pump supercontinuum from the PCF and the pump + signal SFM from the OPO recorded on an Ocean Optics visible wavelength spectrometer. (a) Supercontinuum from the PCF up to 550 nm before the diffraction grating. The spectrum continued down to  $\sim 490$  nm. (b) pump + signal SFM from the OPO with the supercontinuum on one graph for scale. (c) SFM and PCF output after the diffraction grating. An iris was used to select the required wavelength region. (d) Photograph of the supercontinuum generated in the PCF.*

The polariser before the APD was used to balance the two interferometer arms so the signal strengths at the detector were equal. This resulted in the highest signal-to-noise ratio with a strong signal strength from the detector.

A spectrum was recorded from 480 – 1250 nm for the pump supercontinuum from the PCF. The graph in Figure 3.10 plots data from measurements from an Ocean Optics visible spectrometer and an Ando AQ6317B OSA. Noise on the OSA prevented measurements at higher wavelengths.

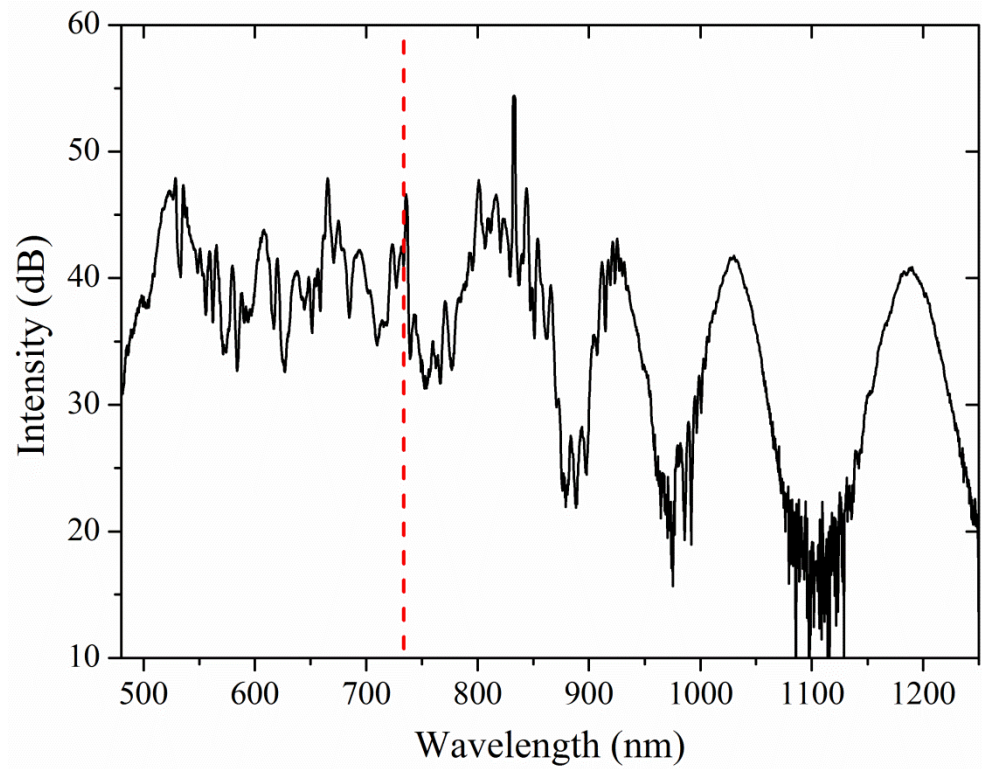


*Figure 3.10 Spectrum of pump supercontinuum from PCF. Wavelengths up to 732 nm were recorded on Ocean Optics visible spectrometer; wavelengths from 732 nm upwards were recorded using an Ando AQ6317B Optical Spectrum Analyzer. Red dashed line marks where data was joined.*

### **3.2.2. Electrical locking loops**

The beat frequency detected at the APD from the pump supercontinuum and the pump + signal SFM from the OPO was equal to the CEO-frequency of the signal pulses. The optical configuration and locking loop used to stabilise the CEO-frequency are presented in Figure 3.11. The beat frequency was monitored with an RF spectrum analyser (Agilent E4411B ESA-L series), and a Newport Microdrive Controller (ESA-C) was connected to PZT3 (Thorlabs AE0505D08F) to tune the CEO-frequency over its 280 MHz range. An Agilent signal generator (8664A) was used to generate a 10 MHz reference signal for one input of an analogue to digital converter (Pulse Research Lab L-350 TTL Dual-Channel Converter).

A Mini-Circuits (M-C) amplifier (Amp 1) increased the signal from the APD (Mini-Circuits ZFL-500LN originally and later a ZKL-1R5+ was used in series with this to increase the overall signal strength) which was then low-pass filtered (M-C 15 MHz LPF) before entering the other input port of the Dual-Channel Converter. The

outputs of this circuit then served as the two inputs to the PFD circuit (based on the design by Prevedelli *et al.* [124]) and the output of this then in turn served as the input to a New Focus LB1005 proportional-integral (PI) amplifier (Amp 2). The corner frequency, low frequency gain limit and gain on the amplifier were optimised for the most stable CEO-frequency lock ( $f_{\text{corner}} = 10 \text{ kHz}$ , LF gain limit = 40 dB) by shaping the feedback to PZT2 (Thorlabs AE0203D04F). The HR mirror mounted on PZT2 was cut-down ( $\sim 8 \times 8 \times 2 \text{ mm}$ ) to reduce the mechanical load on the PZT.

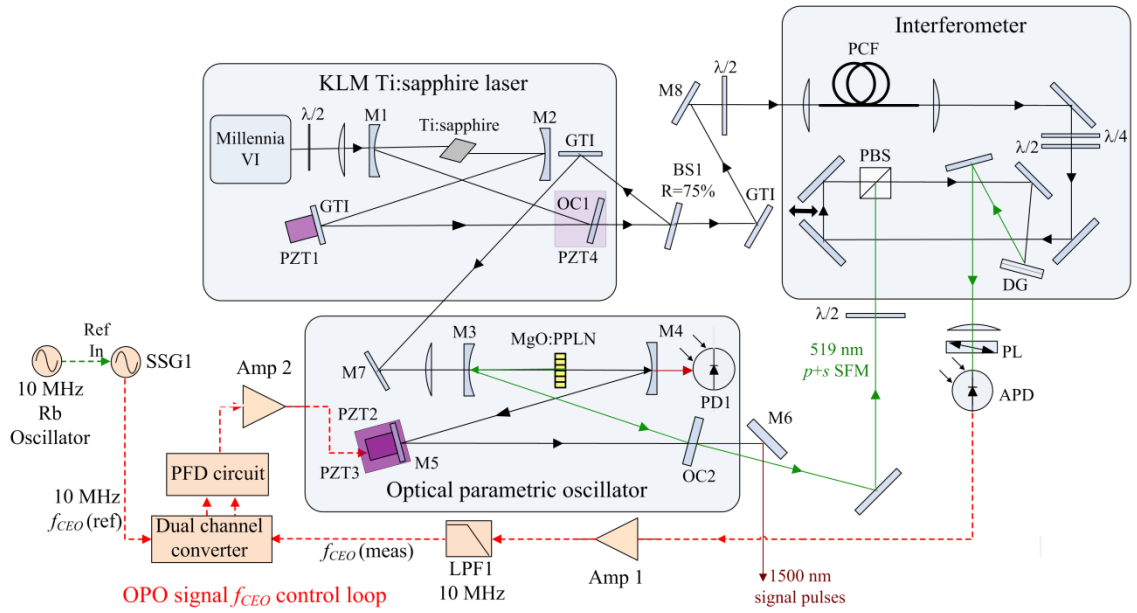


Figure 3.11 The optical and electronic configuration for a CEO-frequency stabilised OPO. The beat frequency at the APD was amplified, filtered and converted to a digital signal, along with a 10 MHz reference signal, to provide an error signal to a PI amplifier (Amp 2), which provided a voltage level to PZT2 to vary the length of the OPO and therefore the CEO-frequency. Amp, amplifier; LPF, low-pass filter; SSG, synthesized signal generator.

The CEO-frequency remained locked for  $\sim 30$  minutes, and could remain locked for most of a day if the piezo-driver for PZT3 was used to keep the locking loop within its capture range as the temperature varied. Any loud noises, such as a door slamming were enough to make the locking drop. Loud voices or people walking in the room caused a visible increase in the noise of the CEO-frequency beat of the spectrum analyser, so enclosing each cavity in a Perspex box and floating the optical bench helped but did not fully isolate the system from vibrations.



### 3.2.3. Bandwidth measurement of the CEO-frequency locking loop

The broadening of the linewidth of the CEO-frequency to a finite width can be observed directly on an RF spectrum analyser. Observing the signal-to-noise ratio for this beat frequency and the -3 dB bandwidth on the analyser is therefore a convenient way to directly monitor the quality of the locking of the CEO-frequency.

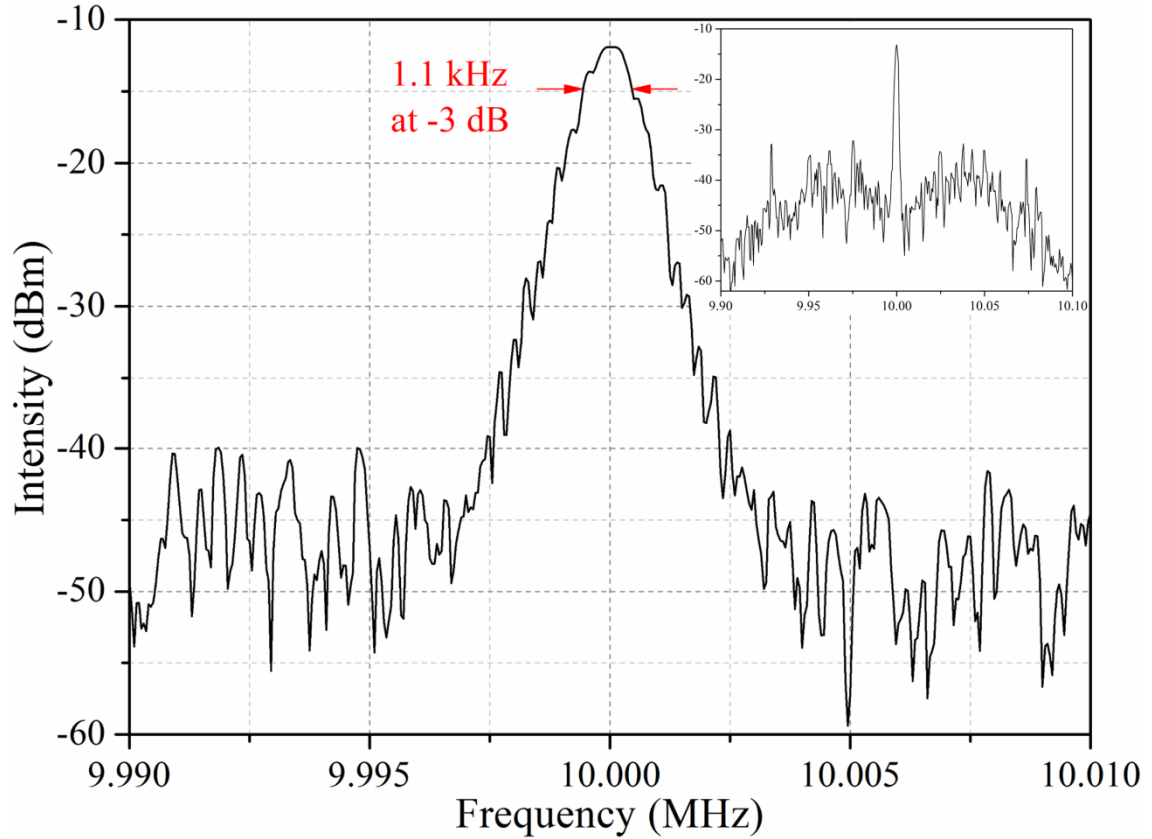


*Figure 3.12 RF spectrum of locked signal CEO-frequency recorded on an RF spectrum analyser (Agilent E4411B) with a span of 20 kHz (200 kHz inset). The -3 dB bandwidth was 1.1 kHz recorded with a resolution of 1 kHz (instrument limit). The signal-to-noise ratio was  $>30$  dB [44].*

Early measurements of the RF spectrum of the beat were made on an Agilent E4411B with a resolution limit of 1 kHz (see Figure 3.12). Measurements of the locked CEO-frequency on this analyser had a signal-to-noise ratio of  $>30$  dB and a -3 dB locked bandwidth of  $\sim 1$  kHz (instrument-limited) [44]. Results published by this group for earlier work using an  $f$ -2 $f$  pump self-referencing approach reported a broader linewidth for the stabilized CEO-frequency with a lower signal-to-noise ratio for the

locked CEO-frequency beat [36]. The improved results are likely to be as a result of the simplified locking technique implemented for this thesis.

Later on in this project a Rigol DSA 1030A with a resolution limit of 10 Hz was used to measure the locked beat, which gave a -3 dB locked bandwidth of 15 Hz [23]. These measurements were taken with the interference filter in the interferometer to separate the green beat from the rest of the light after the PBS. When the interference filter was removed and a reflection of the diffraction grating was used instead, the signal-to-noise ratio improved significantly, which led to a better -3 dB bandwidth measurement of  $\sim 10$  Hz (instrument-limited). The improved RF spectrum results are shown in Figure 3.13, whilst the repetition frequency of the Ti:sapphire laser was also locked; this may have led to a small increase in the noise for the CEO-frequency lock which cannot be observed at this resolution.

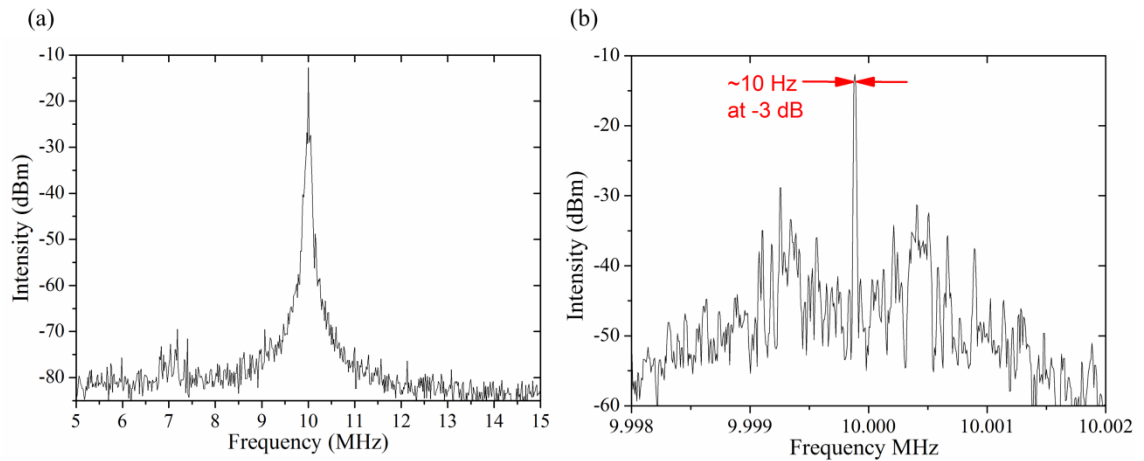


*Figure 3.13 RF spectrum of locked signal CEO-frequency recorded on an RF spectrum analyser (Rigol DSA 1030A). (a) Span of 5 MHz, resolution 3 kHz. The signal-to-noise ratio was  $\sim 50$  dB. (b) Span of 5 kHz, resolution 10 Hz. The -3 dB bandwidth was 10 Hz (instrument limited). The repetition frequency of the Ti:sapphire laser was also locked for these measurements.*

Figure 3.13 shows a very narrow bandwidth for the CEO-frequency lock, significantly better than that shown for other comparable near-IR frequency combs such as a Cr:forsterite laser at  $1.25 \mu\text{m}$  (CEO-frequency bandwidth  $\sim 1$  MHz) [20], and an Er-doped fibre laser at  $1.53 \mu\text{m}$  (CEO-frequency bandwidth  $\sim 600$  kHz) [21]. Narrower bandwidths can be achieved using strongly-driven laser diodes and phase-lead compensation control, where sub-Hz bandwidths have been achieved [22], but this requires more complex feedback systems.

#### ***3.2.4. Phase noise in the CEO-frequency locking loop***

The in-loop phase noise PSD and cumulative phase noise were calculated for the CEO-frequency locking loop. Whilst the CEO-frequency was locked, part of the signal from the PFD circuit was directed through a separate amplifier and into a 12-bit data acquisition card, with the data capture controlled with a Matlab program. The amplifier before the card ensured the dynamic range was filled, although this will have contributed some additional noise; the minimum phase noise possible to record with no input to the amplifier was measured as 4 mrad (integrated over the full frequency range). Data were recorded for a range of time periods, however periods of 1 second have been used consistently through this thesis for easy comparison between results. The output from the PFD circuit recorded with the acquisition card was calibrated in phase to calculate the phase error between the CEO-frequency and the 10 MHz reference so the frequencies with the highest noise contribution could be identified. An experiment was carried out to calibrate the voltage from the PFD circuit as a phase. Two frequency sources with a common reference were set at ~10 MHz, offset from each other by 1 Hz. With these as the two inputs to the PFD circuit, the output was monitored whilst it moved from its minimum to its maximum voltage. The time period and voltage range for this gave a slope in V/rad which was used to change the voltages recorded in noise measurements into a phase in radians. The recorded signals were also adjusted for the amplification and offset of the amplifier before the data acquisition card. The results for the noise measurements are presented in Figure 3.14 [44].

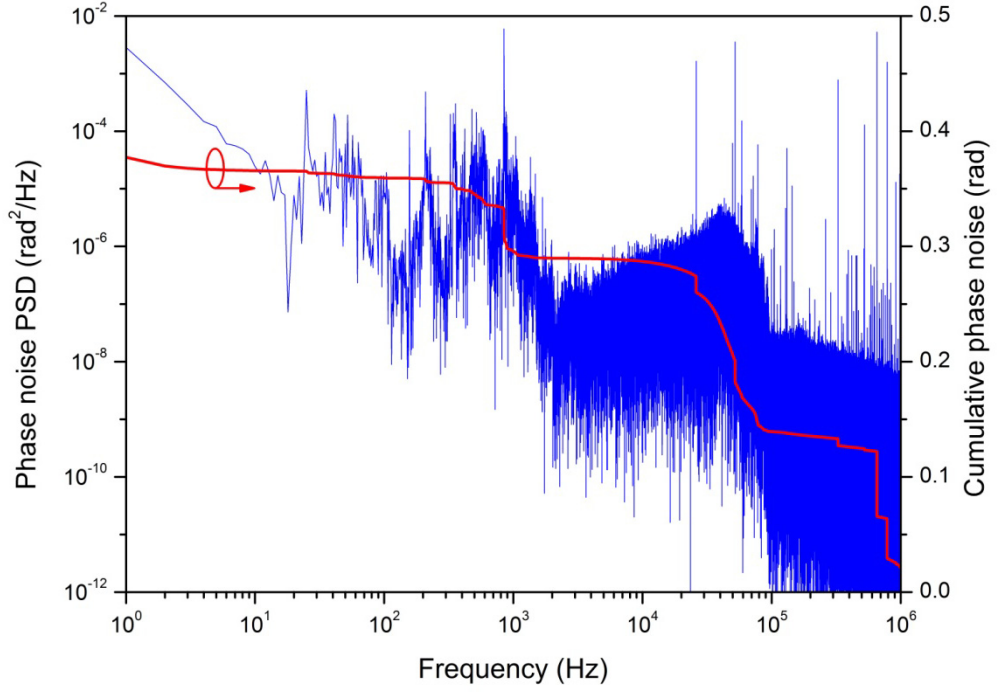


*Figure 3.14 In-loop measurement of the phase noise PSD of the CEO-frequency (blue). The cumulative phase noise (red) integrated up to 1 MHz is 0.38 rad (1 second observation time).*

The cumulative phase noise was integrated up to 1 MHz, which gave an error of 0.38 rad over an observation time of 1 second. Results previously published by this group for work using an f-2f pump self-referencing approach reported a cumulative phase noise up to 100 kHz for an observation time of 1 second of 3.5 rad [10]. Direct comparisons with these previous results are difficult as a number of changes have been made within the system, however the approach described here has achieved an order-of-magnitude reduction in the cumulative phase noise compared to the earlier work [10], which is most likely due to the simplification of the locking technique. This is especially impressive given the move from a Verdi pump laser for the previous results to a Millennia laser for the current project, as the intensity from the Millennia laser is less stable [44]. This difference is detailed below.

The data in Figure 3.14 show increased phase noise for PSD measurements between 3 and 60 kHz, compared to the previously published work. The increase in noise at these frequencies is attributed to the use of a multi-longitudinal-mode (MLM) Spectra-Physics Millennia VI in the current study, in contrast to the single-longitudinal-mode (SLM) Coherent Verdi V10 that was used in all prior work. MLM oscillation causes mode competition and beating effects in the laser which will increase the RIN of the

pump laser output and also – through nonlinear effects – couple directly to CEO-frequency phase noise in the modelocked oscillator [129]. This increased noise has been published for a comparison of the RIN from Millennia and Verdi lasers [130], which revealed a higher RIN from the Millennia laser in the 20 Hz - 1 MHz band. The increase is consistent with the higher phase noise PSD contributed across the 3 - 100 kHz band of the OPO CEO-frequency. The Ti:sapphire laser used to pump the OPO was not CEO-frequency stabilized, so there are no phase noise PSD data for the pump laser to allow an estimate for the relative performances of the OPO and the Ti:sapphire laser.

### ***3.2.5. Relative intensity noise***

Measurements of the RIN for the Ti:sapphire laser and the OPO were taken whilst the CEO-frequency of the signal pulses was locked. The repetition frequency of the Ti:sapphire laser remained free-running. Part of the outputs from the laser and OPO were monitored simultaneously on Si and InGaAs PDs (respectively) with the data collected using a 12-bit data acquisition card, as with the phase noise measurements. The average power for the final locked frequency comb must be stable for the ease of measurements for future experiments, such as spectroscopy. The RIN from the oscillators will also couple into the phase noise for the comb lines, so this will place a limit on the stability (comb line width and drift) for the final comb. Measurements were also taken for the Millennia pump laser to show how much of the Ti:sapphire RIN was caused directly by the Millennia. The data were recorded over a 64 second time period.

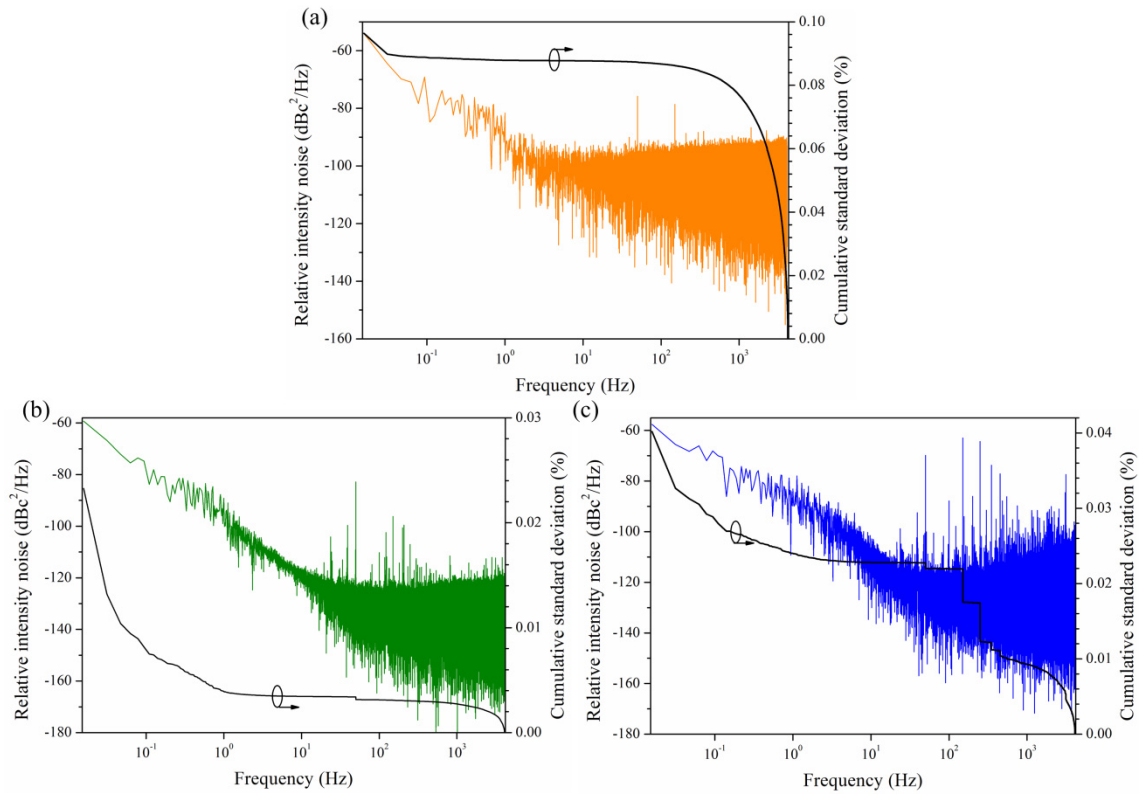


Figure 3.15 Relative intensity noise from the Millennia laser, Ti:sapphire laser and the OPO when the CEO-frequency of the signal was locked. The left axis shows the frequency-dependent RIN relative to the carrier, expressed on a logarithmic scale. The right axis is the cumulative standard deviation of the RIN data, calculated by normalising the laser power to unity then evaluating the standard deviation over an interval from a given frequency to the Nyquist frequency. (a) Millennia laser. (b) Ti:sapphire laser. (c) OPO. For the OPO signal output, the maximum value of the cumulative standard deviation is 0.04% and is equal to the RMS fluctuations of the normalised OPO power over the 64 second measurement interval.

The results in Figure 3.15(a) show almost all the RIN for the Millennia occurring at frequencies over 100 Hz, most likely due to the mode competition and beating effects considered in Section 3.2.4 that result from MLM oscillation in the laser. The noise at sub-Hz frequencies may be as a result of temperature drifts. The RIN for the Ti:sapphire laser follows a very similar pattern, but the OPO shows additional frequencies where significant noise is contributed. This may be due to amplitude noise in the Ti:sapphire laser leading to phase noise that couples in the OPO RIN. The difference between the RIN recorded for the Ti:sapphire laser and OPO is shown in Figure 3.16. Some of the phase noise will also have been contributed by the PFD circuit.

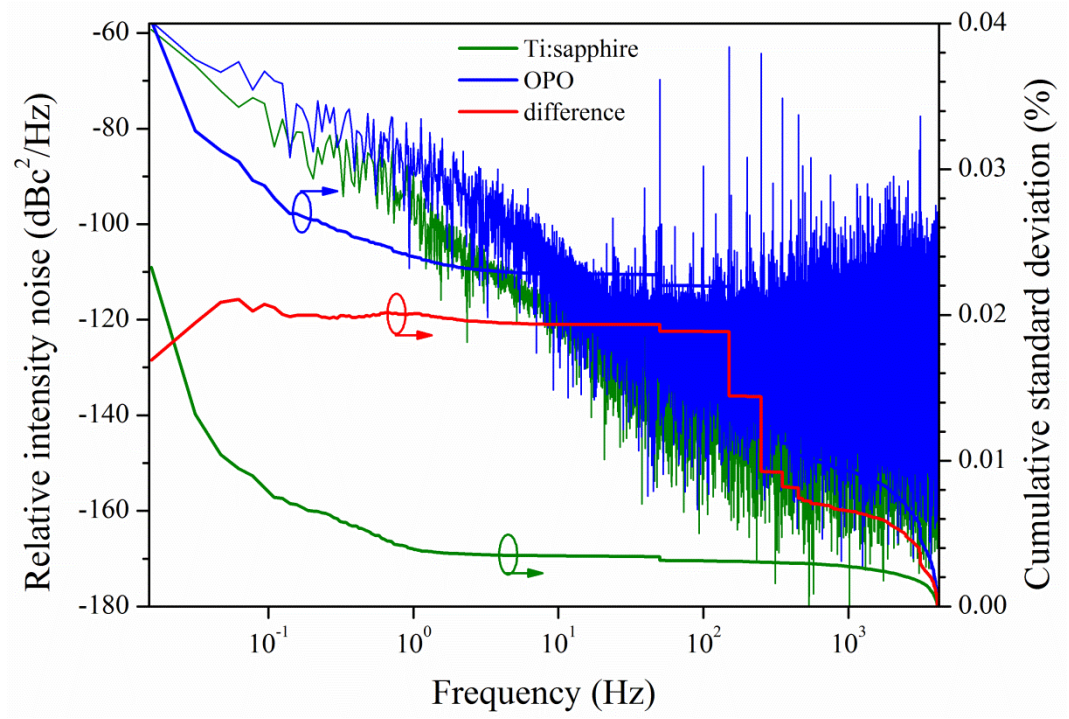


Figure 3.16 The decrease in the difference between the cumulative power error of the Ti:sapphire and OPO oscillators at low frequencies is as a result of the PZT for locking the CEO-frequency correcting for any fluctuations.

In Figure 3.16, the OPO shows additional RIN in the 100 Hz - 4 kHz frequency range and this noise may be traceable to the Millennia laser RIN in the following way. The fluctuations in the Millennia power couple into both the amplitude and phase noise in the Ti:sapphire through linear and nonlinear effects in the Ti:sapphire crystal. The amplitude noise will be observed in the RIN of the Ti:sapphire laser and will couple proportionately into the RIN for the OPO. Phase noise is not measured in the Ti:sapphire RIN, but will lead to timing jitter in the Ti:sapphire pulse sequence. This timing jitter causes amplitude noise in the OPO output which is observable as excess RIN. Despite these effects, the RIN from the OPO was very low with 0.04% cumulative standard deviation (relative to the carrier), compared to a Ti:sapphire laser RIN of approximately 0.02% cumulative standard deviation. The Millennia RIN was significantly higher at 0.09%.

### 3.3. Locking the repetition frequency of the Ti:sapphire laser

Some of the depleted pump in the OPO leaked through mirror M4 in the OPO cavity. Two glass slides were placed after this mirror in the depleted pump to direct part of this leakage light into two fast Si PDs (Hamamatsu S9055). The signal from the first of these, PD1, was used in the feedback loop for locking the repetition frequency of the Ti:sapphire laser. The second photodiode (PD2) was used to separately monitor the system repetition frequency without affecting the signal strength used in the feedback loop, and later as the source for two-sample frequency deviation and in-loop comb instability measurements.

The 8<sup>th</sup> harmonic of repetition frequency ( $\sim 2.24$  GHz) was used for locking ( $f_{rep}(\text{meas})$  in Figure 3.17), as this gave us increased sensitivity for changes in the frequency (i.e. a 1 Hz change would be detected as an 8 Hz change), although it also reduces the dynamic range [2]. The PD output passed through a 2.2 GHz band-pass filter (M-C VBFZ-2130-S+) to remove the other harmonics of the repetition frequency before entering a mixer (M-C ZAM-42). An Agilent E4411B synthesized signal generator (SSG1) with its output set to  $\sim 2.2414$  GHz ( $f_{rep}(\text{ref})$ ) was used as the other mixer input, the output of which was passed through a PI amplifier (Newport LB1005). The corner frequency, low frequency gain limit and gain were varied to obtain the quietest lock for the repetition frequency ( $f_{\text{corner}} = 100$  Hz, LF gain limit = 70 dB). The output from the PI amplifier fed directly into PZT1 (Thorlabs AE0505D08F), the piezo-electric transducer upon which a GTI mirror was mounted in the Ti:sapphire laser cavity. The PZT was bonded onto a large brass weight, which was then held in a mirror mount. This helped damp the vibrations from the PZT to minimise noise. The repetition rate remained locked for up to 1 hour with no adjustment of SSG1,  $f_{rep}(\text{ref})$ .



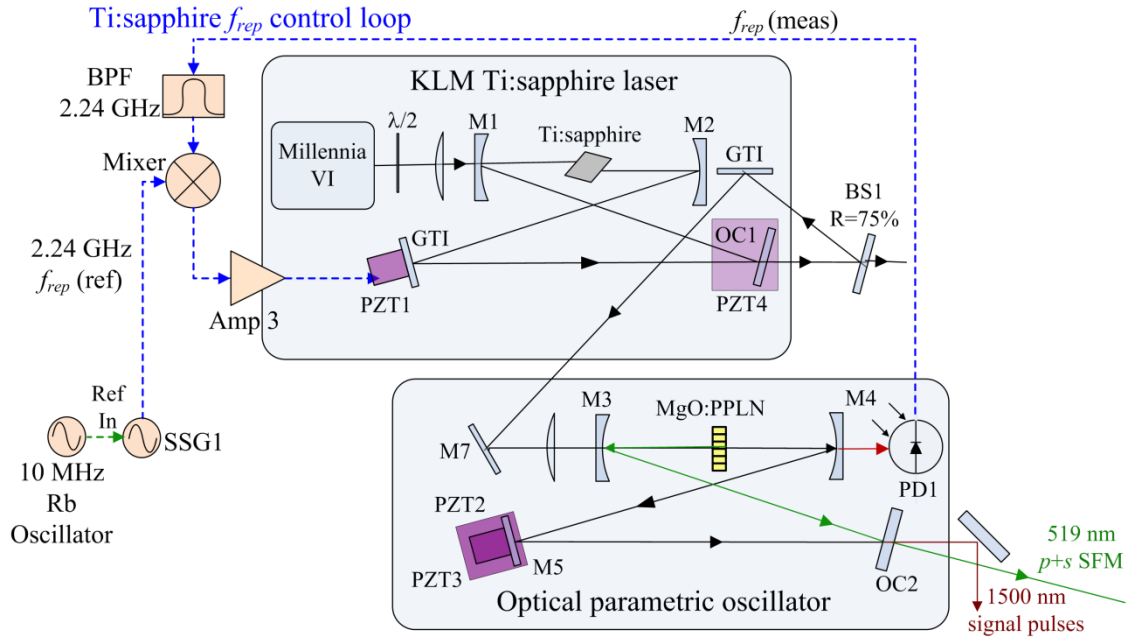
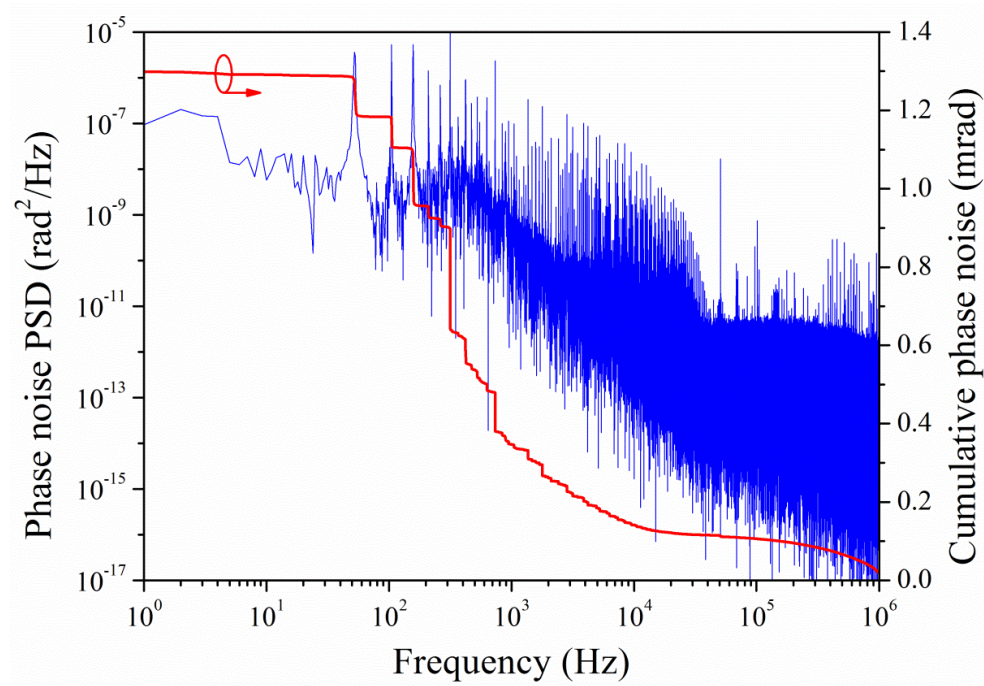


Figure 3.17 Experimental configuration for the stabilisation of the repetition frequency. The frequency measured at PD1 ( $f_{rep}(meas)$ ) was band-pass filtered to provide one input to a mixer, with SSG1 providing the second input ( $f_{rep}(ref)$ ). The output of the mixer was shaped using a PI amplifier to give feedback to PZT1. Amp, PI amplifier; BPF, band-pass filter; SSG, synthesized signal generator.

### 3.3.1. Phase noise for preliminary locking of the repetition frequency

An initial experiment for locking the repetition frequency had used a different PZT (Physik Instrumente P-820.10) with a cut-down GTI ( $\sim 8 \times 8 \times 2$  mm) mounted on it for the laser. When the repetition frequency was locked with these components, even when optimised ( $f_{corner} = 300$  Hz, LF gain limit = 20 dB) it was difficult to lock the CEO-frequency of the signal in the OPO. Phase noise PSD measurements were taken for the signal from the mixer using the same method described in Section 3.2.4. These were also calibrated to change the voltage into a phase. The peak-to-peak voltage for the sine wave from the mixer was measured when the difference between the inputs was a few Hz. The voltage level from the mixer when the repetition frequency was locked was also measured, so the slope at this point could be calculated (in V/rad). This factor, along with the amplitude and offset of the amplifier used to fill the dynamic range of the acquisition card, was used to calibrate the measured signal as a phase in radians. The results are plotted in Figure 3.18 with the cumulative phase noise. Similar in-loop phase noise measurements for no signal in the repetition frequency noise measurement were recorded, as were previously carried out for the CEO-frequency. This found the

minimum noise that could be measured (limited by the amplifier and acquisition card used for the measurement) was 0.06 mrad.



*Figure 3.18 In-loop measurement for the phase noise PSD over a 1 second observation time. The phase noise PSD for the repetition frequency is shown for the 8th harmonic, and the integrated data are scaled appropriately to show the cumulative phase noise in the fundamental for the repetition frequency. The cumulative phase noise from 1 Hz to 2 MHz is 1.3 mrad.*

The cumulative phase noise is low at 1.3 mrad, but there is considerable noise contribution for frequencies above 1 kHz, which will impact more strongly on the CEO-frequency lock than lower frequencies, which the faster loop will be able to adjust for.

### **3.3.2. Phase noise for improved locking of the repetition frequency**

To decrease the noise coupled from the repetition frequency stabilisation onto the CEO-frequency lock, the higher frequency components from the repetition frequency stabilisation loop needed to be reduced. This can be done electronically, but the best results are usually achieved by mechanically by “slowing-down” the PZT response so the faster CEO-frequency loop has time to correct to any fluctuations in phase.

A Michelson interferometer, with the Millennia laser as a source, was built using the original set-up (a cut-down mirror on a narrow PZT from Physik Instrumente) and then an alternative arrangement (un-cut 1 inch GTI mirror mounted on Thorlabs PZT with a larger end-surface area) to see if the frequency response and any mechanical instabilities causing noise were reduced. For a fixed voltage sine wave dither on the original PZT, increasing the frequency from 10 Hz to 1.2 kHz caused low frequency modulations on the fringes detected at a Si PD and did not lead to a decrease in fringe number (the corner frequency for the configuration was not approached). When the heavier arrangement with the wider PZT was used, the number of fringes detected halved for the higher frequency and no low frequency modulation was observed on the fringes. To further reduce any mechanical vibrations, the PZT was glued to a brass weight, which was held in the mirror mount. The original experiment used a small aluminium disc for this, which would have had little effect in damping any vibrations or resonances.

The improved phase noise measurements for the new arrangement are shown in Figure 3.19, the PI amplifier settings used were those stated at the start of Section 3.3. The cumulative phase noise was reduced from 1.3 to 0.98 mrad.

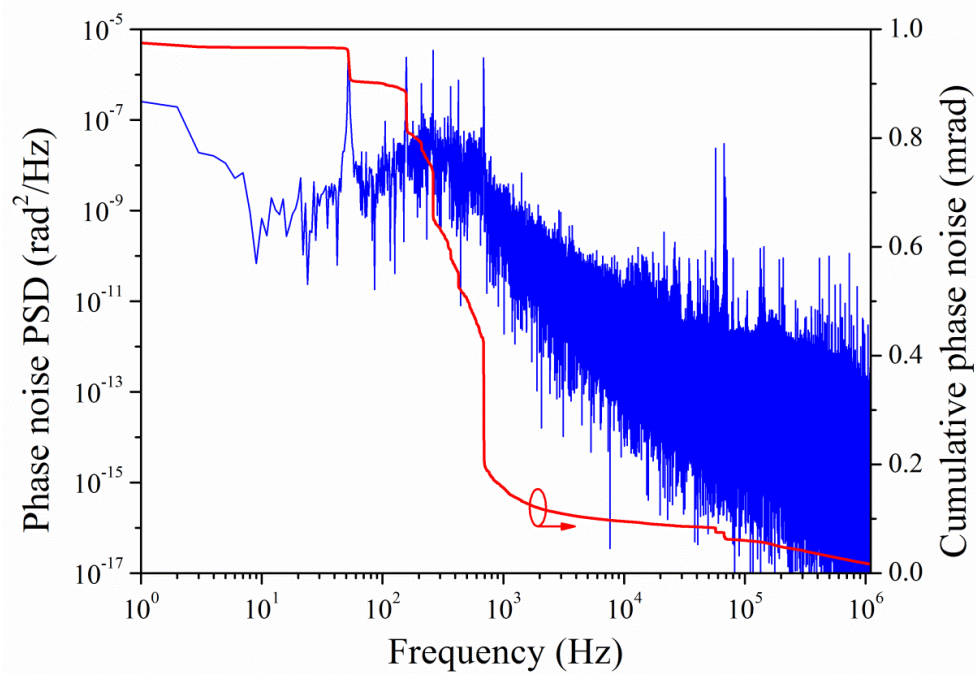


*Figure 3.19 In-loop measurement for the PSD phase noise over a 1 second observation time. The phase noise PSD for the repetition frequency is shown for the 8th harmonic, and the integrated data are scaled appropriately to show the cumulative phase noise in the fundamental for the repetition frequency. The cumulative phase noise from 1 Hz to 2 MHz is 0.98 mrad [23].*

In addition to a lower cumulative phase noise, the results in Figure 3.19 show less noise contribution from higher frequencies. There was, however, still a significant contribution between 100 Hz (the corner frequency on the PI amplifier) and 1 kHz (close to the measured corner frequency for the PZT and mirror), which will couple into the phase noise for the CEO-frequency when both the locking loops are stabilised.

### 3.4. Locking the OPO frequency comb

Both the CEO-frequency and the repetition frequency of the OPO signal pulses need to be stabilised to generate a fully stabilised frequency comb. Here I describe the locking performance when both the repetition frequency and the CEO-frequency are stabilised.

#### 3.4.1. Locking both the CEO-frequency and repetition frequency

Once the optimum PI amplifier settings for both the CEO-frequency loop and the repetition frequency loop were established, both needed to be locked simultaneously to determine the overall instability in the frequency comb lines [23].

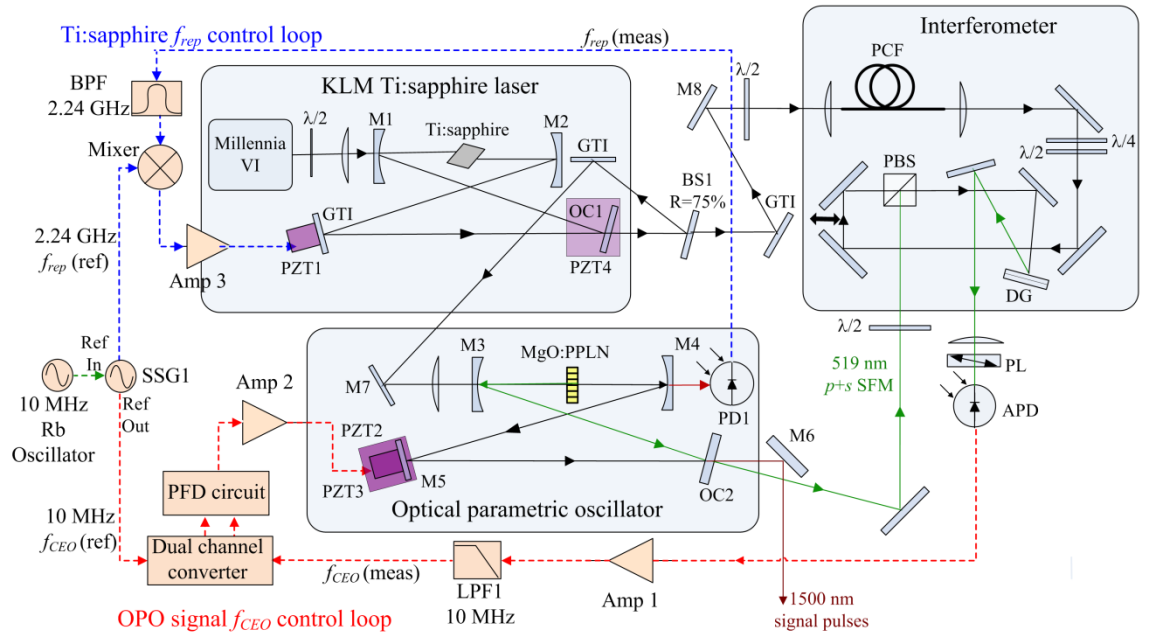


Figure 3.20 Experimental configuration for a locked frequency comb for the signal pulses from a synchronously pumped femtosecond optical parametric oscillator.

Once the repetition frequency of the Ti:sapphire laser was locked, the CEO-frequency of the signal from the OPO could be stabilised for the same periods as with the

repetition frequency free-running. The time limits arose from temperature drift in the laboratory, although the CEO-frequency was also sensitive to any strong vibrations and noises.

### 3.4.2. Power spectral density of the phase noise in the frequency comb

Measurements of the phase noise PSD and the cumulative phase noise for locking the CEO-frequency were repeated for the repetition frequency free-running and locked in the same manner described earlier. This allowed an estimate to be made for the contribution of the CEO-frequency to the comb line stability, and also conclusions to be drawn over the degree of cross-talk between the two locking loops. The configuration used meant the repetition frequency lock was not affected by simultaneously controlling of the CEO-frequency.

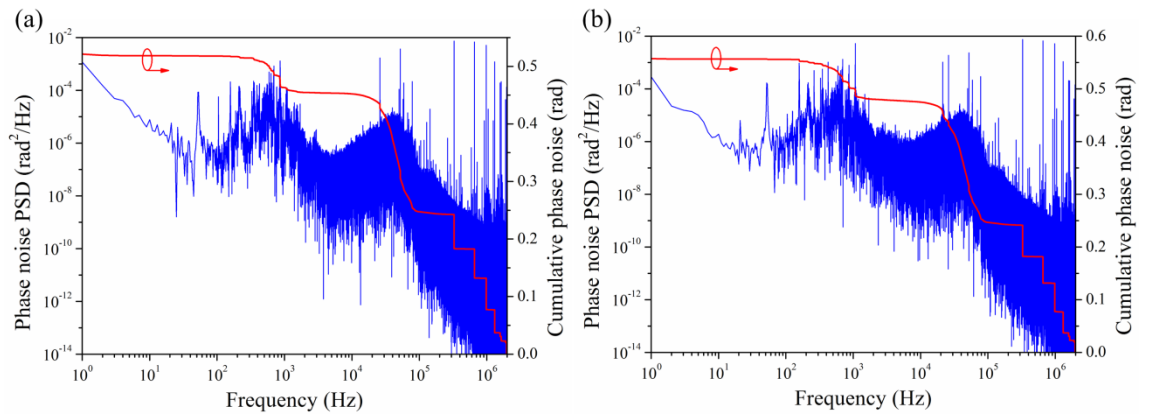


*Figure 3.21 In-loop measurement for the phase noise PSD and cumulative phase noise of the CEO-frequency. (a) With the repetition frequency free-running the cumulative phase noise was 0.52 rad. (b) With the repetition frequency locked the cumulative phase noise was calculated as 0.56 rad [23].*

The CEO-frequency cumulative phase noise was 0.52 rad with the repetition frequency free-running (see Figure 3.21(a)). This cumulative noise is higher than the measurements made earlier in the project, which gave a cumulative phase noise of 0.38 rad. Some changes were made to the system during this time, including changing the chiller unit used to cool the Millennia and Ti:sapphire crystal; any of these changes, or even the decrease in performance from the Millennia laser or the PCF due to degradation with time may have caused the increased noise.

The locked CEO-frequency had a cumulative phase noise of 0.56 rad when the repetition frequency was also locked. This shows that the repetition frequency stabilisation loop did not significantly reduce the quality of the CEO-frequency lock. These results were taken at the same time as the repetition frequency noise measurements in Section 3.3. The results in Figure 3.21(b) indicate an increase in the phase noise of the CEO-frequency around 1 kHz, where the majority of the phase noise had been found to contribute to the repetition frequency loop.

The cumulative phase noise integrated from 1 Hz to 2 MHz for the repetition frequency was 0.98 mrad, which corresponds to 0.16 mHz. For the CEO-frequency, the cumulative phase noise corresponds to an uncertainty of 0.09 Hz. If we take our centre optical frequency,  $f_n$ , to be  $\sim 200$  THz, this would give a mode number,  $n$ , of  $\sim 714300$  for a repetition frequency of 280 MHz. Multiplying up the phase noise for the repetition frequency implies a contribution from our feedback electronics to the uncertainty in the comb line position of 110 Hz and indicates the CEO-frequency phase noise contribution is negligible in comparison [23]. This value is an upper limit for the comb line instability as it includes contributions from the phase noise measurement system and has been calculated from the error signals in our locking loops rather than the CEO- and repetition frequencies directly.

### ***3.4.3. Two-sample frequency deviation and in-loop comb instability measurements***

Another method of analysing phase noise involves time-series frequency-stability measurements (based on the Allan deviation) which can help characterize the effectiveness of our servo-control system and its contribution to the overall comb instability. A frequency counter was used to record the variation in the repetition frequency and the CEO-frequency while locked over a range of gate times, from which we calculated the two-sample frequency deviation of these signals (Allan deviation calculated about the lock frequency).

A Rb reference (Spectratime LCR900/10 MHz) was used to stabilize a synthesized signal generator (SSG1) which in turn was used to stabilize a second signal generator, SSG2 (Anritsu MS9740A), and a frequency counter (Hameg Programmable Counter HM8123), as shown in Figure 3.23. The Rb clock had a long term fractional stability of  $< 2 \times 10^{-11}$  / day and a short term stability of  $9 \times 10^{-13}$  for a time period of 100 seconds [131, 132]. Measurements were taken over periods of  $\sim 15$  min with gate times varying



from  $\tau = 1$  second to 10 seconds, and a sampling interval of  $T = \tau + 1$  second (so there was 1 second of dead-time between each measurement).

The CEO-frequency signal was recorded after the first low-pass filter (LPF1) but before the converter (see Figure 3.22(a)). To count the repetition frequency, the signal from PD2 (usually used for monitoring the frequency separately from the locking loop) was passed through LPF2 to remove any other harmonics of the repetition frequency and to provide one input to a frequency mixer. The other input to the mixer was from SSG2, the frequency of which was offset from the repetition frequency by 20 kHz. This meant that the lower frequency heterodyne output from the mixer, rather than the repetition frequency directly, was measured, so the counter could record to a higher resolution (see Figure 3.22(b)).

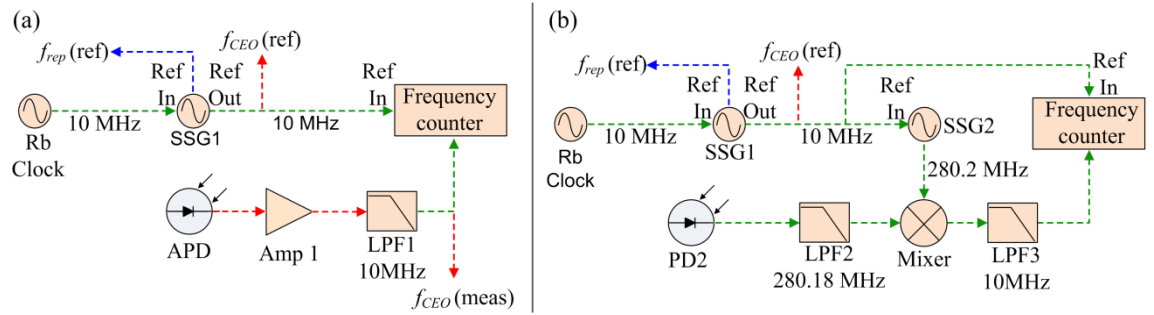


Figure 3.22 Configurations for recording frequency data on a counter for two-sample frequency deviation calculations. (a) Direct measurement of fluctuations in the OPO signal CEO-frequency. (b) Measurement of fluctuations in the Ti:sapphire repetition frequency by the heterodyne technique. SSG, synthesized signal generator; APD, avalanche photodiode; PD, photodiode; LPF, low-pass filter; Amp, amplifier.

The system noise associated with the monitoring electronics and Rb clock,  $f_{elec}$ , was measured by replacing the repetition frequency signal from PD2 with SSG1 set equal to this frequency and recording the frequency fluctuations over the same gate times (with SSG2 still offset by 20 kHz). These measurements were repeated with SSG1 set to 10 MHz and SSG2 set to this frequency with an offset 2 kHz, which gave very similar results to the  $f_{elec}$  measurement, with fractional instabilities slightly larger than those for the Rb clock. These near identical results suggested one system measurement,  $f_{elec}$ , was sufficient to estimate the noise contribution from the measurement electronics.

The system measurements were then repeated using a second Rb clock to reference the frequency counter (and to provide one input to the mixer at 10 MHz), replacing SSG1

and SSG2 in Figure 3.22(b), with the first clock in place of PD2 and the LPF. This allowed the Rb clock to be characterized by an out-of-loop measurement with an equivalent characterization to that used for the electronic system. The results were nearly identical to the initial measurements, indicating that our results were limited by the stability of the Rb clock [23].

Figure 3.23 presents time-series data for the CEO and repetition frequencies for a 1 second gate time. The results for the CEO-frequency show an instability about the 10 MHz frequency lock with a standard deviation of 0.17 Hz, comparable to the value of 0.09 Hz inferred from the PSD phase noise measurements. The repetition frequency measurements showed lower instabilities, with a standard deviation of 6.0 mHz, compared to 6.7 mHz for the system,  $f_{elec}$ , implying the stability measurement of the repetition frequency was limited by the measurement equipment used [23].

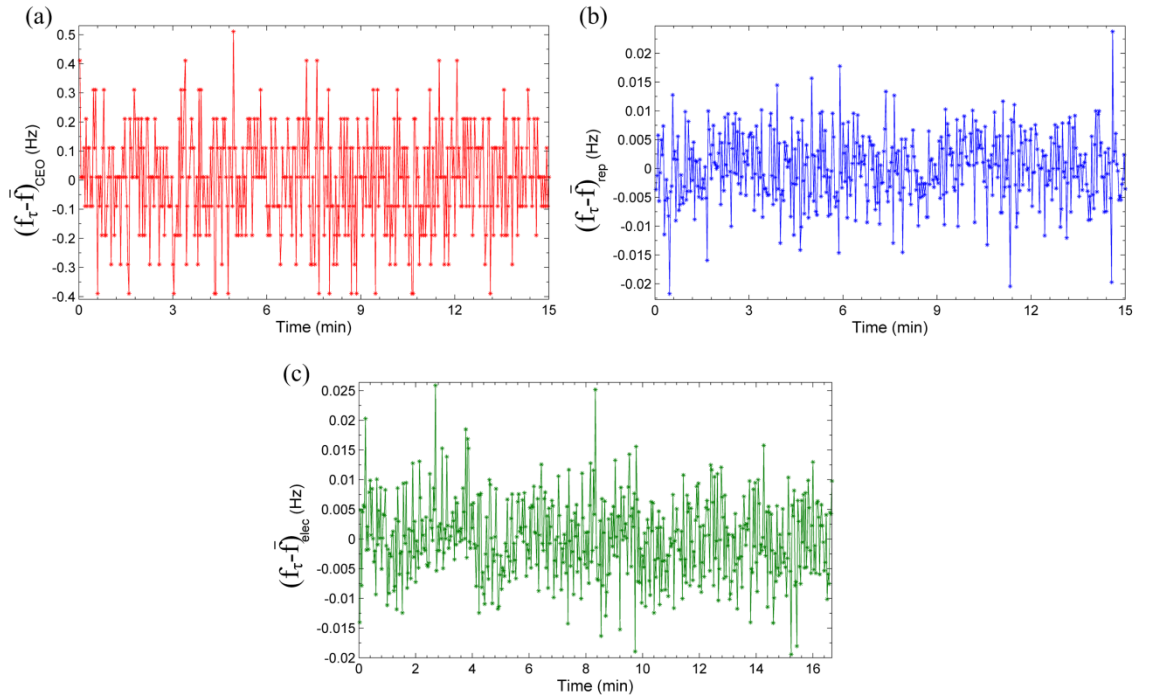


*Figure 3.23 Frequency fluctuations recorded on a frequency counter with 1 s gate time. (a) In-loop measurement of the CEO-frequency beat showing fluctuations about the 10 MHz lock (the mean was subtracted during data processing). (b) In-loop measurement of the repetition frequency showing fluctuations about the 280.18 MHz lock. The repetition frequency was combined in a mixer with a reference (SSG2) offset by 20 kHz. (c) In-loop measurement of the electronic showing fluctuations about the 280.18 MHz reference frequency. The reference frequency (SSG1) was combined in a mixer with a second frequency source (SSG2) offset by 20 kHz.*



The two-sample frequency deviation for the CEO-frequency ( $\Delta f_{CEO}$ ), repetition rate ( $\Delta f_{rep}$ ) and electronic system ( $\Delta f_{elec}$ ) used for the repetition frequency stabilization were measured [133], using the Allan deviation equation, but relative to the zero point (see Figure 3.23). These were used to calculate the fractional instability [20], and plotted in Figure 3.24. The data for  $\tau = 100$  s were calculated by averaging the results for 10 s. The 1 second dead time in each sampling interval increased the instability calculated, so the results are worst-case values. The data for the Rb clock [132], are also plotted for comparison and show the overall stability limitation of the system. The two-sample frequency deviation for the CEO-frequency was calculated as 0.174 Hz and for the repetition frequency was 6.1 mHz, which were scaled to the optical domain by the mode number of 714285. This implied fractional stabilities of  $2 \times 10^{-11}$  (repetition frequency) and  $1 \times 10^{-15}$  (CEO-frequency), so as with the PSD phase noise, the repetition frequency dominates. These results are comparable with the  $2 \times 10^{-11}$  s instability of the Rb clock, verifying that servo-control of the CEO-frequency and repetition frequency was effective in stabilizing the comb to at least this level of precision.

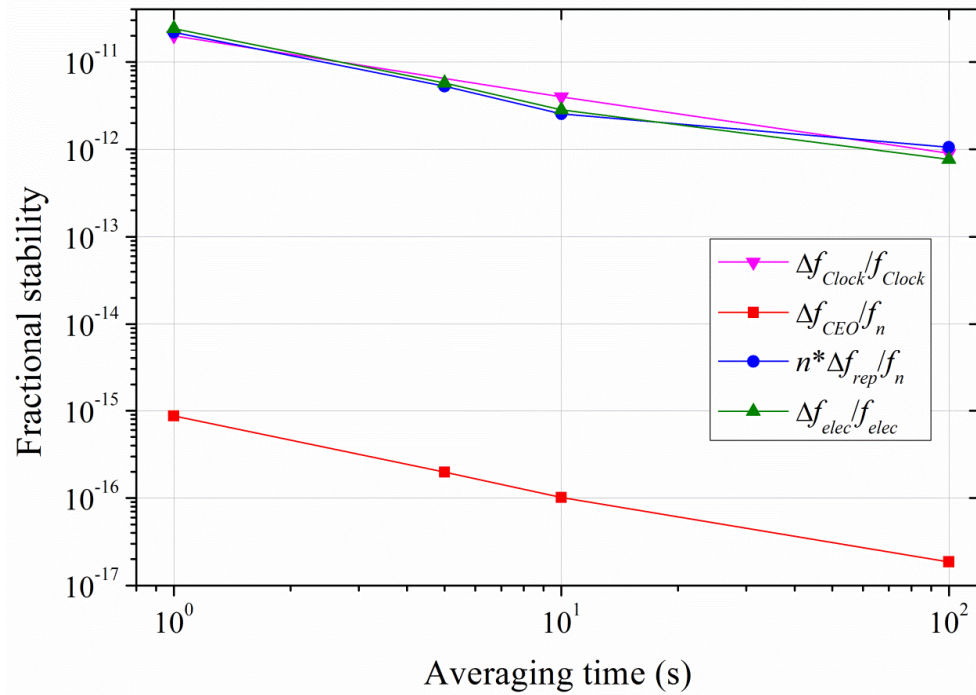


Figure 3.24 Fractional comb instability (frequency deviation scaled by optical frequency,  $f_n = 200$  THz and mode number,  $n = 714285$ ) from in-loop repetition frequency and CEO-frequency signals. Data for the electronic system ( $\Delta f_{elec}/f_{elec}$ ) and the Rb clock ( $\Delta f_{Clock}/f_{Clock}$ ) show the intrinsic uncertainty in the repetition frequency measurements.

#### ***3.4.4. Slow loop for long-term repetition frequency stabilization***

One of the limitations for the long-term locking of the frequency comb was the significant drift in temperatures experienced in the laser laboratory (occasionally several degrees Celsius over a day). This resulted in the locking loop for the repetition frequency running out of range over time periods varying from one to twelve hours, depending on the lab conditions. To compensate for this, a second, slower loop was implemented for maintaining the repetition frequency lock.

The signal from the PI amplifier (range 0 – 10 V) was monitored using an A-D data acquisition card (Labjack U6) connected to a computer controlled with a Matlab program. This monitored the voltage so if it varied from 5 V (centre of the locking range) a small voltage offset was added through a port on a Newport Microdrive Controller (ESA-C) to PZT4 (Thorlabs AE0505D08F), which was a piezo-electric stack mounted in a translation stage under the output coupler in the Ti:sapphire laser. The program changed the output to this at intervals of 0.1 seconds by very small voltage increments (mVs), so the repetition frequency lock loop was fast enough to compensate for this without any increase in the system noise. The Newport piezo-driver allowed the full voltage range for the PZT to be used (100 V), so that as long as no sudden shocks happened to the system, the fast locking loop could be kept within its 10 V range for a twelve hour period.

### **3.5. Conclusions**

The repetition frequency and CEO-frequency of signal pulses from a synchronously pumped femtosecond OPO were stabilised to obtain a locked frequency comb. The phase noise in the CEO-frequency lock was lower than previous systems from this group and compared well to other comparable comb sources. The removal of the f-2f self-referencing interferometer simplified the system and reduced the noise in the locking loop. The repetition frequency of the system was also stabilised without any significant effects on the CEO-frequency. RIN measurements, PSD and cumulative phase noise calculations, in addition to fractional stabilities were examined to fully characterise the frequency comb and confirm its suitability for high-accuracy applications.

In Chapter 4 a different optical system is introduced as a potential optical frequency reference for this frequency comb. This was based on a 780 nm external cavity diode laser stabilised using saturated absorption in rubidium vapour.

In Chapter 5 I describe how the OPO frequency comb detailed in this chapter was filtered using a passive external cavity to increase the comb line separation to improve the suitability of the locked comb for spectroscopy measurements.

## **Chapter 4. Locking the frequency of an external cavity diode laser using saturated absorption in Rubidium**

### **4.1. Introduction**

For an absolute frequency measurement to be taken with a frequency comb, an absolute RF or optical reference is needed for stabilising the comb. In the previous chapter, noise measurements were examined for an OPO frequency comb and a 10 MHz Rb clock was used as the reference for all the electronic frequency sources in the experimental setup. This reference could be further standardised by using a 10 MHz GPS signal to ensure the clock's frequency follows an internationally recognised reference. However, for an absolute reference, something must be used that can be independently implemented anywhere and not only where there is a GPS signal. In this chapter I describe how an external cavity diode laser (ECDL) was locked to a frequency peak resulting from saturated absorption in a Rb gas cell. This resulted in a stabilised optical source, with a wavelength corresponding to the second harmonic wavelength of the signal pulses from the OPO.

The initial experimental work for setting up the ECDL for showing saturated absorption in Rb was carried out by Alireza Marandi when he visited the Ultrafast Optics Group and was completed by Jan Heip for his 5<sup>th</sup> year undergraduate project. The final optical setup and locking of the ECDL to one of the Rb transmission peaks was carried out by the author with assistance from Tobias Lamour and Xiaohui Fang. Useful advice and assistance was also provided by Aidan Arnold from the University of Strathclyde [134].

#### **4.1.1. Rubidium**

Rubidium (Rb) is an alkali metal with one stable isotope,  $^{85}\text{Rb}$ . This makes up about 72% of the naturally occurring element, with  $^{87}\text{Rb}$  composing the remainder [135]. The quartz reference cell (Thorlabs GC19075-RB) used in this research contained Rb in the natural isotope ratio. Rb is easily vaporised and its spectral absorption range renders it highly suited to high-precision applications. One example of this is in secondary frequency references, such as the clock used for referencing the electronic equipment discussed in Chapter 3.

Light at 780 nm which is transmitted through a Rb reference cell will show four Doppler broadened peaks, corresponding to the transition  $5^2S_{1/2}$  to  $5^2P_{3/2}$  [136]. These peaks are from two sets of transitions for each of the two isotopes. The peaks are for the Doppler broadening of the  $D_2$  transition peak and result from movement of the Rb vapour atoms with a thermal velocity distribution. If a Rb atom is travelling towards an observer with velocity  $v_a$ , then the frequency at which the transition actually occurs,  $f$ , can be calculated from the frequency at which it is observed,  $f_a$ , using [137]:

$$f_a = f \left(1 - \frac{v_a}{c}\right)^{-1} \quad \text{Equation 4.1}$$

where  $c$  is the speed of light. The Maxwell velocity distribution gives a spread in  $v_a$  resulting in the Doppler line broadening [137]:

$$\Delta f = \frac{f}{c} \left(\frac{2kT \ln 2}{m}\right)^{1/2} \quad \text{Equation 4.2}$$

where  $m$  is the mass of the atom and  $\Delta f$  is larger than the natural linewidth. The broadening is inhomogeneous and gives a Gaussian line shape [137].

The beam emitted directly from a laser can be considered as a probe beam, passing through the gas cell onto a PD to give the Doppler broadened peaks when the laser optical frequency is tuned. If a beamsplitter is used to reflect part of this beam back directly along its incident path, this now becomes a pump beam. We now have two beams of equal frequency propagating through the gas cell in opposite directions. This means the two beams interact with atoms with similar speeds moving in opposite directions. If the laser is tuned to the zero velocity transition frequency then both beams will interact with the same set of atoms (a “crossover” frequency), reducing the absorption of the probe beam at a point along the Doppler broadened peak. This corresponds to the zero velocity atoms, i.e. the actual frequency of the transition,  $f$ . The absorption of the pump beam (at a crossover frequency) reduces the available atoms for excitement by the probe beam, so as the troughs (Lamb dips) in intensity corresponding to absorption by zero frequency atoms increase in height, the Doppler broadened peaks are reduced in intensity [137]. The Lamb dips in the broadened peaks (or peaks in the broadened troughs in the case of a transmission spectrum) are much narrower and therefore more suitable as a reference for locking. Theoretically they are only limited in linewidth by the Heisenberg uncertainty principle; however in reality they are limited by the linewidth of the laser [137, 138]. By using two beams, sub-Doppler saturated absorption troughs (Lamb dips) can be generated. This reveals the hyperfine transitions

in the  $D_2$  lines. Diagrams showing the hyperfine structure for absorption in Rb are shown in Figure 4.1.

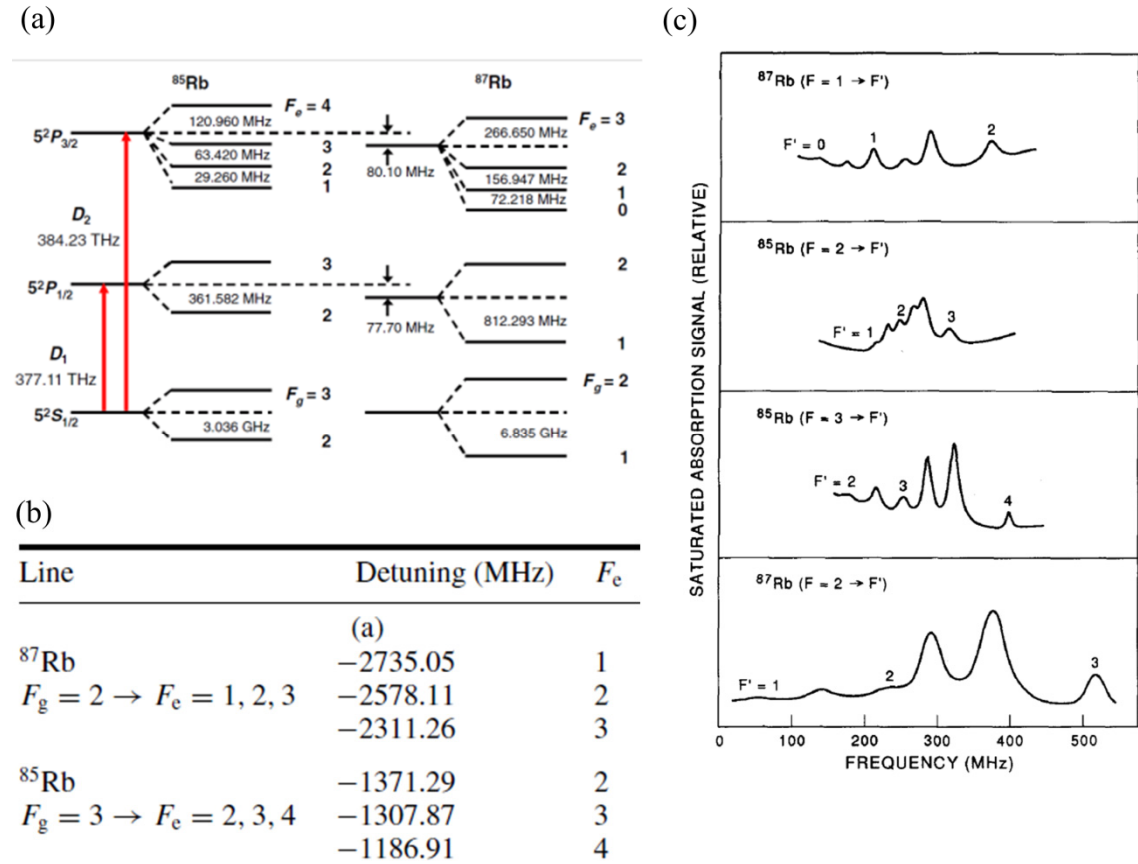


Figure 4.1(a) A schematic taken from [136] showing the hyperfine structure for the  $D$  spectroscopic lines of Rb. (b) Part of a table taken from [136] displaying the transition frequencies for the  $D_2$  line relative to the weighted average. (c) Figure taken from [139] showing the saturated absorption curves for the hyperfine structure of Rb.

In the absence of hyperfine splitting, the average frequency for the  $D_2$  transition can be calculated by the abundance of isotope as 384 230 436.6 MHz. All the hyperfine peaks will be offset from this by the detuning frequencies presented in Figure 4.1(b). Two of these peaks, the  $^{87}\text{Rb}$  excitation from the  $F=2$  ground state and  $^{85}\text{Rb}$  excitation from the  $F=3$  ground state, were used to dither lock an external cavity diode laser (ECDL).

#### 4.1.2. External cavity diode lasers

A semiconductor diode laser can have one end anti-reflection coated so an external optical element(s) completes the cavity. The increased length of the cavity can reduce the phase noise and therefore the linewidth of the emitted light. The use of a diffraction grating as the output coupler can also reduce the linewidth and allow for wavelength tuning [140]. This technique for laser control was first used with dye lasers [141].

An external cavity diode laser (ECDL) can be arranged in a Littrow or Littman-Metcalf configuration. In the Littrow configuration, with a collimating lens and diffraction grating [142], the first-order diffracted beam provides the feedback to the laser diode, and by making small changes to the angle of the grating, the wavelength of the laser can be tuned. This is achieved by ensuring the Littrow condition (Equation 4.3) is satisfied:

$$2D \sin\theta = m\lambda \quad \text{Equation 4.3}$$

where  $D$  is the line-spacing on the diffraction grating,  $m$  is the order of diffraction,  $\theta$  is the angle between the  $m^{\text{th}}$  order of diffraction and the normal to the grating and  $\lambda$  is the wavelength of the light. So  $m$  will be equal to 1.

This configuration can be designed so that only one mode will see gain, enforcing single-mode operation. Adjusting the angle of the grating to tune the wavelength will, however, slightly change the direction of the output beam [141], although this can be compensated for [143].

The other design that can be used is the Littman-Metcalf configuration [144]. For this arrangement the diffraction grating remains stationary, and an additional mirror is used to reflect the first-order diffracted beam back into the laser diode. The reflected zero-order diffracted beam is lost in this configuration so the output power is lower than with a Littrow design, and the addition of a mirror into the cavity reduces the simplicity of the design. A Littrow configuration was used for the ECDL in the research for this thesis.

#### 4.1.3. Dither locking of an optical cavity

The ECDL was locked to the  $^{87}\text{Rb}$   $\text{D}_2$  transition at frequency,  $f_{\text{lock}}$ . The laser wavelength was stabilised using dither locking, which is a common method for controlling cavity length [145], or frequency [134].

When dither locking is used to stabilise a passive cavity, a signal with a clear peak is needed to derive an error signal. If, for example, the length of an optical cavity needs to be stabilised to give the highest intensity output, as the length moves away from its optimum, the light intensity output will fall. Applying a modulation, or dither, to the cavity length, with a known amplitude, phase and frequency, will produce a Gaussian or other similar response function for a measurement of intensity against displacement. The peak intensity will occur at the optimum length, and drop as the cavity length increases or decreases. If the derivative of this signal is taken, it will equal zero at the cavity length where the intensity is highest (see Figure 4.2).

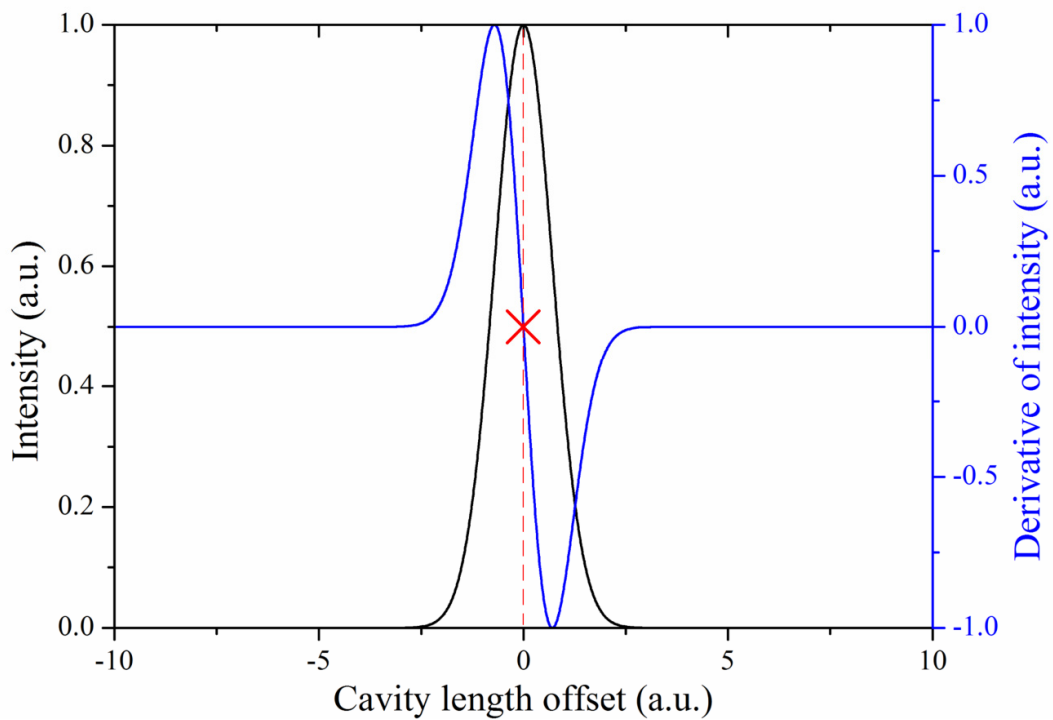


*Figure 4.2 Intensity from a cavity is plotted against the offset from optimum length. The derivative of the intensity signal is plotted in blue. The red dashed line marks the length at which the intensity is highest and the red cross marks the point where the derivative of the intensity crosses this line.*

Once the cavity length is brought within the locking range of a feedback loop, locking to zero for the derivative will always coincide with the maximum for the output intensity (red cross in Figure 4.2), even when the maximum level fluctuates. The locking range will be limited by the amplitude of the dither signal. The dither signal needs to be at the minimum possible voltage to minimise the fluctuation in intensity.



For the ECDL, an absorption peak in Rb was used for dither locking. The diffraction grating angle was tuned onto this peak, so the feedback loop locked onto its maximum.

To find the intensity peak shown in Figure 4.2, a higher amplitude signal with a significantly lower frequency is usually applied to the same component that is being dithered. This ensures the peak used for locking can be easily resolved, and in the case of the ECDL, allows a sufficiently large frequency range to be examined to ensure the correct peak is selected for locking. Once a peak has been identified, the low frequency modulation is reduced in amplitude, until a lock is established, when the additional modulation can be removed entirely to minimise the noise in the locking loop. However, there will always be a small fluctuation in the intensity for any peak used for locking in this way, as the dither must be constantly applied to maintain the lock.

## **4.2. Experimental configuration**

### **4.2.1. Optical design**

A Thorlabs LD1255R laser diode driver, powered by a low noise power supply, was used to power the semiconductor laser diode. The current was adjustable and monitored by the voltage across a  $10\ \Omega$  resistor. Two capacitors ( $200\ \mu\text{F}$  tantalum and  $100\ \text{nF}$  ceramic) were placed in parallel across the laser diode to reduce any fluctuations in the current. The laser diode ( $100\ \text{mW}$ , AR-coated) had an emission peak at  $780\ \text{nm}$  when in normal operation, so within range of the  $\text{D}_2$  line of Rubidium at approximately  $780.2463\ \text{nm}$  [146]. It was mounted in one side of a  $90^\circ$  kinematic mount with an  $1800\ \text{lines/mm}$  visible diffraction grating mounted at  $\sim 45^\circ$ . This could then be rotated slightly to reach the Littrow condition at  $44.6^\circ$  (see Equation 4.3) to form an ECDL. The output from the laser diode was collimated and it was orientated to align its linear polarisation direction (parallel to the minor axis of the elliptical beam) in the vertical axis. This is parallel to the lines of the grating to maximise the wavelength tunability [147]. The kinematic mount was mounted onto silicone mats that enclosed a peltier, which was heated to control the laser emission spectrum (see Figure 4.3).

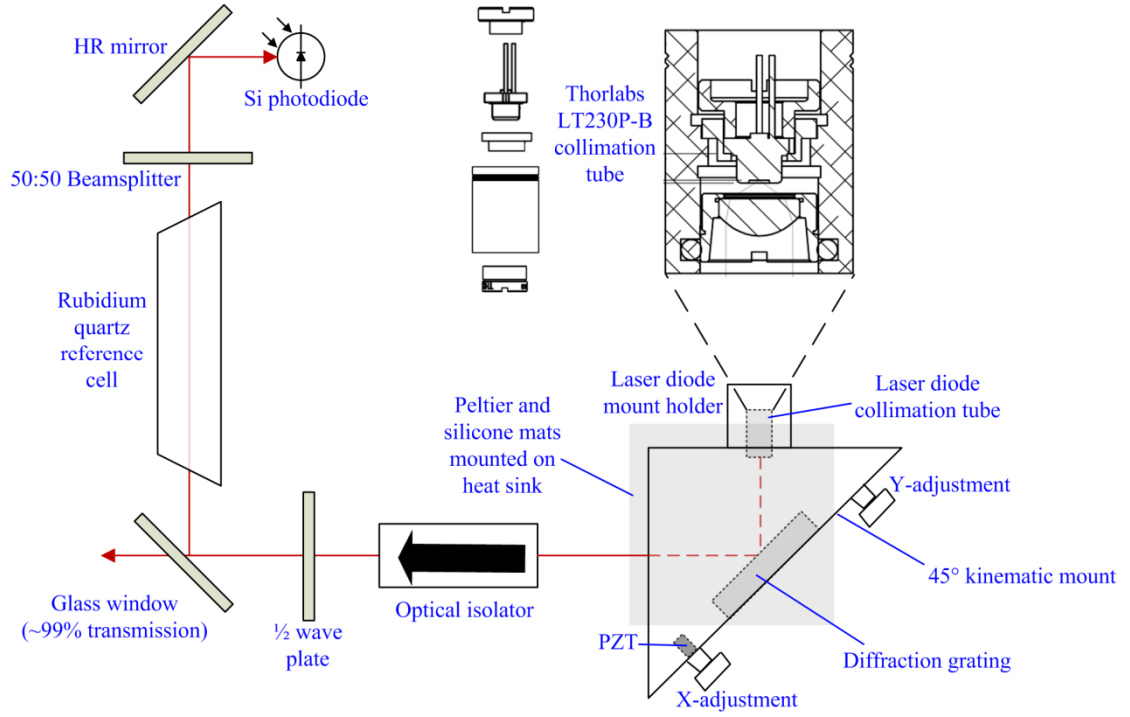


Figure 4.3 The optical configuration for locking the ECDL. The diffraction grating was attached, using an adhesive, to a 1 inch mount that fitted in the 45° kinematic mount. The transmission spectrum showing saturated absorption was recorded at the photodiode. The diagrams for the Thorlabs LT230P-B collimation tube were taken from [148].

The cavity length and temperature were optimised to give the smoothest tuning over the correct wavelength range (close to 780.24 nm) whilst maintaining a narrow linewidth. A PZT was mounted inside the ‘x-direction’ actuator on the mount to be used for scanning the grating and eventually for locking the cavity. A low-noise power supply (Tektronix PWS 4323) was used in series to add a positive voltage offset onto the PZT so the combined scanning and locking signals would never result in it receiving an overall negative voltage.

The output from the ECDL passed through a LINOS isolator and then a half-wave plate (on a rotation mount) that reduced the intensity of the light that would pass through the Rb gas cell (only a small amount of power can be used through the Rb vapour without saturating the signal at the PD). A glass window was used at 45° to reflect ~1% of the light into the gas cell. The rest of the light passed through the window to be recorded on a fibre-coupled OSA and, later, on an additional Si PD for normalisation in the locking RIN measurements. After the gas cell, a beamsplitter was used to reflect part of

the beam back along its path (so we had both a pump and a probe beam) and the remaining probe beam was reflected onto a negatively-biased PD.

The experimental configuration is also shown below in Figure 4.4(a) and the kinematic mount is shown in more detail in Figure 4.4(b). Once the alignment was completed a cardboard box was placed over the mount to help maintain a stable temperature for the laser diode.

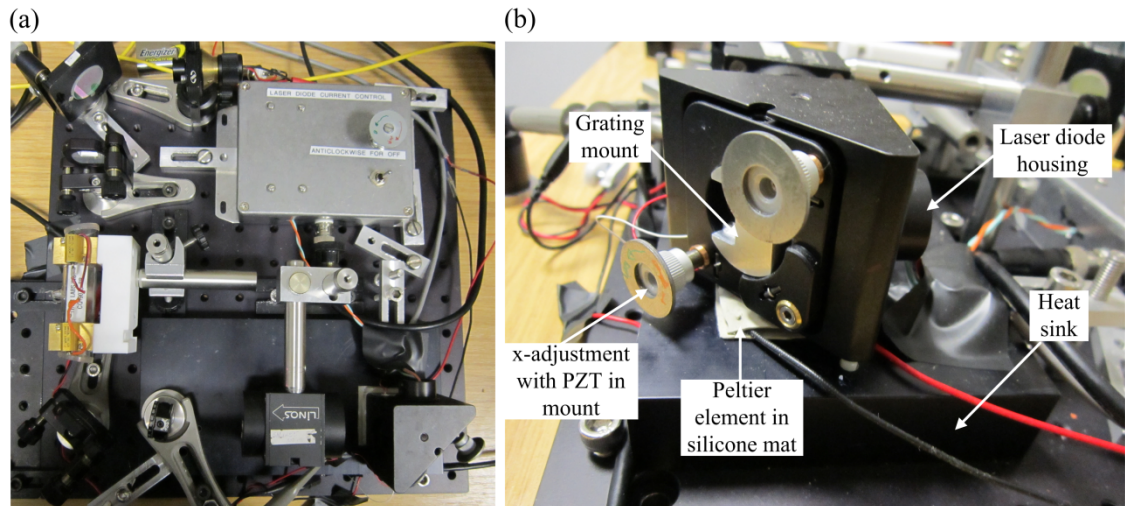


*Figure 4.4(a) Photograph of the optical layout. (b) Photograph of the kinematic mount used to tune and lock the ECDL.*

Operation as an ECDL was established by adjusting the angle of the diffraction grating. Once this was optimized, the grating was used to tune the wavelength of the ECDL to the Rb absorption peaks. Using a low frequency scan (6 Hz at a 9 V amplitude) on the PZT, the current of the laser diode was used to see absorption peaks and the beamsplitter was aligned to maximise the saturated absorption dips. These appeared as peaks on the transmission spectrum, see Figure 4.5.

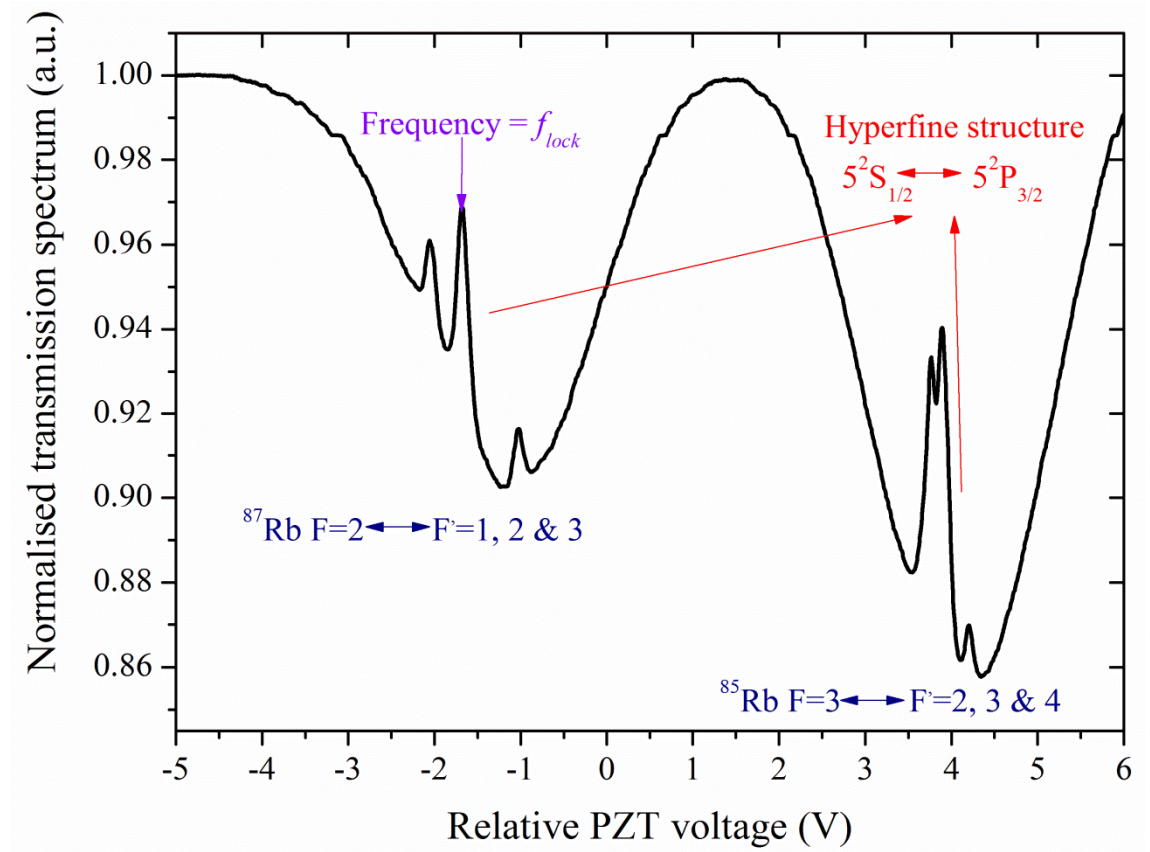


Figure 4.5 Saturated absorption seen as transmission peaks on the Doppler broadened dips in the spectrum detected at the photodiode. The strongest peak from  $^{87}\text{Rb}$ , ( $f_{\text{lock}}$ ) was used to lock the ECDL for the results given below. The ECDL was also successfully locked to the strongest transmission peak from  $^{85}\text{Rb}$ .

The peak used to lock the ECDL laser was for the  $^{87}\text{Rb}$   $F=2$  to  $F'=2$  transition and corresponded to an optical frequency,  $f_{\text{lock}}$ , of 384 227 981.9 MHz [146], and a wavelength of  $\sim 780.246$  nm.

#### 4.2.2. Locking electronics

A New Focus LB1005 Servo Controller was used as a proportional-integral amplifier (PI) amplifier for locking the ECDL. The triangular low frequency scan was used for the 'sweep in' signal and a 1.85 kHz, 160 mV amplitude sine wave from a low noise SRS lock-in amplifier (SR810 DSP) was used as a modulation signal into the PI amplifier. This was the dither signal used for locking. The modulation signal was also high-pass filtered and used as one input for a mixer. The photodiode signal was high-pass filtered and used as the other input for the mixer. The gains for the circuits

used as high-pass filters were adjusted to ensure the inputs to the mixer had equal intensities. The output of the mixer was the derivative of the PD signal, and this was low-pass filtered to remove the high frequency modulation. The filtered derivative was then used as the input of the PI amplifier ( $f_{\text{corner}} = 300$  Hz, LF gain limit = 20 dB), the output of which was finally used as the error signal to control the PZT for locking. The locking electronics are shown in Figure 4.6 below.

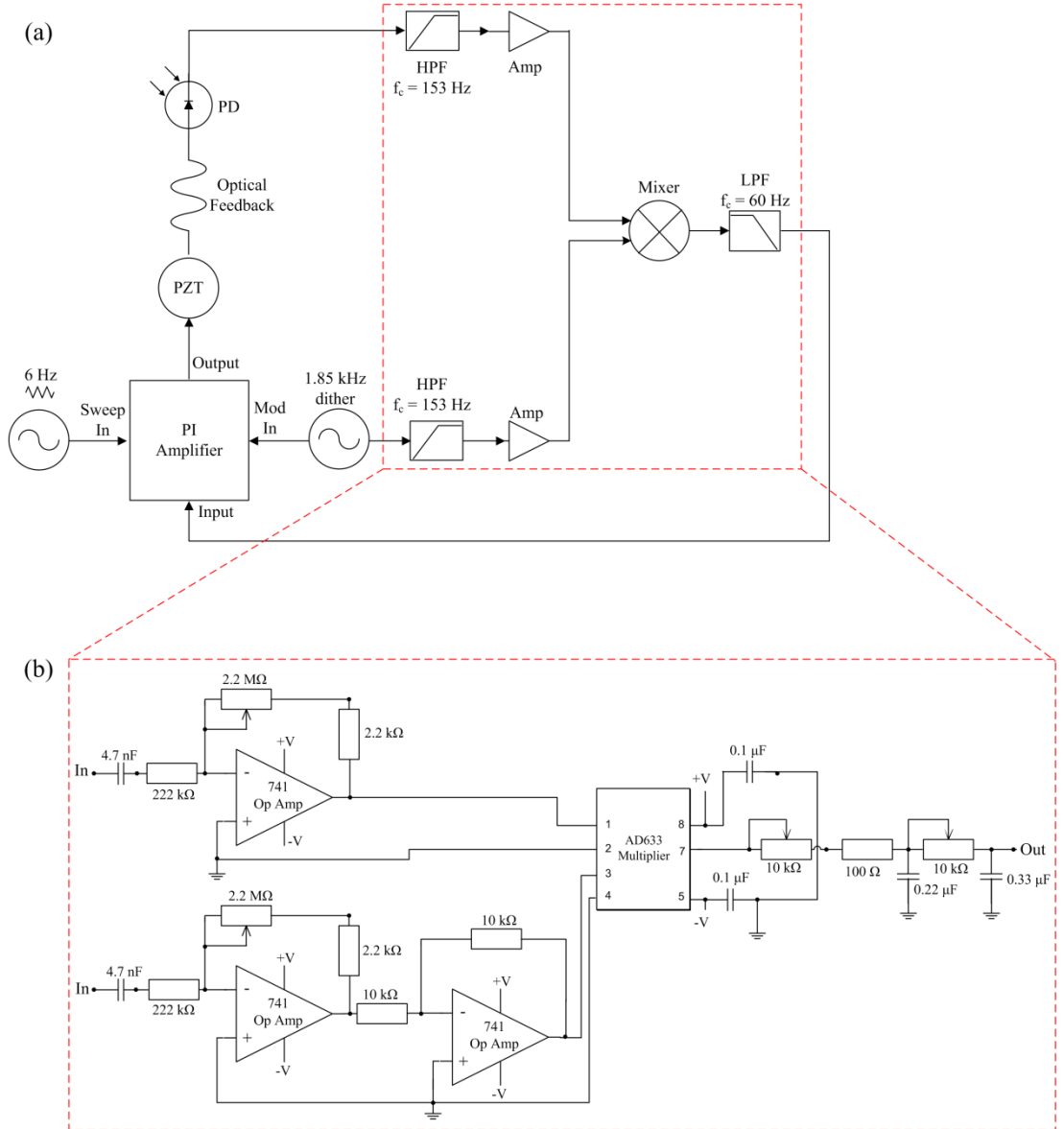
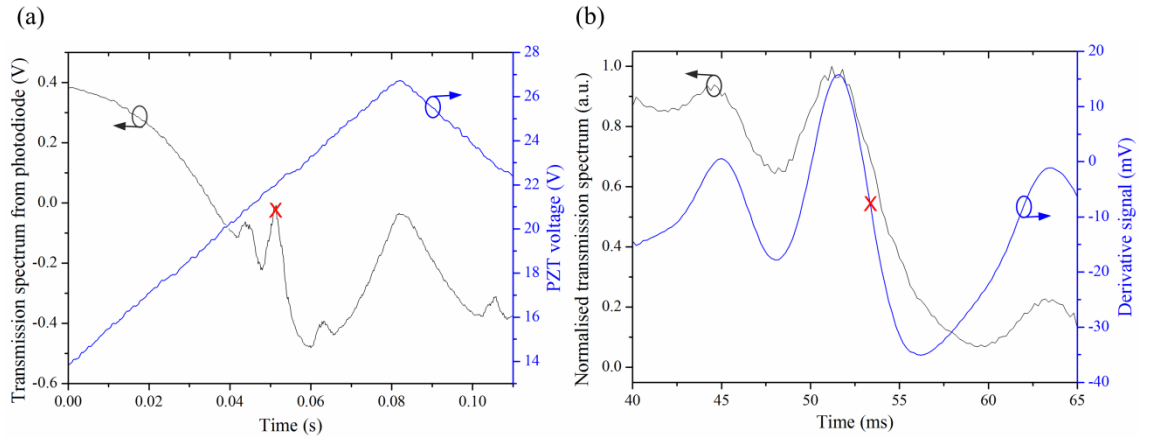


Figure 4.6(a) The feedback loop used to lock the ECDL to a Rb transmission peak. (b) The circuits built to filter, invert and amplify the two signals so the mixer inputs were matched in intensity and phase. HPF, high-pass filter; LPF, low-pass filter;  $f_c$ , corner frequency.

The scan on the PI amplifier was gradually turned down so only the peaks from  $^{87}\text{Rb}$  were visible. Then the offset from the low noise power supply was used to bring the strongest peak to the halfway point of the positive scan, see Figure 4.7(a). The scan continued to be turned down as the output offset on the PI amplifier was used to bring the derivative signal to the centre of the transmission peak, see Figure 4.7(b). There was a small phase offset in time observed here on the oscilloscope, resulting from some of the electronics used between where the two signals were monitored. This is not a real delay between the normalised transmission spectrum and the derivative from the mixer and will have no affect on the locking. When the scan was very small the PI amplifier was switched to ‘lock-on’ and the scan fully turned off. The ECDL was then stabilized to the saturated absorption (Lamb dip) peak.



*Figure 4.7(a) Transmission signal from saturated absorption shown with the modulated error signal from the PI amplifier with the scan on. The red cross marks the peak that was tuned to the centre of the upward slope of the scan. (b) The same transmission peak with the low pass filtered derivative signal from the mixer. The red cross on this marks the centre of the derivative signal.*

### 4.3. ECDL stabilisation results

#### 4.3.1. The locked ECDL

Once the ECDL was locked to the peak in the transmission, the scan could be turned back on while maintaining locking to ensure it remained locked to the correct peak. Locking was successfully demonstrated for over an hour. The main limiting factor for locking the ECDL was the air conditioning in the laboratory which caused large fluctuations in its temperature. Other aspects of the experimental configuration had an



effect on the noise level in the locking and these are explored in more detail in Section 4.3.2 below. Once the ECDL was locked, the modulation signal amplitude was turned down to 55 mV to minimise the noise in the locking signal. However when first establishing lock, or when locking was lost, it was easier to re-acquire this if the amplitude of the modulation signal was first increased back to  $\sim 160$  mV.

#### 4.3.2. Relative intensity noise measurements

RIN measurements have previously been described in Chapter 3. Here they were recorded from the PD on an Agilent Infiniium 54833A oscilloscope for time spans ranging from 1 to 100 seconds. A second PD in the beam transmitted through the glass window was recorded simultaneously and used to normalise the signal from the main PD for any fluctuations from the laser diode. The PSD for time spans of 1 and 100 seconds were taken to calculate the RIN and the cumulative standard deviation. These results are shown in Figure 4.8.

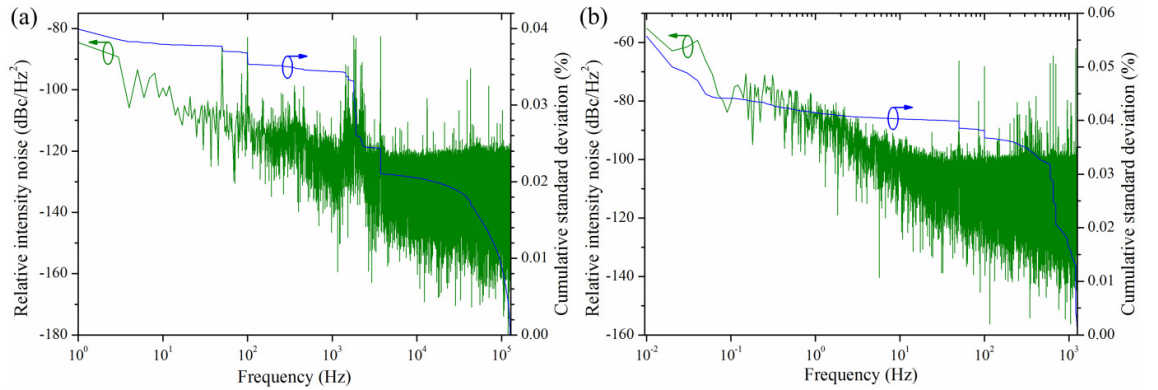


*Figure 4.8 RIN from the locked ECDL after the Rb reference cell. The left axis shows frequency-dependent RIN relative to the carrier (logarithmic scale). The right axis is the cumulative standard deviation of the RIN data, calculated by normalising the optical power to unity then evaluating the standard deviation over an interval from a given frequency to the Nyquist frequency. This is equal to the root-mean-square fluctuation of the normalized power over the measurement interval. (a) Results for a 1 second data acquisition. (b) Results for a 100 second data acquisition.*

For a 1 second data acquisition, noise at 50Hz and 100 Hz from the mains electricity and room lights can be observed. There is also noise at the modulation frequency of 1.85 kHz. The cumulative standard deviation was 0.040%. For the longer acquisition time, noise is also observed at these frequencies, in addition to higher frequencies approaching 1 kHz. The cumulative standard deviation over 100 s was 0.055%.

#### **4.4. Conclusions and further work**

The ECDL was successfully locked to a transmission peak resulting from saturated absorption in Rb. The locking had low noise and the ECDL could remain locked for relatively long periods of time without any external adjustments. The wavelength of the locked ECDL is close to that of the frequency doubled signal pulses from the OPO frequency comb, so this could be used for locking or stability measurements with the OPO comb.

##### ***4.4.1. Improvements***

The room air conditioning was a limiting factor for long-term locking of the ECDL. An immediate improvement could be made by using more suitable box for the kinematic mount holding the laser diode and diffraction grating with the heating element. An additional box around the entire optical setup would further stabilise the temperature and protect it from significant fluctuations from the air conditioning. By further shielding the PD from ambient light in the room the noise peak at 100 Hz could be greatly reduced. In addition, a similar optical design to that used could also be easily implemented with a smaller footprint to enable easier use of this system with other systems, such as the OPO frequency comb.

The noise in the locking could also be reduced by using shielded cable for all the connections for the PZT, laser diode and PD, reducing the noise observed at 50 Hz. Additional optimisation with the high and low pass filter corner frequencies and using a box to house the amplifier ‘home-built’ circuits, as has already been done for the filters and mixer, would further reduce noise in the locking loop.

In the future, we plan to have all the electronics used for dither locking incorporated onto a single circuit board using low noise components. This should significantly reduce the noise in the locking loop and ensure there is no phase offset between the peak of the absorption and its derivative.



#### ***4.4.2. Frequency comb measurement***

By measuring the beat between this locked laser with the second harmonic of the locked signal pulses from the OPO comb and examining the noise and bandwidth in this signal, the noise in these two systems could be characterised. Alternatively, the Rb stabilised ECDL could be used as an alternative reference for locking the frequency comb [149]. Some small adjustments would need to be made to the OPO comb to ensure the wavelengths overlapped sufficiently for a beat measurement to be made.

In the next chapter work will be discussed for ensuring the OPO frequency comb is suitable for practical spectroscopic measurements. A stabilised frequency comb has been filtered by an external cavity stabilised using the same dither locking method that has been described in this chapter.

## Chapter 5. Mode filtering of a stabilised frequency comb

In Chapter 3 the stabilisation of a synchronously pumped femtosecond OPO frequency comb to a standard reference was described. The longitudinal mode spacing of this frequency comb was 280 MHz. In this chapter, attempts to improve the suitability of this comb source to applications in spectroscopy are described, as an external cavity was used to increase the separation in frequency of the comb lines. Initial results are presented and further improvements discussed with the aim to developing a stable frequency comb with multiple GHz line spacing.

### 5.1. Mode filtering and external cavities

Stabilised frequency combs, including combs generated with OPOs, are increasing being utilised across a range of applications. For many of these applications a high repetition frequency is desirable [101, 102, 150, 151]. Any wavemeters used in measurements need a resolution higher than the repetition rate of the frequency comb [150], and the spectrometers used in astrophysics often cannot resolve the comb lines of sources with repetition frequencies in the 100's of MHz range [56, 151]. With careful design OPOs can be built at repetition frequencies of the order of 1 GHz [49, 101], but above this the engineering difficulties increase and simple designs using “off-the-shelf” components are no longer possible.

Jiang *et al.* have demonstrated using pump lasers and OPOs with different cavity lengths at exact ratios, maintaining synchronous-pumping, to achieve repetition frequencies up to 1 GHz [102, 106], and theoretically much higher; although pump powers sufficiently above threshold are required. Other groups have used external cavities, such as Fabry-Pérot etalons or interferometers, to increase the repetition frequency and enable the use of stabilised frequency combs in many areas [152], including molecular fingerprinting [16], and spectroscopy for astrophysics [56, 151, 153].

Ratios between comb sources and external cavities can also be used based on the same principles demonstrated by Jiang *et al.* so a vernier ratio, where every  $m^{th}$  mode from the laser frequency comb lines up with the  $n^{th}$  mode from the external cavity (where  $m \neq n$  are integers) is applied to increase the line spacing of the resulting frequency comb [154].

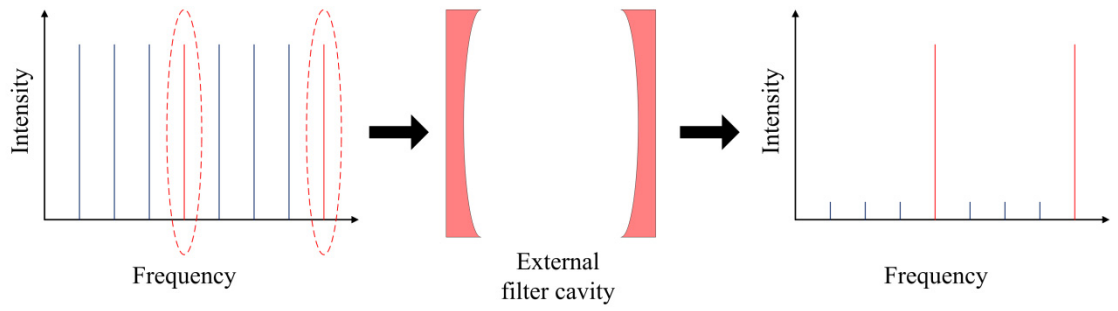


*Figure 5.1 Filtering of comb modes through the use of a passive external cavity. The FSR of the cavity is four times higher than the repetition frequency of the frequency comb, so the mode spacing of the comb transmitted from the filter cavity is four times larger.*

In Figure 5.1 a mode filtering external cavity is used to increase the frequency comb mode spacing. The length of the filter cavity can be locked at the exact harmonic so the intensity of the emitted comb is stable. If the dispersion within the cavity is near-zero, the width of the comb lines and phase noise for the frequency comb should not deteriorate.

## 5.2. Cavity locking techniques

If an external cavity is used to filter the modes of a frequency comb, the length of this cavity must be locked to a harmonic of the frequency comb to ensure synchronism, otherwise temperature drifts will reduce the transmission of the comb. There are a range of locking techniques that can be used to control the length of a cavity. Dither locking was described in Chapter 4, where it was used to control the optical frequency from an ECDL [155]. This is a more stable method than the simpler side-locking technique, where no modulation is used and the cavity is simply locked to the side of a peak at a fixed intensity, resulting in a noisier lock that will not hold for intensity fluctuations. The dither lock technique can be extended to Pound-Drever-Hall, where an additional cavity, such as a Fabry-Pérot can be used to generate a reflection to enable fast feedback for a large bandwidth [156]. Another technique that was considered was spatial mode interference, or tilt locking [157, 158]. In this case the external cavity would be slightly tilted so it was misaligned from the comb source to generate a non-resonant transverse mode that could be used to generate the error signal [56].

We selected dither locking for our stabilisation technique, as this method should be adequate for early experiments testing filtering of the OPO frequency comb, and the electronic circuits required were already available from the ECDL experiment detailed in Chapter 4.

### **5.3. Designing the filter cavity**

The external filter cavity was used to increase the mode separation of the stabilised OPO frequency comb. A range of cavity designs were considered, including using cavities with free spectral ranges (FSR) that were exact harmonics of the OPO repetition frequency, and cavities where a vernier ratio was used to increase the mode spacing to a higher harmonic. The plane and curved mirrors we had available in the lab that were HR coated around 1500 - 1550 nm were investigated to find the range of cavities that could be built as stable resonators [159, 160]. We also used the complex beam parameter to plot the beam propagation for the output of the OPO with a range of available lenses to ensure we could successfully mode-match the beam waist of the OPO and the beam waist for a cavity with one or more curved mirrors [92, 159]. An IR camera (Electrophysics MicronViewer 7290A) was used to measure the beam waist for the output from the OPO (Figure 5.2(a)), which was calculated in pixels before a calibration measurement (using an image taken of the millimetre scale on a ruler) was used to obtain a beam waist in microns. Once a cavity design and lens had been selected, this measurement was repeated after the OPO had propagated through the lens to confirm the beam propagation traced using Matlab (see Figure 5.2(b)).

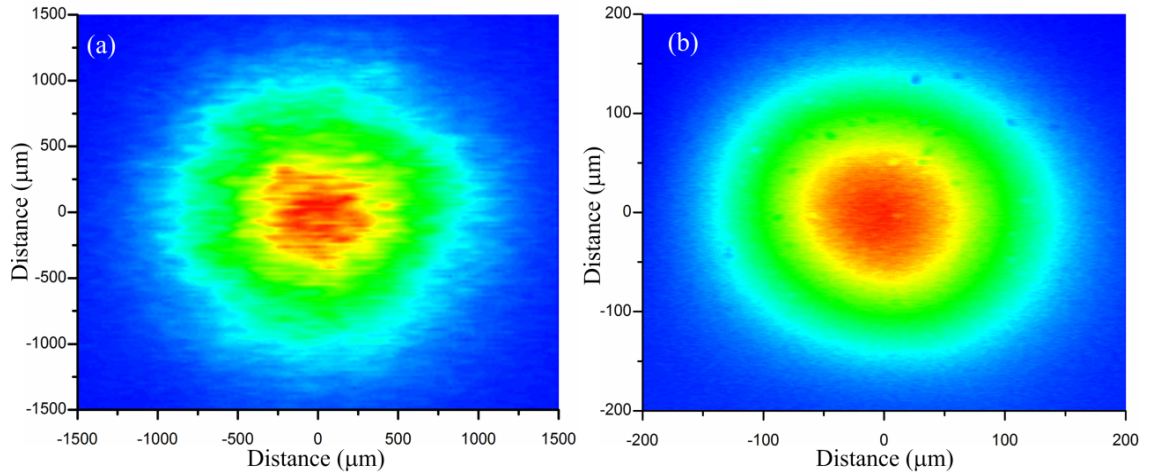


*Figure 5.2 Mode images for the OPO frequency comb recorded using an IR camera after the output coupler. (a) Image taken at distance corresponding to the focus of the 1.4 GHz filter cavity using no lens. Beam waist (radius) calculated as  $\sim 1.0$  mm in the horizontal axis and  $\sim 1.1$  mm in the vertical axis. (b) Mode image for the OPO beam after the 300 mm lens at a distance corresponding to the focus. Beam waist calculated as  $\sim 175$   $\mu\text{m}$  in the horizontal axis and  $\sim 178$   $\mu\text{m}$  in the vertical axis.*

Two cavity designs were selected from the results. Ultimately, we required the comb mode separation to be many GHz, and so a cavity with two curved mirrors ( $R = -38$  mm and  $R = -25$  mm) was selected using a 125 mm lens to focus in to obtain a beam waist radius of 77  $\mu\text{m}$ . This had a FSR of 8.7 GHz, corresponding to a mirror separation of  $\sim 17$  mm that would pass every 31<sup>st</sup> mode from the input comb. We were limited by the equipment available in our lab for measuring a comb at this repetition frequency, so we chose an additional longer cavity to test the locking procedure before we could continue to the final design. The cavity we have locked used one plane and one curved ( $R = -150$  mm) mirror and was used with a 300 mm lens to focus the OPO beam waist down to 180  $\mu\text{m}$ . This cavity had a FSR of 1.4 GHz, which corresponded to a mirror separation of 107 mm and passed every 5<sup>th</sup> mode from the input comb (see Figure 5.3). The mode image for the OPO beam after the 300 mm lens at its beam waist is shown in Figure 5.2(b).

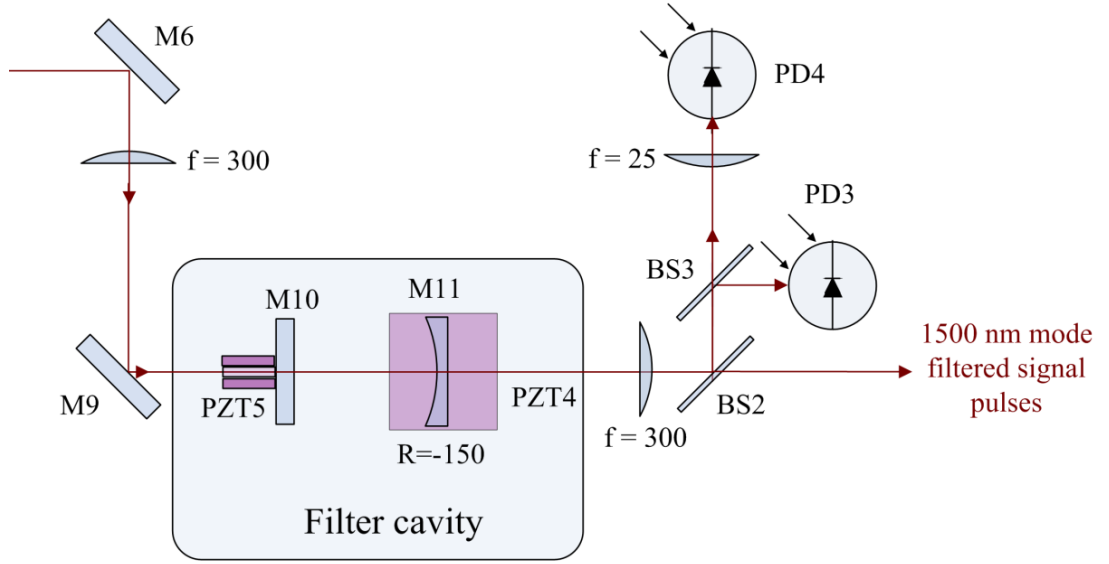


Figure 5.3 Optical configuration of the comb mode filtering cavity. *M*, HR dielectric mirror; *PZT*, piezoelectric stack; *BS*, beamsplitter; *PD*, photodiode.

The output from the OPO was focussed through the first lens and through the first cavity mirror, M10 (see Figure 5.3). This mirror was mounted on a ring PZT (Noliac CMAR03), so the beam passed through the hole at the centre. This PZT was used to lock the cavity length. The mount for the second cavity mirror, M11, was screwed onto a z-axis translation stage containing PZT4 (Thorlabs AE0505D08F). This allowed for manual tuning of the cavity length for larger distances through the screw actuator on the stage, or for small changes using a piezo-driver (Newport Microdrive Controller ESA-C) to control PZT4. The output from the cavity was collimated before BS2 (50:50) where half the output was used to monitor the output. BS3 (50:50) directed half of the output onto PD3 (Thorlabs Det 10/CM InGaAs Biased Detector), with the remainder passing through to PD4 (New Focus 1544-B). PD3 provided the signal for the feedback loop used for locking the cavity length; PD4 was monitored on an RF spectrum analyser (Rigol DSA 1030A).

The OPO frequency comb was locked to the stable reference (Rb clock) to ensure the input to the filter cavity had a stable average power and comb line spacing. The full optical configuration for filtering the stabilised frequency comb is presented in Figure 5.4.

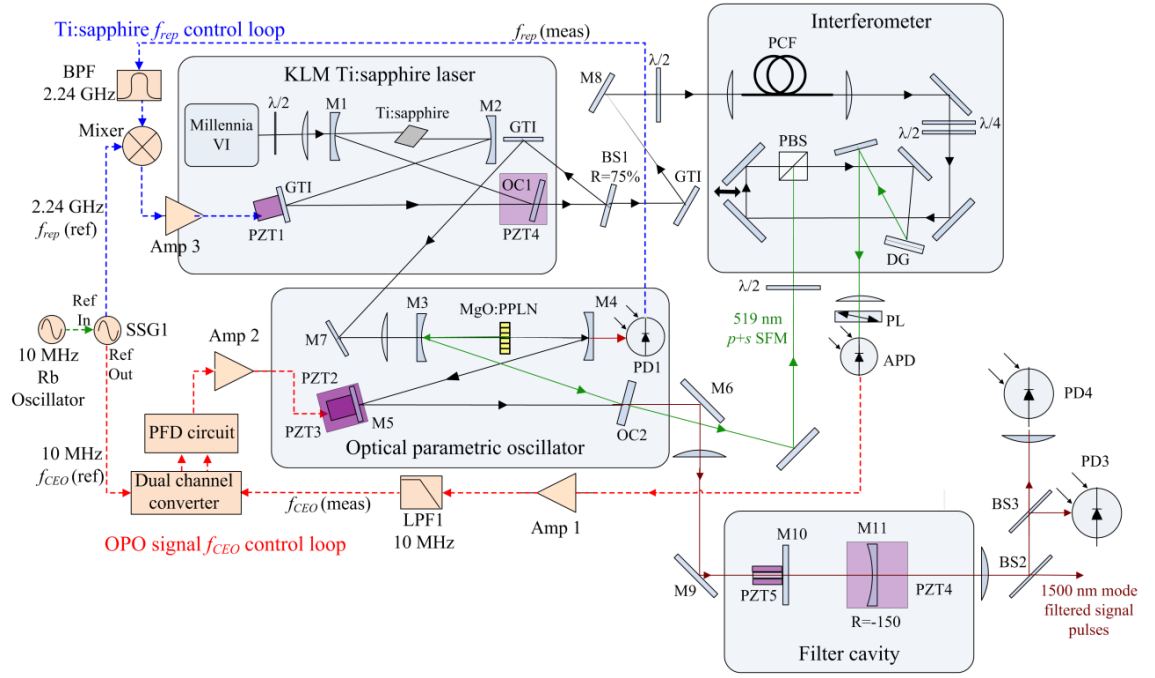


Figure 5.4 Optical configuration for filtering a stabilised frequency comb. The repetition frequency and CEO-frequency for signal pulses from an OPO frequency comb were transmitted by a filter cavity, increasing the comb line separation.

When the filter cavity was aligned to the stabilised frequency comb, the output mode spacing increased from 280 MHz (Figure 5.5(a)) to 1.4 GHz (Figure 5.5(b)). Using HR mirrors for the cavity reduced the output power, but gives narrow transmission peaks with good suppression of lower frequency comb lines.

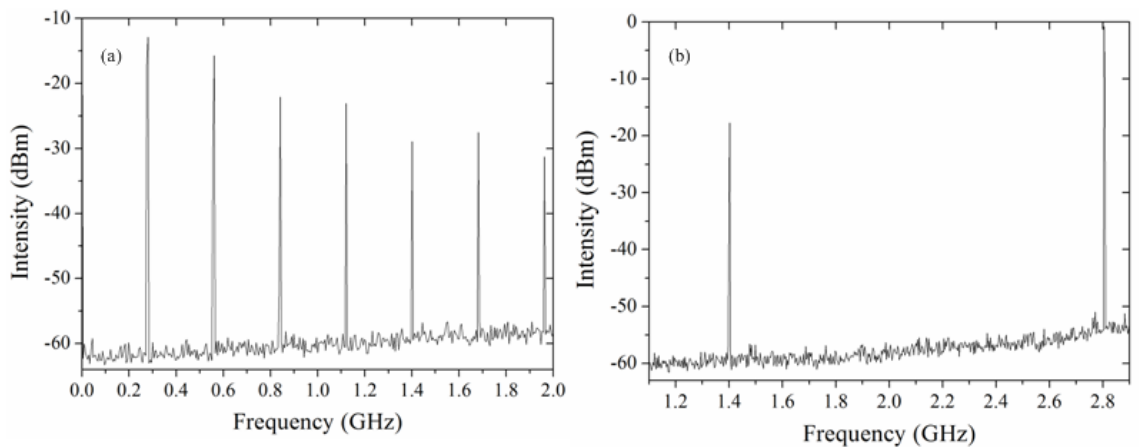


Figure 5.5 RF spectra of the OPO comb repetition frequency detected on PD4. (a) Repetition frequency with higher harmonics measured immediately after the OPO. (b) Output from the filter cavity showing fundamental and second harmonic at the increased mode spacing.

Temperature drifts in the lab meant the external cavity was only synchronised with the comb for very short periods of time (1 – 5 seconds), so a feedback loop was needed to lock the cavity length.

#### 5.4. Locking the external cavity to the frequency comb

The FSR of the filter cavity was locked at the fifth harmonic of the OPO frequency comb using dither locking. This technique was described in Section 4.1.3, with the feedback loop presented in Figure 4.5.

##### 5.4.1. Electrical locking loop

A New Focus LB1005 PI amplifier was used to lock the cavity length, with the output providing the input for PZT5. A low-noise power supply (Tektronix PWS 4323) was used in series to add a positive voltage offset onto the PZT so the combined scanning and locking signals would never result in it receiving an overall negative voltage. A low frequency (6 Hz) sine wave was used for “sweep-in” on the amplifier as the slow scan to produce a large transmission peak at PD3 (see Figure 5.6).

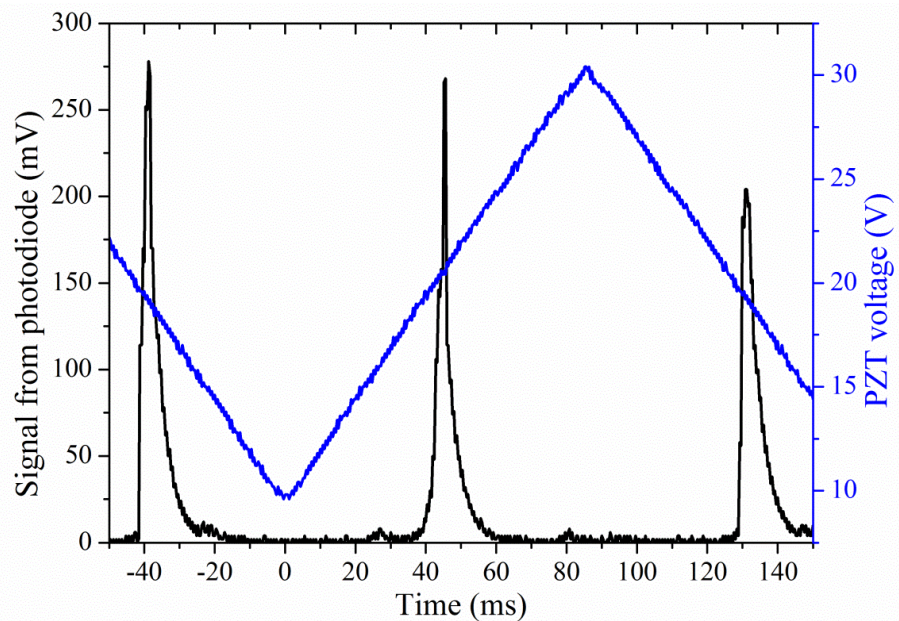


*Figure 5.6 Transmission peaks from the filter cavity (black) shown with the modulated error signal from the PI amplifier (blue) with the slow scan on (i.e. slow scan + dither modulation + error signal resulting from derivative).*



The high frequency modulation for dithering PZT5 was generated in a low noise lock-in amplifier (SRS810 DSP) which was used for “Mod In” on the PI amplifier and also high-pass filtered and amplified for one input of the mixer. This was a sine wave at 2.2 kHz with 100 mV amplitude. The signal from PD3 with the transmission peaks was also high-pass filtered and amplified for the other input. The signal at PD3 was noisier than had been the case with the ECDL, so a ProSound crossover unit was used as a low-pass filter (350 Hz) to give a sharper frequency cut-off after the mixer. The ProSound unit had a low input impedance, so a voltage buffer (or follower) was used before this low-pass filter to prevent loading of the mixer output. The low-pass filtered output from the mixer (the derivative of the transmission peak) is presented in Figure 5.7. As with the ECDL locking signals in Chapter 4, there is a time offset between where the “zero” point for the derivative is and the maximum from the photodiode. This results from where the two signals are monitored and will have no affect on the dither lock.

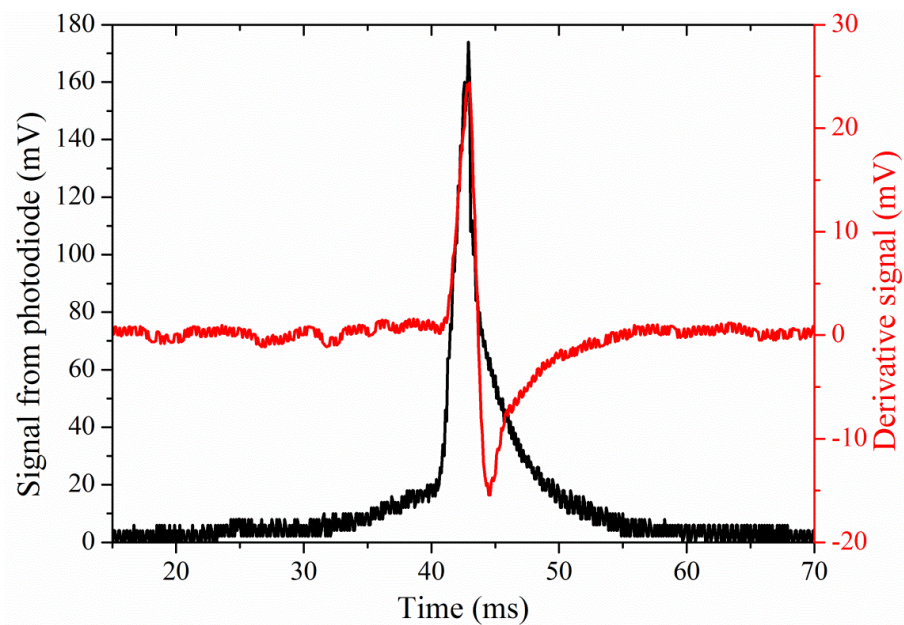


*Figure 5.7 A transmission peak from PD3 corresponding to Figure 5.6 (black). The derivative from the mixer is shown in red. The noise in this signal was higher than that observed when in the signal used for locking the ECDL.*

The derivative signal shown in Figure 5.7 was then used as the main input to the PI amplifier, from which the error signal onto PZT5 for locking was obtained. The full electronic configuration for locking the filter cavity to a harmonic of the OPO stabilised frequency comb is presented in Figure 5.8.

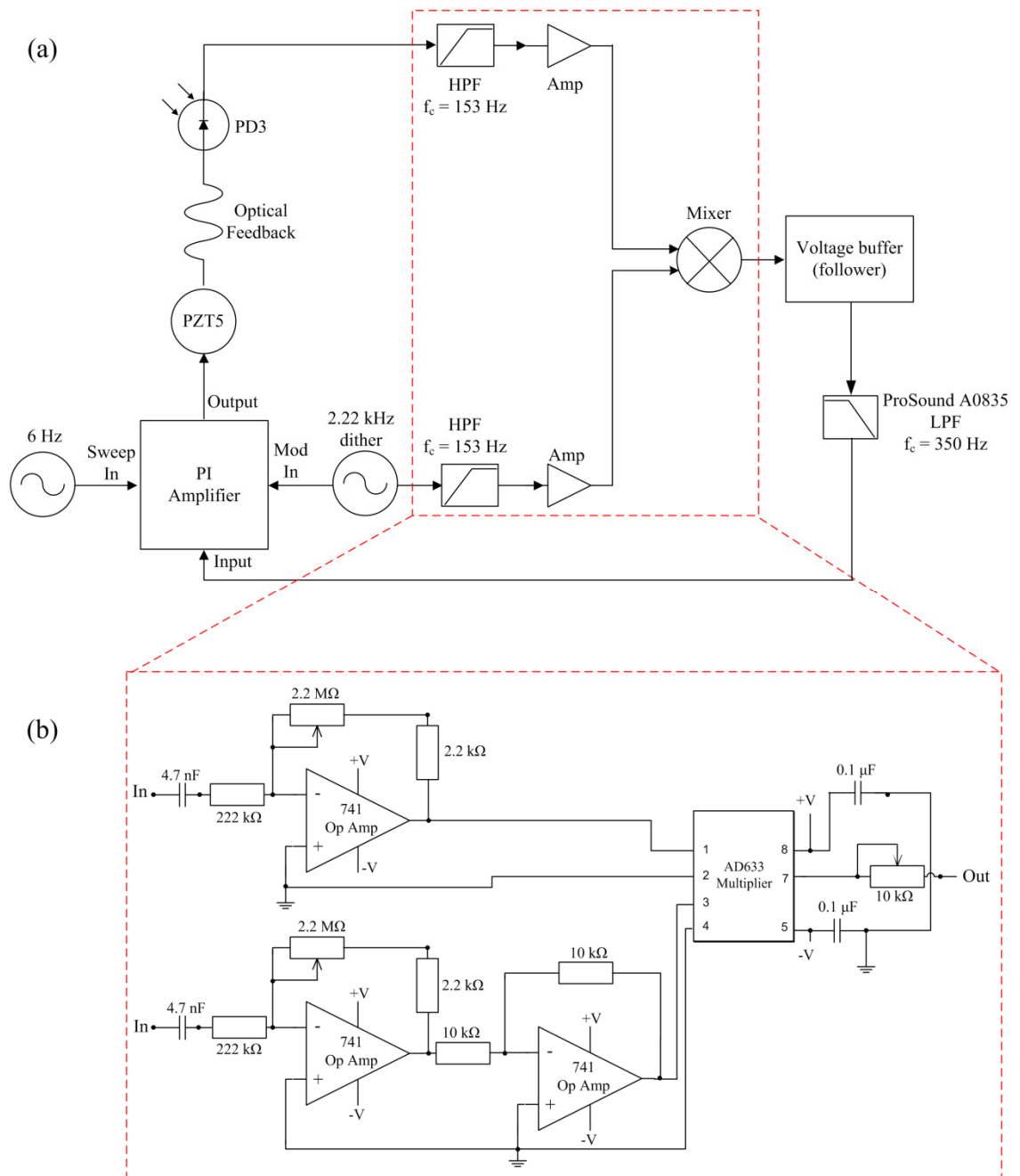
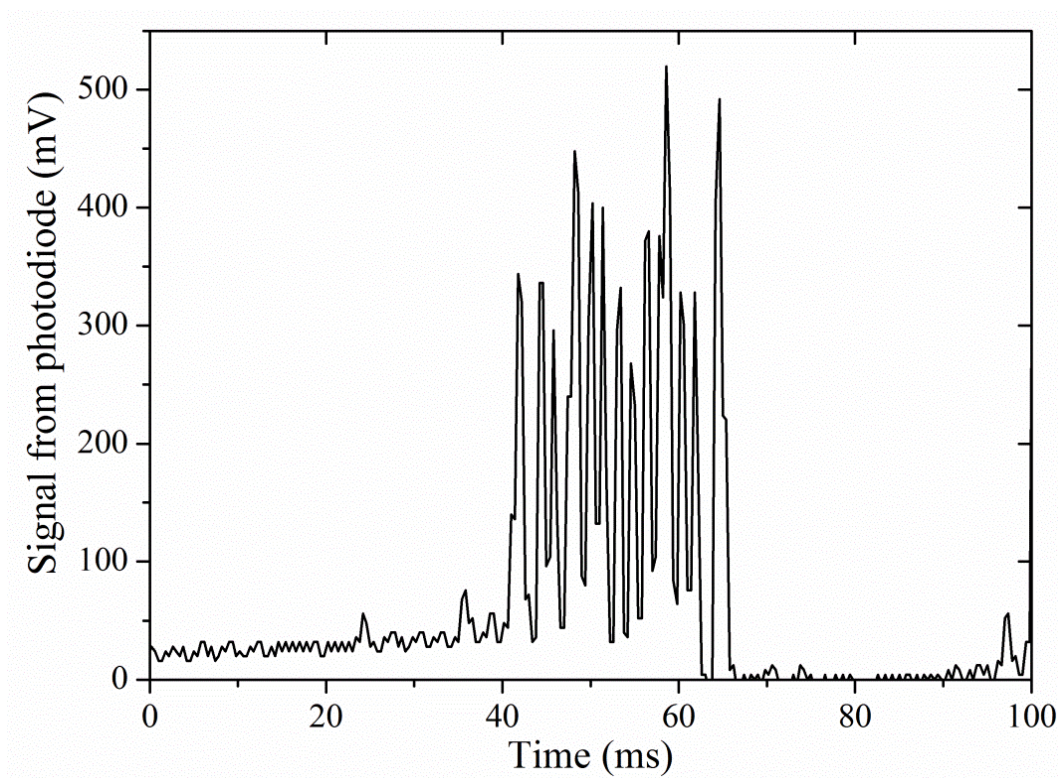


Figure 5.8 (a) The feedback loop used to lock the filter cavity to the fifth harmonic of the OPO. (b) The circuits built to filter, invert and amplify the two signals so the mixer inputs were matched in intensity and phase. HPF, high-pass filter; LPF, low-pass filter;  $f_c$ , corner frequency.

#### 5.4.2. Generating a suitable error signal

To lock the filter cavity length, the slow scan used to find the large peaks needed to be turned down to zero. As the voltage in this scan was reduced, the noise in the transmission peak increased considerably (see Figure 5.9).



*Figure 5.9 Transmission peak at PD3 when the sine wave slow scan is reduced to 1 V peak-to-peak. The break-up of the signal to multiple peaks increased with decreasing voltage in the slow scan.*

The slow scan was originally a triangular wave, as used in Chapter 4. This was changed to a sine wave to see if it improved the noise in the signal at PD3. The scan was also reduced in 1 Hz steps to from 6 Hz to 1 Hz, however this had no effect on the noise. Figure 5.9 shows the noise present for a 1 V sine wave scan at 6 Hz.

The noise in the transmission peak could be caused by a range of factors. The derivative signal from the mixer was disconnected from the PI amplifier to eliminate electronic feedback noise, and the high frequency dither amplitude was varied slightly, but this had no effect on the noise observed.

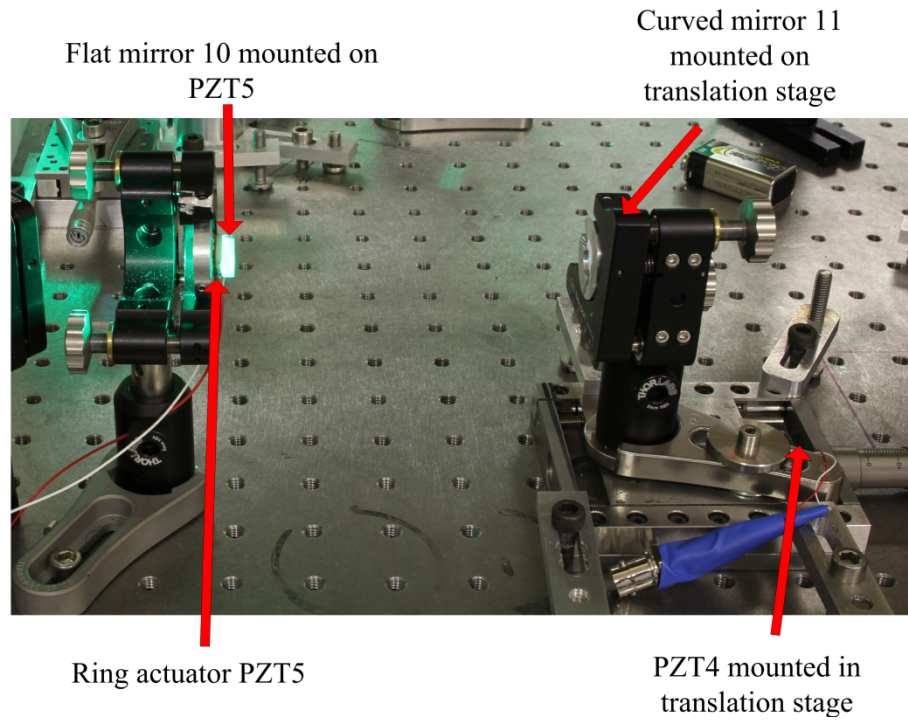


*Figure 5.10 Photograph of the original filter cavity. Standard Newport mirror mounts and Thorlabs posts and post holders were used to build the cavity. A box with a lid was placed around the cavity to reduce air currents and temperature drift.*

Two other sources of the multiple peaks were considered. The first of these was dispersion. The OPO comb lines were very narrow, and the finesse of the filter cavity was high ( $\sim 650$ ) so the transmission peaks transmitted through this were also narrow. We did not have the dispersion data for the coatings on the mirrors used, however if it was sufficient to ensure the comb lines were shifted so only some were synchronised with the filter cavity, this would have an effect on the transmission peaks. Adding dispersion to a simple cavity in a Matlab program did not produce anything like the fringes we observed in Figure 5.9, however to eliminate this possibility we changed the plane mirror (M10) for a 2% output coupler for 1500 – 1550. The signal from the PI amplifier was then connected to PZT4; this will have slightly increased the mirror displacement for the same applied voltage. The transmission peaks for slow scan voltages at 6 and 1 V are presented in Figure 5.11(c) and (d), below the measurements for the original cavity with HR mirrors. Reducing the finesse of the cavity to give higher transmission for broader peaks had no effect on the fringes in the transmission, so we ruled out dispersion as a cause.

The other source we had considered was mechanical noise and vibrations. Figure 5.10 is a photograph of the original cavity. The two cavity mirrors are mounted separately

using standard free-space optomechanics. Any mechanical disturbance happening for each mirror relative to the other will cause noise, in addition to any variations between vibrations on the mirrors and the input beam. The cavity was re-built using a cage mount system to reduce any differences in position for one mirror relative to the other. The transmission peaks for this system are presented in Figure 5.11(e) and (f).

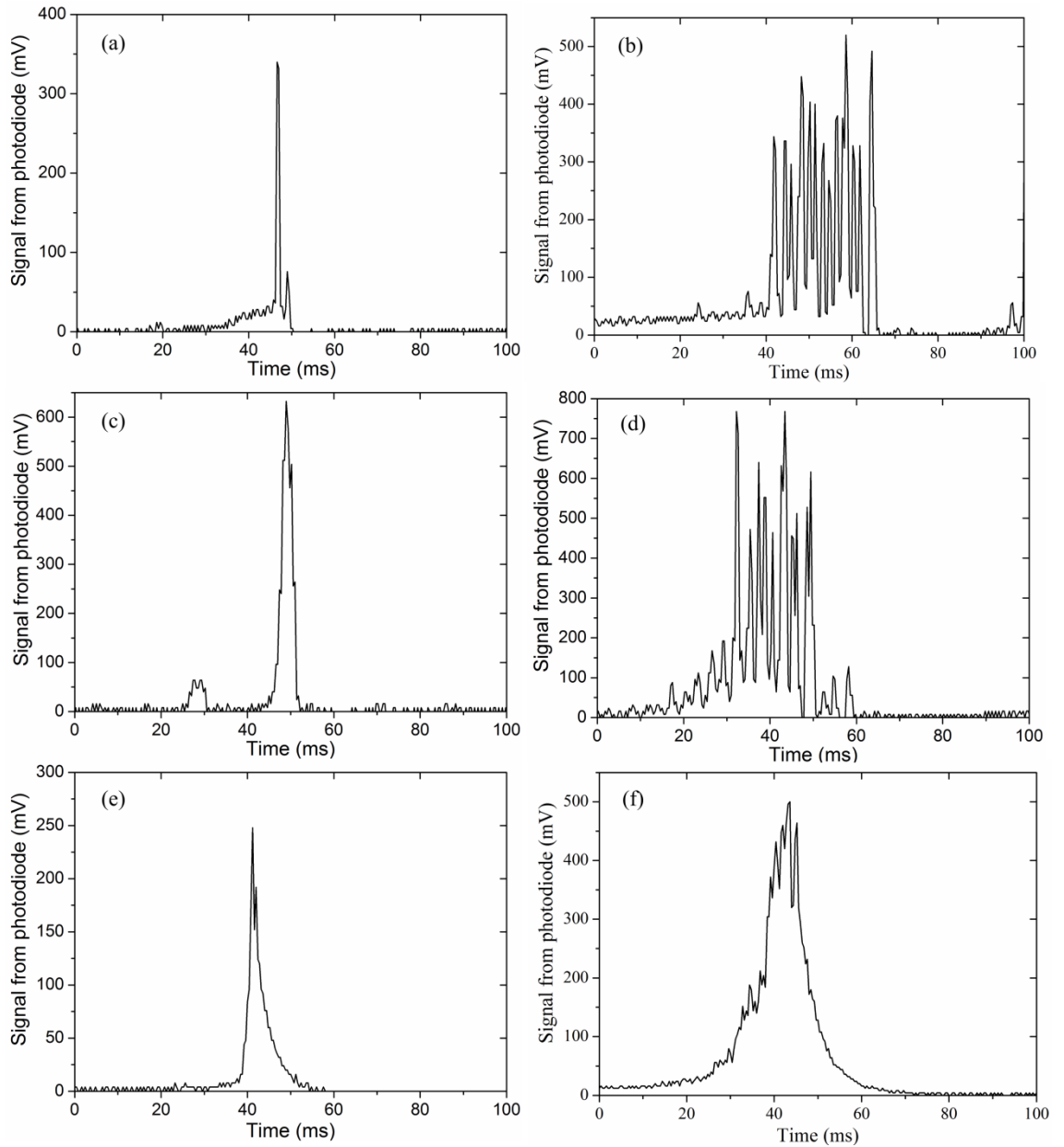


*Figure 5.11 Photodiode signals from PD3 for slow sweep signals to a PZT. (a) Original cavity with 6 V sine wave modulation. (b) Original cavity with 1 V sine wave modulation. (c) Second mirror substituted for 2% OC with 6 V modulation. (d) Second mirror substituted for 2% OC with 1 V modulation. (e) Cage mount cavity with 6 V modulation. (f) Cage mount cavity with 1 V modulation.*



The plane mirror bonded onto PZT5 was mounted in a kinematic mount with x and y-axis tilt, as with the original cavity. This was mounted on one end of the construction rods, with M11 held in a z-axis translation mount on the other side of the two supports. The micrometer translation stage was not used in this system, so PZT4 could not be used and the translation mount containing M11 provided the only length adjustment other than PZT5. This increased the difficulty of obtaining synchronism between this cavity and the OPO comb when the lab temperature drifted. The use of a more rigid mounting system reduced any mechanical drift between the two cavity mirrors and significantly reduced the noise fringes (see Figure 5.11(f)). The removal of x and y-axis tilt from M11 increased the difficulties of cavity alignment and although this system did provide greater stability, the cage mounts still allowed for mechanical vibrations that were not constant across the whole system, and moved as the temperature varied. This caused the alignment between the cavity and the OPO comb to drift slightly over time and was not easy to correct for without moving the position of the post holders that were screwed onto the optical bench.

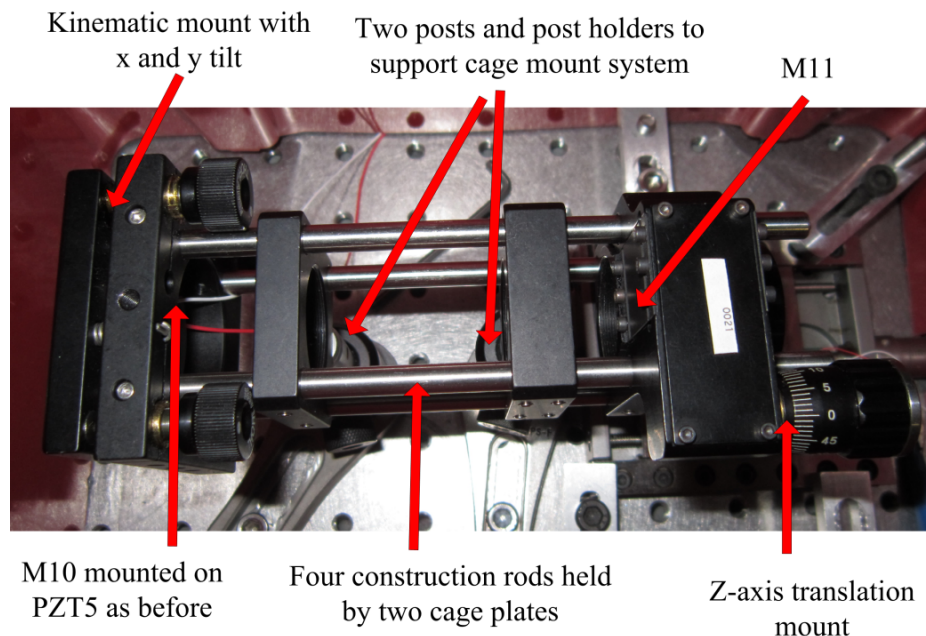


*Figure 5.12 Photograph of the filter cavity constructed using cage mount optomechanics. Two cage plates were mounted above the bench and supported the four construction rods. The mirror mounts containing M10 and M11 were mounted on either end of the rods. This increased the mechanical stability, but still led to some noise fringes in the transmission peaks.*

The transmission peak and derivative signals for the 1 V low frequency scan showed some noise fringes, but the zero-point for the derivative used for locking was clearly visible (Figure 5.13). As the voltage was further decreased the fringes did increase so it was hard to judge whether the lock was to the centre of the peak. This meant the transmission for the locked cavity was not always constant as the peak used could be from a fringe slightly to one side of where the maximum signal should be.

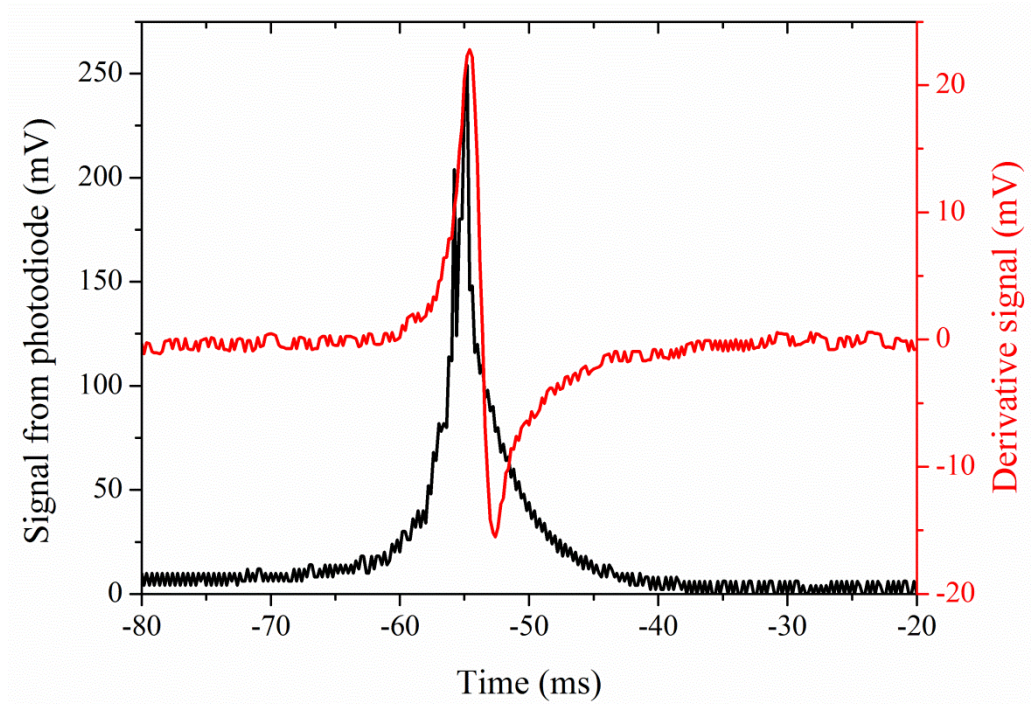


*Figure 5.13 Transmission peak (black) from PD3 and the derivative from the low-pass filtered mixer (red) for 1 V low frequency scan.*

The lock for the filter cavity relative to the OPO frequency comb was very sensitive to mechanical noise and vibrations in addition to any air currents. A person walking across the laboratory or speaking was often sufficient to cause the loop to drop out of lock. This sensitivity confirmed that a more stable mechanical system would be needed for any future experiments dependent on the lock and to carry out a full characterisation of the filtered comb.

## 5.5. Characterisation of the stabilised filter cavity

The best lock between the cavity length and the OPO stabilised comb could be maintained for 2 to 3 minutes and could be re-locked easily by changing the output offset on the PI amplifier or low noise power supply when the length change needed was outside the range of the dither lock loop ( $f_{\text{corner}} = 100$  Hz, LF gain limit = 20dB). After a few hours however, the z-axis translation mount had to be used to give a greater length adjustment. The limited rigidity of this system resulted in small changes in the x and y tilt/alignment when this was done, which in turn reduced the transmission through the cavity. Each time the alignment of the cavity was optimised other factors, such as the rate of temperature drift in the laboratory, would also vary, so the optimum settings on the PI amplifier would need to be adjusted slightly as different frequencies dominated the noise in the feedback loop. Spectra from an RF spectrum analyser were recorded during one of the most stable locks at PD4 and these are presented in Figures 5.14 and 5.15.

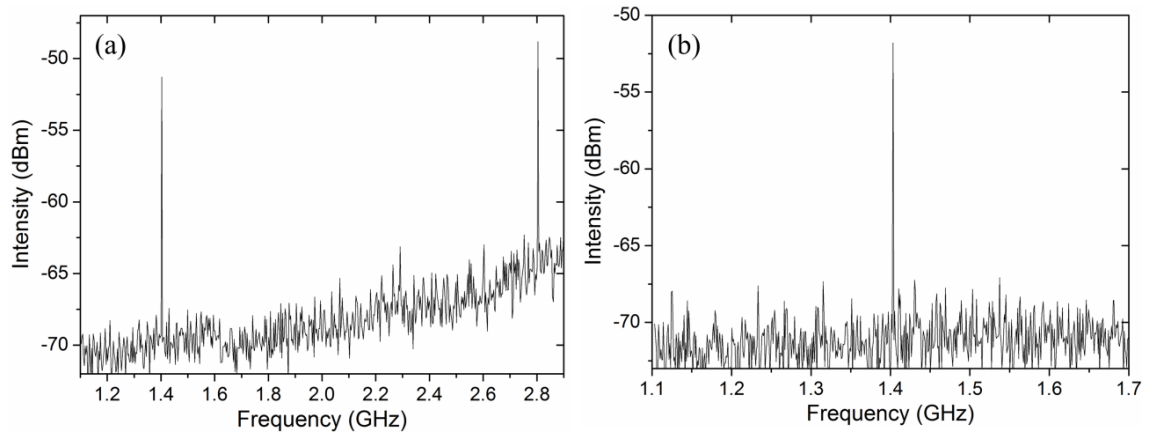


*Figure 5.14 Repetition frequency after the locked cavity recorded on a Rigol DSA 1030A RF spectrum analyser. (a) RF spectrum of the new fundamental and second harmonic recorded over a span of 1.8 GHz. The four high harmonics of the original mode spacing between these are not visible. (b) RF spectrum of the new fundamental repetition frequency over a span of 600 MHz with 100 kHz resolution. The fourth and sixth harmonics of the original repetition frequency have been strongly suppressed.*

RF spectra recorded over large frequency spans show the original comb line spacing has been strongly suppressed (see Figure 5.14). In Figure 5.15 the RF spectrum is shown over a span of 2 kHz with a resolution of 10 Hz. The -3 dB bandwidth was measured as 10 Hz (instrument-limited). These results suggest the passive cavity caused no



significant broadening of the stabilised comb lines, however the 10 Hz resolution of the RF spectrum analyser limits the certainty of any conclusions. The strong signal-to-noise ratio in Figures 5.14 and 5.15 show successful filtering of the comb modes, increasing the comb line separation to 1.4 GHz – the fifth harmonic of the original OPO comb.

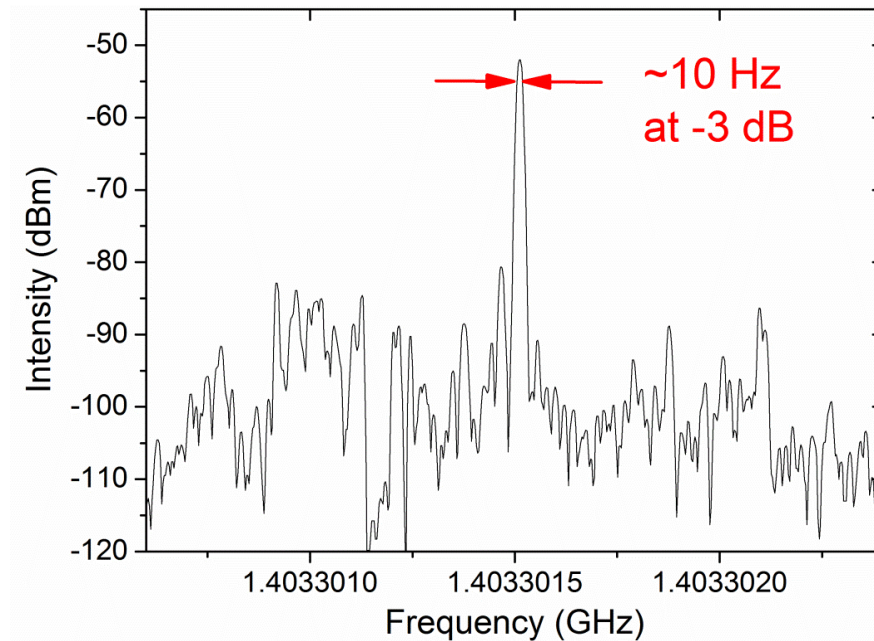


*Figure 5.15 Transmission through the locked filter cavity at PD4 recorded on a Rigol DSA 1030A RF spectrum analyser across 2 kHz with a time span of 20 s and instrument-limited resolution of 10 Hz. The -3 dB bandwidth was 10 Hz.*

The optical spectrum of the filtered stabilised frequency comb was recorded for the transmitted beam after BS2 (see Figure 5.16). The cavity lock was noisier for this measurement than it had been when recording the RF spectra. The power transmitted through the cavity was lower so the beam used for the OSA was weak. This resulted in noise on the optical spectrum.

The FWHM bandwidth measured on the spectrum was 8 nm (see Figure 5.16), which was only a third of the bandwidth for the original OPO comb. This may have been as a result of the mirrors between the OPO output coupler and BS2 all having slightly different HR coatings; some were for a wavelength range centred below 1500 nm whereas others were centred nearer 1550 nm. This will have induced losses across the spectrum of the frequency comb, so when a weak signal was measured the bandwidth would be reduced.

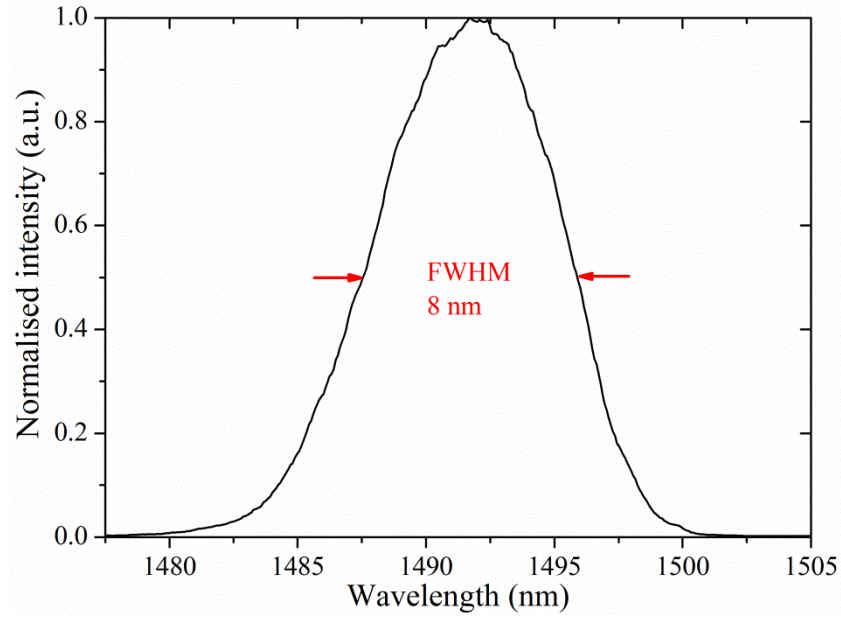


*Figure 5.16 Smoothed optical spectrum of the filtered OPO frequency comb measured on an OSA. The full-width at half-maximum bandwidth was measured as 8 nm.*

The RIN measurements recorded for the ECDL to test the stability of the lock used could not be repeated for this cavity as the signal from PD3 was not sufficiently stable after the initial lock. For the first few hours when the dither lock was achieved the PD signal was relatively stable and showed low noise, however subsequent locks did not achieve the same level of stability with noise levels varying depending on which fringe in the noise across the transmission peak the dither lock used. This meant that no consistent noise level could be measured as the recorded RIN would vary for each lock.

## **5.6. Conclusions and further work**

### **5.6.1. Conclusions**

The longitudinal modes of a stabilised frequency comb were filtered using a passive external cavity. The comb mode separation was increased from 280 MHz to 1.4 GHz. The external cavity was locked to the fifth harmonic of the comb using dither locking and the lock between the filter cavity and the OPO could be maintained for up to five minutes. Characterisation of the filtered comb included recording RF and optical spectra, however the sensitivity of the locking loop and overall instability of the system prevented further measurements. Significant changes are needed for a repeatable stable lock that will allow the stabilised comb to be used for any spectroscopic measurements.

### ***5.6.2. Further improvements and developments***

The noise in the locking loop could be reduced using the same improvements suggested in Chapter 4. Incorporating all the locking onto one circuit board with low-noise components and enclosing this in a shielded box, in addition to increasing the shielding for any cables and wires would immediately reduce the electrical noise. However the main limitations with this cavity were thermal drift and mechanical noise.

The air conditioning (A.C.) unit in the laboratory was noisy with significant changes in temperature and strong air currents. This caused large swings (several degrees Celsius) in temperature over a period of 24 hours. There were also large fluctuations in the temperature over shorter periods of a few minutes, as the A.C. unit had a high fan speed, even on the lowest setting, and the variation in temperature for the emitted air was significant. Two fan heaters were used in the laboratory to increase the heat load while the work in this chapter was carried out in an attempt to keep the A.C. on cooling only, however the large external wall in the lab and difference in temperature overnight still led to large variations. In addition to this, any time the laboratory door was opened the temperature would drop, causing the A.C. to start heating the air. A large baffle, which consisted of a twinwall polycarbonate sheet ( $\sim 2.5 \times 2$  m) supported by the gantry above the optical bench, was used once we started attempting to lock the filter cavity. This reduced the air flow directly from the A.C. fans onto the optical bench, however the fan speed and variations in air temperature were still sufficient to change the laboratory temperature and also to cause temperature variations between different areas of the optical bench.

In the long term an alternative solution will be needed to maintain a more stable temperature with fewer and smaller fluctuations over short and long time periods and also to reduce the temperature gradient across areas of the laboratory. Moving the A.C. sensor and installing a larger baffle closer to the A.C. fan are changes currently under consideration. Large scale improvements could include improving the insulation for the external wall; installing an intermediate area in the laboratory between the door and the optical benches to reduce temperature changes when people enter and leave the lab, and installing a new A.C. unit.

The optical bench could also be better insulated against air currents by using additional boxes around the cavities and beam path, and adding insulating layers around areas such as the filter cavity.

The filter cavity can be further stabilised by changing the method of mounting components and the materials used. If the temperature in the laboratory can be held closer to constant, a fixed cavity length can be used. This could use standard optical mounts held on a large block of invar (iron and nickel alloy) to dampen vibrations and reduce the distance and alignment variations with temperature. A more stable solution would be to use a single unit for the filter cavity, for example an “off-the-shelf” scanning 10 GHz Fabry-Pérot from Thorlabs (SA210-12B) where the mirrors are held in an invar case. The mechanical vibrations, air currents and temperature fluctuations across all areas of the optical system need to be minimised to achieve a long-term stable lock between the filter cavity and OPO frequency comb.

Once a more stable lock can be achieved over longer periods of time, other cavity lengths can be considered. A cavity with a FSR of 8.7 GHz was originally considered, transmitting the 31<sup>st</sup> harmonic of the OPO repetition frequency. Comb line separations approaching 10 GHz would allow this comb to be used for spectroscopic measurements.

A Michelson interferometer was built after the filter cavity in preparation for locking the planned 8.7 GHz filter cavity. This was designed to contain two retro-reflectors in one arm, with the first of these mounted on a speaker. This would offset the beam in x and y to allow multiple reflections (four) off of the retro-reflector so the distance travelled by the speaker would be multiplied by eight for the optical path. In this way a speaker with a travel of ~5 mm could give an optical path difference of 4 cm between the two arms of the interferometer, corresponding to twice the filter cavity length. The recombined beams would then be detected on a PD. Fourier transforms of the signal from the PD could be used to resolve the optical modes. Recording the PD signals with and without a gas cell, for example acetylene, in the fixed arm would give a spectroscopic measurement (based on the reduction in the intensity of comb lines). This would be a simple experiment to carry out in the laboratory to confirm the stabilised OPO frequency comb can be successfully used in spectroscopy.

In Chapter 6 conclusions will be drawn from all the results presented in thesis. Improvements and further developments for the OPO frequency comb and ECDL will also be discussed.

## Chapter 6. Conclusions and further developments

In this thesis I have presented experimental results for a synchronously pumped femtosecond OPO. The signal pulses from the OPO were repetition frequency and CEO-frequency stabilised to a high precision reference frequency to generate a fully stabilised frequency comb. The stabilisation of the CEO-frequency of the signal pulses was demonstrated with a free-running pump laser, therefore not requiring the use of an f-2f self-referencing interferometer and significantly reducing the experimental complexity. Preliminary work was carried out into filtering the frequency comb lines to increase the mode separation, making the stabilised comb more suited to high-precision spectroscopy measurements. An ECDL was also frequency stabilised to an absorption peak in Rb as an alternative high precision optical source for experiments with the frequency comb. The results for these systems are summarised below.

### 6.1. Summary of results for this thesis

In Chapter 2 the design and construction of the pump laser and synchronously pumped optical parametric oscillator were presented. The Ti:sapphire ring laser used to pump the OPO was stably modelocked at 793 nm with an average power of 1.4 W, a repetition frequency at 280 MHz and a pulse duration of 48 fs. This fulfilled the requirement of a high peak power for the pump source for the OPO and short pulse duration required for supercontinuum generation in the PCF. The ring OPO generated tunable signal pulses around 1500 nm with a pulse duration of  $\sim 135$  fs.

Chapter 3 introduced the locking electronics for stabilising the frequency comb. The CEO-frequency of the signal pulses from the OPO was stabilised with the pump laser left free-running. This reduced the complexity and the noise for the stabilised system by removing the requirement for an f-2f self-referencing interferometer and the associated electronics to lock the CEO-frequency of the laser. A range of noise measurements was carried out to fully characterise the stability of the locked OPO frequency comb. The bandwidth of the stabilised CEO-frequency of the signal pulses was measured as 10 Hz (instrument-limited). RIN measurements were made for the OPO whilst the CEO-frequency was locked, these gave a cumulative standard deviation of 0.04% (for a 64 second acquisition). This showed the power fluctuations in the OPO were low enough that the frequency comb had sufficient stability for metrology

measurements. Phase noise PSD data were recorded for the CEO-frequency and repetition frequency when the comb was locked yielding cumulative standard deviations of 0.09 Hz and 0.16 mHz respectively. This put an upper limit on the noise in the locked frequency comb of  $\sim 100$  Hz for an optical frequency of 200 THz. Two-sample frequency deviations were measured for the CEO-frequency and repetition frequency so the fractional instabilities of these could be calculated for a comb line at the OPO optical frequency. The upper limit for the fractional instability of a comb line was found to be  $2 \times 10^{-11}$ , limited only by the stability of the reference frequency used for the measurements.

In Chapter 4 the wavelength of an external cavity diode laser was stabilised to 780.2 nm, corresponding to the saturated absorption peak for the  $F=2$  to  $F'=2$  transition in  $^{87}\text{Rb}$ . RIN measurements showed the ECDL was stabilised with low noise and could be used as a stable high precision optical reference for a frequency comb. Some improvements to the electrical circuits and improved thermal and electrical insulation were suggested at the end of the chapter. These have now been implemented by a new PhD student, Karolis Balskus, and have successfully reduced the noise and increase the time over which the ECDL remained locked.

Preliminary experiments into filtering the longitudinal modes of the stabilised OPO frequency comb were presented in Chapter 5. The results confirmed that the repetition frequency of the comb could be increased whilst maintaining narrow comb lines at a wavelength suited to spectroscopic measurements. However, the sensitivity of the external filter cavity to thermal drift and mechanical vibrations necessitated a new cavity design with improved thermal management before a more complete characterisation could be carried out.

## **6.2. Further developments**

The main constraints on further developments of the OPO frequency comb are limitations in the environmental stability within the laboratory. The performance could also be improved with some electrical and optical alterations. The optical cavities included mirrors with a range of HR and AR coatings, so the central wavelength for the reflectivity was slightly offset for some mirrors relative to others. The MgO:PPLN crystal in the OPO was also AR coated for a shorter wavelength range than where we operated. This will have increased the parasitic losses and affected the control of

dispersion across the full wavelength range of the cavities. Using matching reflectivity coatings for all the optical components in each cavity could increase the output power from the OPO, although currently this is not a limiting factor for the system.

Some of the circuits in the locking loops are “home-built” with low-cost components. Exchanging these for low-noise equivalents, maximising the electrical shielding used, in addition to incorporating as many circuits as possible in to shielded boxes, should reduce the electrical noise present when the cavities are stabilised. Shielding all the wires and cables used between the circuits should also reduce some of the cross-talk between different signals. Substituting mains operated power supply units for batteries for some components will also reduce the low frequency noise.

The main methods for addressing the environmental instabilities were addressed in Chapter 5. Isolating cavities from mechanical noise and vibrations by avoiding mounting cavities directly onto the optical bench and increasing the rigidity of some areas – such as using a fixed length, single-piece comb mode filtering cavity – should increase the tolerance of all the locking loops to external sources of noise. Additional boxes and beam pipes around the optical beam path would further shield the cavities from rapid changes in temperature. Addressing the long-term temperature drift could involve more significant changes to the air conditioning unit in the laboratory and improved thermal isolation of the laboratory from the external environment.

If these changes lead to a more stable lock for the filter cavity after the OPO, a range of mode filtering configurations could be investigated, dependent on the comb line power and spacing required.

There are further experiments that can be done with the frequency comb without the need for improving the environmental stability. The Rb-stabilised ECDL could be used as a high-precision optical reference for comparisons with the stabilised OPO frequency comb, or as an alternative reference source. The noise measurements in Chapter 3 could then be repeated to see if the use of an optical reference frequency can reduce the noise in the CEO-frequency lock. The mirror set in the OPO could also be changed so the signal pulses operate in the mid-IR region of the spectrum, allowing future experiments to be conducted at wavelengths suited to a wider range of spectroscopic applications.

A simplified system was used for generating a stabilised OPO frequency comb. Removing the  $f$ - $2f$  stabilisation has reduced the pump source complexity and increased

the range of sources that could be used. Using an OPO for the comb increases the flexibility of the source, as changing the mirror set can allow for a large degree of spectral coverage from the visible up to the mid-IR. The noise characterisations for the stabilised OPO comb confirm the suitability of this system to high-precision applications.



## References

1. S. T. Cundiff, "Topical Review: Phase stabilization of ultrashort optical pulses," *Journal of Physics D: Applied Physics* **35**(8), 43-59 (2002).
2. J. Ye and S. T. Cundiff, Ch. 1 "Introduction," in *Femtosecond Optical Frequency Comb Technology; Principle, Operation and Applications*, J. Ye and S. T. Cundiff, eds. (Springer, 2005), pp. 12-53.
3. H. R. Telle, G. Steinmeyer, A. E. Dunlop, J. Stenger, D. H. Sutter, and U. Keller, "Carrier-envelope offset phase control: A novel concept for absolute optical frequency measurement and ultrashort pulse generation," *Appl. Phys. B-Lasers Opt.* **69**(4), 327-332 (1999).
4. S. T. Cundiff, J. Ye, and J. L. Hall, "Optical frequency synthesis based on mode-locked lasers," *Rev. Sci. Instrum.* **72**(10), 3749-3771 (2001).
5. T. Udem, R. Holzwarth, and T. W. Hänsch, "Optical frequency metrology," *Nature* **416**(6877), 233-237 (2002).
6. J. Ye, H. Schnatz, and L. W. Hollberg, "Optical frequency combs: From frequency metrology to optical phase control," *IEEE J. Sel. Top. Quantum Electron.* **9**(4), 1041-1058 (2003).
7. S. A. Diddams, J. Ye, and L. Hollberg, Ch. 9 "Femtosecond Lasers For Optical Clocks and Low Noise Frequency Synthesis," in *Femtosecond Optical Frequency Comb Technology; Principle, Operation and Applications*, J. Ye and S. T. Cundiff, eds. (Springer, 2005), pp. 225-262.
8. T. Udem, "Spectroscopy: Frequency comb benefits," *Nat. Photonics* **3**(2), 82-84 (2009).
9. S.-W. Kim, "Metrology: Combs rule," *Nat. Photonics* **3**(6), 313-314 (2009).
10. J. Sun and D. T. Reid, "Coherent ultrafast pulse synthesis between an optical parametric oscillator and a laser," *Opt. Lett.* **34**(6), 854-856 (2009).
11. R. A. McCracken, J. Sun, C. G. Leburn, and D. T. Reid, "Broadband phase coherence between an ultrafast laser and an OPO using lock-to-zero CEO stabilization," *Opt. Express* **20**(15), 16269-16274 (2012).
12. D. J. Jones, S. A. Diddams, J. K. Ranka, A. Stentz, R. S. Windeler, J. L. Hall, and S. T. Cundiff, "Carrier-Envelope Phase Control of Femtosecond Mode-Locked Lasers and Direct Optical Frequency Synthesis," *Science* **288**(5466), 635-639 (2000).

13. T. Udem, S. A. Diddams, K. R. Vogel, C. W. Oates, E. A. Curtis, W. D. Lee, W. M. Itano, R. E. Drullinger, J. C. Bergquist, and L. Hollberg, "Absolute Frequency Measurements of the  $\text{Hg}^+$  and Ca Optical Clock Transitions with a Femtosecond Laser," *Phys. Rev. Lett.* **86**(22), 4996-4999 (2001).
14. B. R. Washburn, S. A. Diddams, N. R. Newbury, J. W. Nicholson, M. F. Yan, and C. G. Jørgensen, "Phase-locked, erbium-fiber-laser-based frequency comb in the near infrared," *Opt. Lett.* **29**(3), 250-252 (2004).
15. N. R. Newbury and W. C. Swann, "Low-noise fiber-laser frequency combs (Invited)," *J. Opt. Soc. Am. B-Opt. Phys.* **24**(8), 1756-1770 (2007).
16. S. A. Diddams, L. Hollberg, and V. Mbele, "Molecular fingerprinting with the resolved modes of a femtosecond laser frequency comb," *Nature* **445**(7128), 627-630 (2007).
17. M. J. Thorpe, D. D. Hudson, K. D. Moll, J. Lasri, and J. Ye, "Cavity-ringdown molecular spectroscopy based on an optical frequency comb at 1.45-1.65  $\mu\text{m}$ ," *Opt. Lett.* **32**(3), 307-309 (2007).
18. I. Coddington, W. C. Swann, and N. R. Newbury, "Coherent Multiheterodyne Spectroscopy Using Stabilized Optical Frequency Combs," *Phys. Rev. Lett.* **101**(4), 0139021-0139024 (2008).
19. B. Bernhardt, A. Ozawa, P. Jacquet, M. Jacquy, Y. Kobayashi, T. Udem, R. Holzwarth, G. Guelachvili, T. W. Hänsch, and N. Picqué, "Cavity-enhanced dual-comb spectroscopy," *Nat. Photonics* **4**(1), 55-57 (2010).
20. K. A. Tillman, R. Thapa, K. Knabe, S. Wu, J. K. Lim, B. R. Washburn, and K. L. Corwin, "Stabilization of a self-referenced, prism-based, Cr:forsterite laser frequency comb using an intracavity prism," *Appl. Opt.* **48**(36), 6980-6989 (2009).
21. J. K. Lim, K. Knabe, K. A. Tillman, W. Neely, Y. S. Wang, R. Amezcua-Correa, F. Couny, P. S. Light, F. Benabid, J. C. Knight, K. L. Corwin, J. W. Nicholson, and B. R. Washburn, "A phase-stabilized carbon nanotube fiber laser frequency comb," *Opt. Express* **17**(16), 14115-14120 (2009).
22. J. J. McFerran, W. C. Swann, B. R. Washburn, and N. R. Newbury, "Suppression of pump-induced frequency noise in fiber-laser frequency combs leading to sub-radian  $f_{\text{ceo}}$  phase excursions," *Appl. Phys. B-Lasers Opt.* **86**(2), 219-227 (2007).
23. T. I. Ferreiro, J. Sun, and D. T. Reid, "Frequency stability of a femtosecond optical parametric oscillator frequency comb," *Opt. Express* **19**(24), 24159-24164 (2011).

24. Y. R. Shen, Ch. 9 "Parametric Amplification and Oscillation," in *Principles of Nonlinear Optics* (Wiley-Interscience, 1984), pp. 117-140.
25. D. C. Edelstein, E. S. Wachman, and C. L. Tang, "Broadly tunable high repetition rate femtosecond optical parametric oscillator," *Appl. Phys. Lett.* **54**(18), 1728-1730 (1989).
26. B. R. Washburn, S. E. Ralph, J. K. Ranka, and R. S. Windeler, "Controlling the phase of a femtosecond optical parametric oscillator via coherent mixing of the pump-generated supercontinuum and an OPO subharmonic," in *Lasers and Electro-Optics Society 2000 Annual Meeting. LEOS 2000. 13th Annual Meeting. IEEE*, (2000), 298-299.
27. D. T. Reid, B. J. S. Gale, and J. Sun, "Frequency Comb Generation and Carrier-Envelope Phase Control in Femtosecond Optical Parametric Oscillators," *Laser Phys.* **18**(2), 87-103 (2008).
28. S. A. Diddams, L.-S. Ma, J. Ye, and J. L. Hall, "Broadband optical frequency comb generation with a phase-modulated parametric oscillator," *Opt. Lett.* **24**(23), 1747-1749 (1999).
29. Y. Kobayashi and K. Torizuka, "Measurement of the optical phase relation among subharmonic pulses in a femtosecond optical parametric oscillator," *Opt. Lett.* **25**(11), 856-858 (2000).
30. Y. Kobayashi and K. Torizuka, "Carrier-phase control among subharmonic pulses in a femtosecond optical parametric oscillator," *Opt. Lett.* **26**(16), 1295-1297 (2001).
31. Y. Kobayashi, H. Takada, M. Kakehata, and K. Torizuka, "Optical phase locking among femtosecond subharmonic pulses," *Opt. Lett.* **28**(15), 1377-1379 (2003).
32. Y. Kobayashi, H. Takada, M. Kakehata, and K. Torizuka, "Phase-coherent multicolor femtosecond pulse generation," *Appl. Phys. Lett.* **83**(5), 839-841 (2003).
33. J. Sun, B. J. S. Gale, and D. T. Reid, "Dual-color operation of a femtosecond optical parametric oscillator exhibiting stable relative carrier-envelope phase-slip frequencies," *Opt. Lett.* **31**(13), 2021-2023 (2006).
34. J. Sun, B. J. S. Gale, and D. T. Reid, "Testing the parametric energy conservation law in a femtosecond optical parametric oscillator," *Opt. Express* **15**(7), 4378-4384 (2007).

35. J. Sun, B. J. S. Gale, and D. T. Reid, "Coherent synthesis using carrier-envelope phase-controlled pulses from a dual-color femtosecond optical parametric oscillator," *Opt. Lett.* **32**(11), 1396-1398 (2007).
36. J. H. Sun, B. J. S. Gale, and D. T. Reid, "Composite frequency comb spanning 0.4-2.4  $\mu\text{m}$  from a phase-controlled femtosecond Ti:sapphire laser and synchronously pumped optical parametric oscillator," *Opt. Lett.* **32**(11), 1414-1416 (2007).
37. R. Gebs, T. Dekorsy, S. A. Diddams, and A. Bartels, "1-GHz repetition rate femtosecond OPO with stabilized offset between signal and idler frequency combs," *Opt. Express* **16**(8), 5397-5405 (2008).
38. B. J. S. Gale, J. H. Sun, and D. T. Reid, "Towards versatile coherent pulse synthesis using femtosecond laser and optical parametric oscillators," *Opt. Express* **16**(3), 1616-1622 (2008).
39. J. Sun, B. J. S. Gale, and D. T. Reid, "Control of the carrier-envelope phases of a synchronously pumped femtosecond optical parametric oscillator and its applications," *Chinese Science Bulletin* **53**(5), 642-651 (2008).
40. S. T. Wong, T. Plettner, K. L. Vodopyanov, K. Urbanek, M. Digonnet, and R. L. Byer, "Self-phase-locked degenerate femtosecond optical parametric oscillator," *Opt. Lett.* **33**(16), 1896-1898 (2008).
41. F. Adler, K. C. Cossel, M. J. Thorpe, I. Hartl, M. E. Fermann, and J. Ye, "Phase-stabilized, 1.5 W frequency comb at 2.8-4.8  $\mu\text{m}$ ," *Opt. Lett.* **34**(9), 1330-1332 (2009).
42. F. Adler, P. Maslowski, A. Foltynowicz, K. C. Cossel, T. C. Briles, I. Hartl, and J. Ye, "Mid-infrared Fourier transform spectroscopy with a broadband frequency comb," *Opt. Express* **18**(21), 21861-21872 (2010).
43. S. T. Wong, K. L. Vodopyanov, and R. L. Byer, "Self-phase-locked divide-by-2 optical parametric oscillator as a broadband frequency comb source," *J. Opt. Soc. Am. B* **27**(5), 876-882 (2010).
44. T. I. Ferreiro, J. Sun, and D. T. Reid, "Locking the carrier-envelope-offset frequency of an optical parametric oscillator without f-2f self-referencing," *Opt. Lett.* **35**(10), 1668-1670 (2010).
45. D. T. Reid, J. Sun, T. P. Lamour, and T. I. Ferreiro, "Advances in ultrafast optical parametric oscillators," *Laser Phys. Lett.* **8**(1), 8-15 (2011).

46. N. Leindecker, A. Marandi, R. L. Byer, and K. L. Vodopyanov, "Broadband degenerate OPO for mid-infrared frequency comb generation," *Opt. Express* **19**(7), 6296-6302 (2011).
47. K. L. Vodopyanov, E. Sorokin, I. T. Sorokina, and P. G. Schunemann, "Mid-IR frequency comb source spanning 4.4-5.4  $\mu\text{m}$  based on subharmonic GaAs optical parametric oscillator," *Opt. Lett.* **36**(12), 2275-2277 (2011).
48. Z. Zhang, C. Gu, J. Sun, C. Wang, T. Gardiner, and D. T. Reid, "Asynchronous midinfrared ultrafast optical parametric oscillator for dual-comb spectroscopy," *Opt. Lett.* **37**(2), 187-189 (2012).
49. M. Vainio, M. Merimaa, L. Halonen, and K. Vodopyanov, "Degenerate 1 GHz repetition rate femtosecond optical parametric oscillator," *Opt. Lett.* **37**(21), 4561-4563 (2012).
50. K. F. Lee, J. Jiang, C. Mohr, J. Bethge, M. E. Fermann, N. Leindecker, K. L. Vodopyanov, P. G. Schunemann, and I. Hartl, "Carrier envelope offset frequency of a doubly resonant, nondegenerate, mid-infrared GaAs optical parametric oscillator," *Opt. Lett.* **38**(8), 1191-1193 (2013).
51. M. W. Haakestad, T. P. Lamour, N. Leindecker, A. Marandi, and K. L. Vodopyanov, "Intracavity trace molecular detection with a broadband mid-IR frequency comb source," *J. Opt. Soc. Am. B* **30**(3), 631-640 (2013).
52. A. Schliesser, N. Picqué, and T. W. Hänsch, "Mid-infrared frequency combs," *Nat. Photonics* **6**(7), 440-449 (2012).
53. N. Leindecker, A. Marandi, R. L. Byer, K. L. Vodopyanov, J. Jiang, I. Hartl, M. Fermann, and P. G. Schunemann, "Octave-spanning ultrafast OPO with 2.6-6.1  $\mu\text{m}$  instantaneous bandwidth pumped by femtosecond Tm-fiber laser," *Opt. Express* **20**(7), 7046-7053 (2012).
54. Z. Zhang, T. Gardiner, and D. T. Reid, "Asynchronous modelocked Yb:KYW lasers for dual-comb spectroscopy," *Electronics Letters* **47**(20), 1140-1142 (2011).
55. Z. Zhang, J. Sun, T. Gardiner, and D. T. Reid, "Broadband conversion in an Yb:KYW-pumped ultrafast optical parametric oscillator with a long nonlinear crystal," *Opt. Express* **19**(18), 17127-17132 (2011).
56. T. Steinmetz, T. Wilken, C. Araujo-Hauck, R. Holzwarth, T. W. Hänsch, and T. Udem, "Fabry-Pérot filter cavities for wide-spaced frequency combs with large spectral bandwidth," *Appl. Phys. B* **96**(2-3), 251-256 (2009).
57. W. E. Lamb, Jr., "Theory of an Optical Maser," *Phys. Rev.* **134**(6A), A1429-A1450 (1964).

58. L. E. Hargrove, R. L. Fork, and M. A. Pollack, "Locking Of He-Ne Laser Modes Induced By Synchronous Intracavity Modulation," *Appl. Phys. Lett.* **5**(1), 4-5 (1964).
59. E. P. Ippen, C. V. Shank, and A. Dienes, "Passive mode locking of the cw dye laser," *Appl. Phys. Lett.* **21**(8), 348-350 (1972).
60. R. Paschotta and U. Keller, Ch. 1 "Ultrafast Solid-State Lasers," in *Ultrafast Lasers: Technology and Applications*, M. E. Fermann, A. Galvanauskas, and G. Sucha, eds. (Marcel Dekker, Inc, 2003), pp. 1-60.
61. U. Keller, "Recent developments in compact ultrafast lasers," *Nature* **424**(6950), 831-838 (2003).
62. M. Fox, Ch. 4 "Radiative transitions in atoms," in *Quantum Optics: An Introduction* (Oxford University Press, 2007), pp. 48-71.
63. A. Yariv and P. Yeh, Ch. 6 "Theory of Laser Oscillations and Some Specific Laser Systems," in *Photonics: Optical Electronics in Modern Communications*, 6th Edn. (Oxford University Press, 2007), pp. 237-312.
64. J. Wilson and J. Hawkes, Ch. 6 "Lasers II," in *Optoelectronics: an introduction*, 3rd Edn. (Prentice Hall Europe, 1998), pp. 244-292.
65. A. E. Siegman, Ch. 27 "Active Laser Mode-Coupling," in *Lasers* (University Science Books, 1986), pp. 1041-1103.
66. F. X. Kärtner and U. Keller, "Stabilization of solitonlike pulses with a slow saturable absorber," *Opt. Lett.* **20**(1), 16-18 (1995).
67. W. Koechner, Ch. 9 "Mode Locking," in *Solid-State Laser Engineering*, 6th Edn. (Springer, 2006), pp. 534-586.
68. M. Becker, D. J. Kuizenga, and A. Siegman, "Harmonic mode locking of the Nd:YAG laser," *IEEE J. Quantum Elect.* **8**(8), 687-693 (1972).
69. W. S. Pelouch, P. E. Powers, and C. L. Tang, "Self-starting mode-locked ring-cavity Ti:sapphire laser," *Opt. Lett.* **17**(22), 1581-1583 (1992).
70. P. F. Moulton, "Spectroscopic and laser characteristics of Ti:Al<sub>2</sub>O<sub>3</sub>," *J. Opt. Soc. Am. B* **3**(1), 125-133 (1986).
71. A. Yariv and P. Yeh, Ch. 1 "Electromagnetic Fields and Waves," in *Photonics: Optical Electronics in Modern Communications*, 6th Edn. (Oxford University Press, 2007), pp. 1-65.
72. Y. Y. Zhao, P. Wang, W. Zhang, J. R. Tian, and Z. Y. Wei, "Generation of 7-fs laser pulse directly from a compact Ti:sapphire laser with chirped mirrors," *Sci. China Ser. G* **50**(3), 261-266 (2007).

73. M. Bass, Ch. 33 "Properties of Crystals and Glasses," in *Handbook of Optics*, 2nd Edn. (McGraw-Hill, 1995).
74. R. W. Boyd, Ch. 1 "The Nonlinear Optical Susceptibility," in *Nonlinear Optics*, 3rd Edn. (Academic Press, 2008), pp. 1-67.
75. W. Koechner, Ch. 10 "Nonlinear Devices," in *Solid-State Laser Engineering*, 6th Edn. (Springer, 2006), pp. 587-679.
76. D. E. Spence, P. N. Kean, and W. Sibbett, "60-fsec pulse generation from a self-mode-locked Ti:sapphire laser," *Opt. Lett.* **16**(1), 42-44 (1991).
77. R. W. Boyd, Ch. 7 "Processes Resulting from the Intensity-Dependent Refractive Index," in *Nonlinear Optics*, 2nd Edn. (Academic Press, 2003), pp. 311-370.
78. J. Hecht, Ch. 24 "Tunable Vibronic Solid-State Lasers," in *The Laser Guidebook*, 2nd Edn. (McGraw-Hill, Inc, 1999), pp. 425-446.
79. W. Koechner, Ch. 2 "Properties of Solid-State Laser Materials," in *Solid-State Laser Engineering*, 6th Edn. (Springer, 2006), pp. 39-101.
80. P. Moulton, "Ti-doped sapphire: tunable solid-state laser," *Optics News* **8**(6), 9 (1982).
81. A. Bartels, T. Dekorsy, and H. Kurz, "Femtosecond Ti:sapphire ring laser with a 2-GHz repetition rate and its application in time-resolved spectroscopy," *Opt. Lett.* **24**(14), 996-998 (1999).
82. A. Kasper and K. J. Witte, "10-fs pulse generation from a unidirectional Kerr-lens mode-locked Ti:sapphire ring laser," *Opt. Lett.* **21**(5), 360-362 (1996).
83. G. T. Nogueira and F. C. Cruz, "Efficient 1 GHz Ti:sapphire laser with improved broadband continuum in the infrared," *Opt. Lett.* **31**(13), 2069-2071 (2006).
84. M. S. Kirchner, T. M. Fortier, A. Bartels, and S. A. Diddams, "A low-threshold self-referenced Ti:Sapphire optical frequency comb," *Opt. Express* **14**(20), 9531-9536 (2006).
85. F. C. Cruz and G. T. Nogueira, "Broadband 2 GHz Femtosecond Ti:Sapphire Laser," in *Conference on Lasers and Electro-Optics*, OSA Technical Digest Series (CD) (Optical Society of America, 2007), JThD6.
86. F. Gires and P. Tournois, "Interferometre utilisable pour la compression d'impulsions lumineuses modulées en fréquence," *C. R. Acad. Sci. Paris* **258** 6112-6115 (1964).
87. J. Heppner and J. Kuhl, "Intracavity chirp compensation in a colliding pulse mode-locked laser using thin-film interferometers," *Appl. Phys. Lett.* **47**(5), 453-455 (1985).

88. A. Robertson, U. Ernst, R. Knappe, R. Wallenstein, V. Scheuer, T. Tschudi, D. Burns, M. D. Dawson, and A. I. Ferguson, "Prismless diode-pumped mode-locked femtosecond Cr:LiSAF laser," *Opt. Commun.* **163**(1-3), 38-43 (1999).
89. B. Golubovic, R. R. Austin, M. K. Steiner-Shepard, M. K. Reed, S. A. Diddams, D. J. Jones, and A. G. Van Engen, "Double Gires-Tournois interferometer negative-dispersion mirrors for use in tunable mode-locked lasers," *Opt. Lett.* **25**(4), 275-277 (2000).
90. A. E. Siegman, Ch. 15 "Ray Optics and Ray Matrices," in *Lasers* (University Science Books, 1986), pp. 581-625.
91. A. E. Siegman, Ch. 16 "Wave Optics and Gaussian Beams," in *Lasers* (University Science Books, 1986), pp. 626-662.
92. A. E. Siegman, Ch. 17 "Physical Properties of Gaussian Beams," in *Lasers* (University Science Books, 1986), pp. 663-697.
93. H. Kogelnik, E. Ippen, A. Dienes, and C. Shank, "Astigmatically compensated cavities for CW dye lasers," *IEEE J. Quantum Elect.* **8**(3), 373-379 (1972).
94. J. Wilson and J. Hawkes, Ch. 3 "Modulation of Light," in *Optoelectronics: an introduction*, 3rd Edn. (Prentice Hall Europe, 1998), pp. 90-128.
95. R. W. Boyd, Ch. 2 "Wave-Equation Description of Nonlinear Optical Interactions," in *Nonlinear Optics*, 2nd Edn. (Academic Press, 2003), pp. 67-127.
96. W. Koechner, Ch. 11 "Damage of Optical Elements," in *Solid-State Laser Engineering*, 6th Edn. (Springer, 2006), pp. 680-701.
97. R. H. Kingston, "Parametric amplification and oscillation at optical frequencies," *Proc. IRE* **50**(4), 472 (1962).
98. J. A. Giordmaine and R. C. Miller, "Tunable Coherent Parametric Oscillation in LiNbO<sub>3</sub> at Optical Frequencies," *Phys. Rev. Lett.* **14**(24), 973-976 (1965).
99. R. J. Ellingson and C. L. Tang, "High-power, high-repetition-rate femtosecond pulses tunable in the visible," *Opt. Lett.* **18**(6), 438-440 (1993).
100. G. M. Gale, M. Cavallari, T. J. Driscoll, and F. Hache, "Sub-20-fs tunable pulses in the visible from an 82-MHz optical parametric oscillator," *Opt. Lett.* **20**(14), 1562-1564 (1995).
101. X. P. Zhang, J. Hebling, A. Bartels, D. Nau, J. Kuhl, W. W. Rühle, and H. Giessen, "1-GHz-repetition-rate femtosecond optical parametric oscillator," *Appl. Phys. Lett.* **80**(11), 1873-1875 (2002).



102. J. Jiang and T. Hasama, "Synchronously pumped femtosecond optical parametric oscillator based on an improved pumping concept," *Opt. Commun.* **220**(1-3), 193-202 (2003).
103. A. Esteban-Martin, O. Kokabee, and M. Ebrahim-Zadeh, "Efficient, high-repetition-rate, femtosecond optical parametric oscillator tunable in the red," *Opt. Lett.* **33**(22), 2650-2652 (2008).
104. O. Gayer, Z. Sacks, E. Galun, and A. Arie, "Temperature and wavelength dependent refractive index equations for MgO-doped congruent and stoichiometric LiNbO<sub>3</sub>," *Appl. Phys. B* **94**(2), 343-348 (2009).
105. O. Gayer, Z. Sacks, E. Galun, and A. Arie, "Erratum to: Temperature and wavelength dependent refractive index equations for MgO-doped congruent and stoichiometric LiNbO<sub>3</sub>," *Appl. Phys. B* **101**(1-2), 481-481 (2010).
106. J. Jiang and T. Hasama, "Harmonic repetition-rate femtosecond optical parametric oscillator," *Appl. Phys. B* **74**(4-5), 313-317 (2002).
107. M. C. Stowe, M. J. Thorpe, A. Pe'er, J. Ye, J. E. Stalnaker, V. Gerginov, and S. A. Diddams, Ch. "Direct Frequency Comb Spectroscopy," in *Advances in Atomic, Molecular and Optical Physics*, E. Arimondo, P. R. Berman, and C. C. Lin, eds. (Elsevier Inc., 2008), pp. 1-60.
108. L. Hollberg, C. W. Oates, E. A. Curtis, E. N. Ivanov, S. A. Diddams, T. Udem, H. G. Robinson, J. C. Bergquist, R. J. Rafac, W. M. Itano, R. E. Drullinger, and D. J. Wineland, "Optical frequency standards and measurements," *IEEE J. Quantum Elect.* **37**(12), 1502-1513 (2001).
109. R. Holzwarth, M. Zimmermann, T. Udem, and T. W. Hansch, "Optical clockworks and the measurement of laser frequencies with a mode-locked frequency comb," *IEEE J. Quantum Elect.* **37**(12), 1493-1501 (2001).
110. J. L. Hall, J. Ye, S. A. Diddams, M. Long-Sheng, S. T. Cundiff, and D. J. Jones, "Ultrasensitive spectroscopy, the ultrastable lasers, the ultrafast lasers, and the seriously nonlinear fiber: a new alliance for physics and metrology," *IEEE J. Quantum Elect.* **37**(12), 1482-1492 (2001).
111. G. Steinmeyer and U. Keller, Ch. 5 "Optical Comb Dynamics and Stabilization," in *Femtosecond Optical Frequency Comb Technology; Principle, Operation and Applications*, J. Ye and S. T. Cundiff, eds. (Springer, 2005), pp. 112-132.

112. R. Paschotta, A. Schlatter, S. C. Zeller, H. R. Telle, and U. Keller, "Optical phase noise and carrier-envelope offset noise of mode-locked lasers," *Appl. Phys. B* **82**(2), 265-273 (2006).
113. T. Udem, J. Reichert, T. W. Hänsch, and M. Kourogi, "Accuracy of optical frequency comb generators and optical frequency interval divider chains," *Opt. Lett.* **23**(17), 1387-1389 (1998).
114. T. Udem, J. Reichert, R. Holzwarth, and T. W. Hänsch, "Absolute Optical Frequency Measurement of the Cesium  $D_1$  Line with a Mode-Locked Laser," *Phys. Rev. Lett.* **82**(18), 3568-3571 (1999).
115. J. C. Knight, T. A. Birks, P. S. J. Russell, and D. M. Atkin, "All-silica single-mode optical fiber with photonic crystal cladding," *Opt. Lett.* **21**(19), 1547-1549 (1996).
116. J. C. Knight, T. A. Birks, P. S. J. Russell, and D. M. Atkin, "All-silica single-mode optical fiber with photonic crystal cladding: errata," *Opt. Lett.* **22**(7), 484-485 (1997).
117. T. A. Birks, J. C. Knight, and P. S. J. Russell, "Endlessly single-mode photonic crystal fiber," *Opt. Lett.* **22**(13), 961-963 (1997).
118. J. K. Ranka, R. S. Windeler, and A. J. Stentz, "Visible continuum generation in air-silica microstructure optical fibers with anomalous dispersion at 800 nm," *Opt. Lett.* **25**(1), 25-27 (2000).
119. A. L. Gaeta and R. S. Windeler, Ch. 4 "Microstructure Fiber and White-Light Generation," in *Femtosecond Optical Frequency Comb Technology; Principle, Operation and Applications*, J. Ye and S. T. Cundiff, eds. (Springer, 2005), pp. 97-111.
120. P. S. J. Russell, "Photonic-Crystal Fibers," *J. Lightw. Technol.* **24**(12), 4729-4749 (2006).
121. J. M. Dudley and J. R. Taylor, "Ten years of nonlinear optics in photonic crystal fibre," *Nat. Photonics* **3**(2), 85-90 (2009).
122. S. A. Diddams, D. J. Jones, J. Ye, S. T. Cundiff, J. L. Hall, J. K. Ranka, R. S. Windeler, R. Holzwarth, T. Udem, and T. W. Hänsch, "Direct Link between Microwave and Optical Frequencies with a 300 THz Femtosecond Laser Comb," *Phys. Rev. Lett.* **84**(22), 5102-5105 (2000).
123. D. J. Jones and S. T. Cundiff, "Optical Frequency Electronics," *IEEE Circuits Devices* **19**(5), 28-35 (2003).

124. M. Prevedelli, T. Freearge, and T. W. Hänsch, "Phase locking of grating-tuned diode lasers," *Appl. Phys. B* **60** 241-248 (1995).
125. A. Yariv and P. Yeh, Ch. 10 "Noise in Optical Detection and Generation," in *Photonics: Optical Electronics in Modern Communications*, 6th Edn. (Oxford University Press, 2007), pp. 465-500.
126. W. H. Press, S. A. Teukolsky, W. T. Vetterling, and B. P. Flannery, Ch. 12 "Fast Fourier Transform," in *Numerical Recipes: The Art of Scientific Computing*, 3rd Edn. (Cambridge University Press, 2007), pp. 600-639.
127. W. H. Press, S. A. Teukolsky, W. T. Vetterling, and B. P. Flannery, Ch. 13 "Fourier and Spectral Applications," in *Numerical Recipes: The Art of Scientific Computing*, 3rd Edn. (Cambridge University Press, 2007), pp. 640-719.
128. A. Yariv and P. Yeh, Ch. 11 "Detection of Optical Radiation," in *Photonics: Optical Electronics in Modern Communications*, 6th Edn. (Oxford University Press, 2007), pp. 501-538.
129. T. D. Mulder, R. P. Scott, and B. H. Kolner, "Amplitude and envelope phase noise of a modelocked laser predicted from its noise transfer function and the pump noise power spectrum," *Opt. Express* **16**(18), 14186-14191 (2008).
130. L. Matos, O. D. Mücke, J. Chen, and F. X. Kärtner, "Carrier-envelope phase dynamics and noise analysis in octave-spanning Ti : sapphire lasers," *Opt. Express* **14**(6), 2497-2511 (2006).
131. "iSource+™ Ultra LCR-900 Spec" (Spectratime, 2008), retrieved 26 March 2013, [www.spectratime.com/documents/lcr\\_spec.pdf](http://www.spectratime.com/documents/lcr_spec.pdf), Specification for Rb oscillators.
132. Jean-Luc Schwizgebel, Operational Manager, Spectratime, Vauseyon 29, 2000 Nechatel, Switzerland (personal communication, July 2011).
133. S. T. Dawkins, J. J. McFerran, and A. N. Luiten, "Considerations on the measurement of the stability of oscillators with frequency counters," *IEEE Trans. Ultrason. Ferroelectr. Freq. Control* **54**(5), 918-925 (2007).
134. A. S. Arnold, J. S. Wilson, and M. G. Boshier, "A simple extended-cavity diode laser," *Rev. Sci. Instrum.* **69**(3), 1236-1239 (1998).
135. "Handbook of Basic Atomic Spectroscopic Data: Rubidium" (The National Institute of Standards and Technology, 2005), retrieved 14 Jan. 2013, <http://physics.nist.gov/PhysRefData/Handbook/Tables/rubidiumtable1.htm>, NIST Standard Reference Database 108 (J. E. Sansonetti and W. C. Martin).

136. P. Siddons, C. S. Adams, G. C., and I. G. Hughes, "Absolute absorption on rubidium D lines: comparison between theory and experiment," *J. Phys. B: At. Mol. Opt. Phys.* **41**(15), 155004 (2008).
137. J. M. Hollas, Ch. 2 "Electromagnetic radiation and its interaction with atoms and molecules," in *Modern Spectroscopy*, 3rd Edn. (John Wiley & Sons, 1997), pp. 25-.
138. J. Wilson and J. Hawkes, Ch. 5 "Lasers I," in *Optoelectronics:an introduction*, 3rd Edn. (Prentice Hall Europe, 1998), pp. 169-243.
139. K. B. Macadam, A. Steinbach, and C. Wieman, "A narrow-band tunable diode-laser system with grating feedback, and a saturated absorption spectrometer for Cs and Rb," *Am. J. Phys.* **60**(12), 1098-1111 (1992).
140. J. Hecht, Ch. 4 "Enhancements to Laser Operation," in *The Laser Guidebook*, 2nd Edn. (McGraw-Hill, Inc, 1999), pp. 43-57.
141. T. W. Hänsch, "Repetitively Pulsed Tunable Dye Laser for High Resolution Spectroscopy," *Appl. Opt.* **11**(4), 895-898 (1972).
142. M. W. Fleming and A. Mooradian, "Spectral Characteristics of External-Cavity Controlled Semiconductor Lasers," *IEEE J. Quantum Elect.* **17**(1), 44-59 (1981).
143. C. J. Hawthorn, K. P. Weber, and R. E. Scholten, "Littrow configuration tunable external cavity diode laser with fixed direction output beam," *Rev. Sci. Instrum.* **72**(12), 4477-4479 (2001).
144. M. G. Littman and H. J. Metcalf, "Spectrally narrow pulsed dye laser without beam expander," *Appl. Opt.* **17**(14), 2224-2227 (1978).
145. M. S. Kirchner, D. A. Braje, T. M. Fortier, A. M. Weiner, L. Hollberg, and S. A. Diddams, "Generation of 20 GHz sub-40 fs pulses at 960 nm via repetition-rate multiplication," *Opt. Lett.* **34**(7), 872-874 (2009).
146. J. Ye, S. Swartz, P. Jungner, and J. L. Hall, "Hyperfine structure and absolute frequency of the  $^{87}\text{Rb}$   $5P_{3/2}$  state," *Opt. Lett.* **21**(16), 1280-1282 (1996).
147. L. Ricci, M. Weidemüller, T. Esslinger, A. Hemmerich, C. Zimmermann, V. Vuletic, W. König, and T. W. Hänsch, "A compact grating-stabilized diode laser system for atomic physics," *Opt. Commun.* **117**(5-6), 541-549 (1995).
148. Thorlabs Inc., "LT230P-B Support Documentation: Auto CAD PDF", retrieved 23 Oct. 2012, <http://www.thorlabs.de/Thorcat/0800/LT230P-B-AutoCADPDF.pdf>, LT230P-B - Collimation Tube with Optic for Ø235.236 & Ø239 mm Laser Diodes.

149. E. Benkler, F. Rohde, and H. R. Telle, "Robust interferometric frequency lock between cw lasers and optical frequency combs," *Opt. Lett.* **38**(4), 555-557 (2013).
150. J. Reichert, R. Holzwarth, T. Udem, and T. W. Hänsch, "Measuring the frequency of light with mode-locked lasers," *Opt. Commun.* **172**(1-6), 59-68 (1999).
151. C. E. Cramer, C. H. Li, A. J. Benedick, G. A.G., K. F.X., D. F. Phillips, D. Sassellov, A. Szentgyorgyi, and R. L. Walsworth, "Astro-comb: revolutionizing precision spectroscopy in astrophysics," in *IAU Symposium, No. 253, 2008*, (International Astronomical Union, 2009).
152. J. Chen, J. W. Sickler, P. Fendel, E. P. Ippen, F. X. Kartner, T. Wilken, R. Holzwarth, and T. W. Hansch, "Generation of low-timing-jitter femtosecond pulse trains with 2 GHz repetition rate via external repetition rate multiplication," *Opt. Lett.* **33**(9), 959-961 (2008).
153. G. Chang, C.-H. Li, D. F. Phillips, A. Szentgyorgyi, R. L. Walsworth, and F. X. Kärtner, "Optimization of filtering schemes for broadband astro-combs," *Opt. Express* **20**(22), 24987-25013 (2012).
154. C. Gohle, B. Stein, A. Schliesser, T. Udem, and T. W. Hänsch, "Frequency Comb Vernier Spectroscopy for Broadband, High-Resolution, High-Sensitivity Absorption and Dispersion Spectra," *Phys. Rev. Lett.* **99**(26), 2639021-2639024 (2007).
155. F. Herzog, K. Kudiella, D. Erni, and W. Bachtold, "Optical Phase Locking by Local Oscillator Phase Dithering," *IEEE J. Quantum Elect.* **42**(10), 973-985 (2006).
156. E. D. Black, "An introduction to Pound--Drever--Hall laser frequency stabilization," *Am. J. Phys.* **69**(1), 79-87 (2001).
157. D. A. Shaddock, M. B. Gray, and D. E. McClelland, "Frequency locking a laser to an optical cavity by use of spatial mode interference," *Opt. Lett.* **24**(21), 1499-1501 (1999).
158. B. J. J. Slagmolen, D. A. Shaddock, M. B. Gray, and D. E. McClelland, "Frequency Stability of Spatial Mode Interference (Tilt) Locking," *IEEE J. Quantum Elect.* **38**(11), 1521-1528 (2002).
159. A. E. Siegman, Ch. 19 "Stable Two-Mirror Resonators," in *Lasers* (University Science Books, 1986), pp. 744-776.

160. M. Born and E. Wolf, Ch. 7 "Elements of the theory of interference and interferometers," in *Principles of optics*, 7th Edn. (Cambridge University Press, 2005), pp. 286-411.